ABSTRACT

Title of dissertation: ELECTROMAGNONS IN MULTIFERROIC
MATERIALS

Rolando Valdés Aguilar, Doctor of Philosophy, 2008

Dissertation directed by: Professor H. Dennis Drew
Department of Physics

This dissertation focuses on the study of spin-lattice and magnon-phonon coupling in multiferroic materials based on their electrodynamic response. Based on a study of the electrodynamic response in the far infrared region of the electromagnetic spectrum of 2 families of multiferroic compounds, a new elementary excitation has been discovered, called electromagnon. This is the central topic of this thesis. The electromagnon is a hybrid excitation composed of phonon and magnon parts that is observable in these materials due to to its electric dipole coupling to the electromagnetic field. This coupling comes about due to the strong magnetoelectric interactions in these materials that are responsible for their multiferroic behavior. Models that describe the experimental features of these excitations are outlined for each of these families of multiferroics.

ELECTROMAGNONS IN MULTIFERROIC
MATERIALS

by

Rolando Valdés Aguilar

Dissertation submitted to the Faculty of the Graduate School of the
University of Maryland, College Park in partial fulfillment
of the requirements for the degree of
Doctor of Philosophy
2008

Advisory Committee:
Professor H. Dennis Drew, Chair/Advisor
Professor Victor Galitski
Professor Richard L. Greene
Professor Johnpierre Paglione
Professor Ichiro Takeuchi

A mis papás,

y

a Beatriz.

Acknowledgments

This has been made possible by the genius and work of my advisor Professor Dennis Drew. He conceived the original idea and obtained the resources for this project to be carried out. He also provided me with encouragement, guidance and an infinite amount of patience that were crucial in my development as a scientist. Dennis has provided the kindest of attention since the very first encounter we had when I was just a beginning graduate student trying to find a research opportunity during the summer after my first year here in Maryland. Even though I started working without much experience in a laboratory setting, Dennis and the *Drew Group* were always there to provide some direction when I felt lost. This is my opportunity to express my gratitude to him and the people in the group, as well as all the people that have, in large and small amounts, contributed to my development as a scientist and, hopefully, made me a better person.

I would like to thank the members of my dissertation committee: Prof. Richard Greene, Prof. Ichiro Takeuchi, Prof. Johnpierre Paglione and Prof. Victor Galitskii for accepting to read and comment on this thesis.

All the members of the *Drew Group*, past and present, were good friends and excellent teachers in the workings of the lab. I have to thank first the support of Dr. Andrei Sushkov. Andrei, with all the experience that I lacked, guided this research program in new and very interesting directions and was the closest of collaborators, he obtained a significant portion of the data presented in this dissertation. In addition I thank Geoff Evans, Dr. Don Schmadel, Dr. Paul Kolb, Dr. Gregory Jenkins and Professor Jeffrey

Simpson.

I also want to thank Professor Maxim Mostovoy from Groeningen University in The Netherlands. He was interested from the very beginning in our investigation of the electrodynamics of multiferroics. He developed the theories that are used in this dissertation to explain our findings and has become a close collaborator.

I thank and appreciate greatly the Mexican community that we have formed during the last years here at UMD. I specially thank Fernando Galaz García and Adrian Pérez Galván for being good friends. This little group provided for a home away from home to me and I will always be fond of the memories that we have created together.

The physics class of the Fall 2003 became a fertile ground for interactions. I will always remember my TA office, *The Farm*, and my office mates that became my defacto first collaborators. Ron Toland, Michael Barnes, Dr. Ingmar Broemstrup, Dr. Matt Cornick, Nick Mecholsky, Cory Poole, Young-Noh Yoon, Rennee Michelle Goertzen, Matty Lau, Dr. Tom Bing, Shaela Jones-Mecholsky, Tracy Moore, Joe Tuggle, Jared

Hertzberg, Matt Beeler and Michael Scholten are some of the people with whom I shared those first moments.

I would specially like to thank all of the staff in the Department of Physics and the MRSEC office. I thank Linda O'hara, Jane Hessing and Julie Callis, without whom my life would have been much more difficult dealing with the bureaucracy of the University.

My family has always supported me. Ever since I decided in high school that I wanted to become a physicist they have stood by me, supported me, encouraged me and yes, sometimes considered me crazy for continuing in school in the pursuit of a doctorate degree. My sisters Rebeca, Raquel and Roselina, and my brother Roberto have been fundamental in my development as a man and I will always love them. Mamá, papá les debo todo a ustedes gracias por apoyarme todo este tiempo.

At last, but not least, I thank my wife Beatriz. She has been there for me through it all even as she herself walks the path of graduate school. I just hope I can be as supporting of her as she has been of me. Gracias Betty.

Table of Contents

List of Tables

List of Figures

Chapter 1

Introduction

1.1   Motivation

Multiferroic compounds are materials where ferroelectric and magnetic orders co-exist in a single phase. In some cases strong coupling between the different orders exists and has led to the observation of spectacular effects such as the rotation of the polarization vector $\mathbf{P}$ with the application of magnetic field $\mathbf{H}$ [1]. Multiferroicity is related to the magnetoelectric effect [2]. The magnetoelectric effect is the induction of magnetization (polarization) when an external electric (magnetic) field is applied. Multiferroicity, on the other hand, refers to the coexistence and coupling between different types of order in a crystal: magnetic, dielectric and elastic. The orders where there is a finite spontaneous moment characterizing its symmetry are called *ferroics* [3] although multiferroics usually also include the anti-ferroic orders. That is because this allows complex magnetic, ferroelectric and elastic orders to coexist and interact. Nevertheless, the term *multiferroic* has been focused mostly in materials where ferroelectricity and magnetism coexist and interact, and this is the meaning it is given in this thesis.

In this regard, the definition used here is more general than the original one given by H. Schmid [3]. This is mainly because materials that have *anti-ferroic* order are
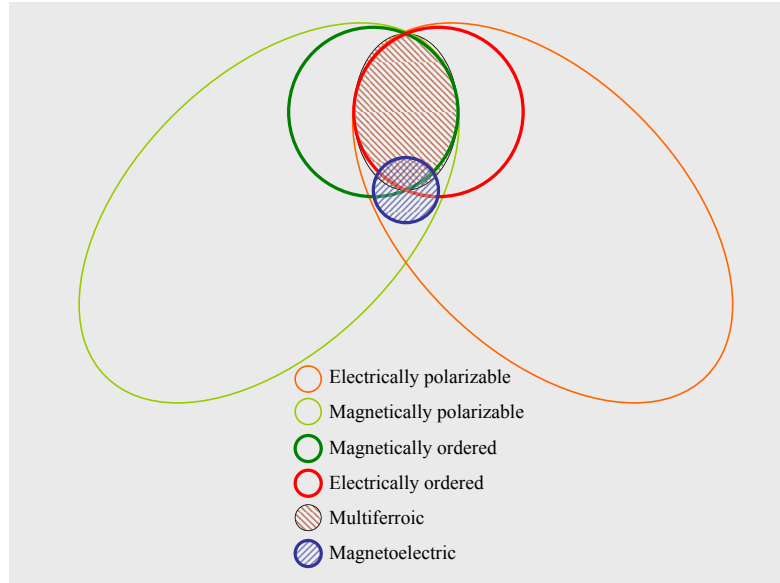
Figure 1.1: Phase diagram of magnetic and dielectric materials. Multiferroics exist only in the phase of joint magnetically and electrically ordered systems.

more common than purely ferroic multiferroics, and as such the more flexible definition allows for the study of a larger class of materials. The relation between magnetic and electric properties is schematically shown in figure 1.1, where the intersection between magnetic and ferroelectric materials defines the multiferroic phase, and also the materials where the magnetoelectric effect can be observed. As can be seen, magnetoelectric and multiferroic materials coexist in a small region of this phase space, but they are mostly independent. It is common to find in the literature that the terms are used indistinctly even though as shown figure 1.1 these phases are actually different.

A telling sign of the interest in these subjects is the rapid increase in publications with the keywords multiferroic and magnetoelectric in the online database ISI Web of
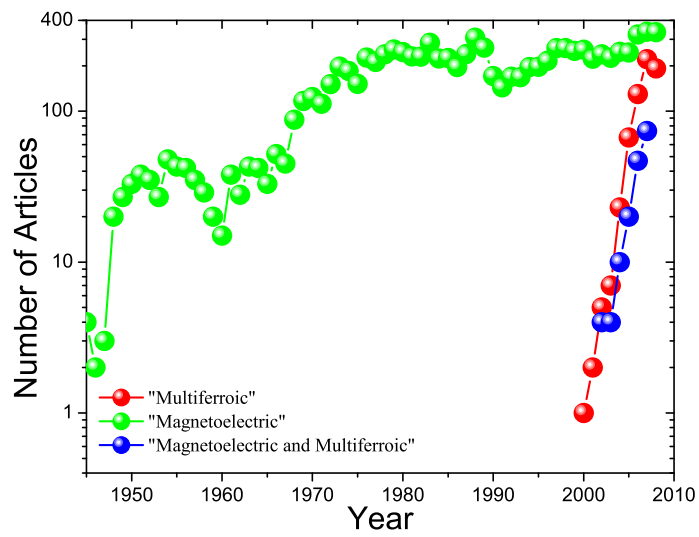
Figure 1.2: Number of articles indexed in the ISI Web of Knowledge database under the keywords 'Multiferroic' and 'Magnetoelectric.'

Science [4] as of September 11th 2008. As shown in figure 1.2, the term multiferroic began being used in the year 2000, and the number of publications whose topic is multiferroic behavior of materials shows a rapid, exponential increase. On the other hand the field of magnetoelectrics is older and with a more steady output of publications through the years, with only a slight increase in the last few years. As a sign of the confounding of these fields the figure also shows the number of publications where both terms are keywords, the time dependence of this is similar to the "multiferroic" curve. It should be cautioned that this, as any other database, is not complete and fully updated, and thus many articles that are better classified in one of these categories, may not have been included in the above numbers.

1.2 The Physics of Multiferroics

The first question to be answered is how the distinct order parameters are coupled and how this coupling can be accessed in experiments. In one of the first modern proposals for a mechanism of multiferroic coupling, Katsura, *et al.* [5] showed that by considering the spin orbit coupling in the superexchange interaction between non-collinear nearest neighbor spins, ferroelectric polarization could be induced with the following form

$$\mathbf{P} \propto \hat{e_{ij}} \times (\vec{S_i} \times \vec{S_j}) \tag{1.1}$$

where $\hat{e_{ij}}$ is the unit vector in the direction between the lattice sites of spins S_i and S_j. It is clear also that non-collinearity between spins is necessary to obtain a non-zero $\mathbf{P}$.

4

This form of coupling between spins and **P** resembles the form of the antisymmetric superexchange interaction $E = \mathbf{D} \cdot (S_1 \times S_2)$, the Dzyaloshinskii-Moriya (DM) interaction [6, 7]. The DM interaction is also derived from the spin orbit coupling effects on the exchange. It has the effect of canting spins out of their collinear configurations favored by the symmetric Heisenberg exchange. The Katsura, *et al.* picture is sometimes called the inverse Dzyaloshinskii-Moriya (IDM) effect because now the non-collinear spins act back on the lattice to create the lattice distortion that induces ferroelectricity [8].

From a phenomenological point of view it was shown [9] that just by considering the fundamental symmetries that are broken in the multiferroic state, time reversal and space inversion, it is possible to obtain ferroelectricity from a non-homogeneous magnetic state. The general form of the ferroelectric polarization **P** in this case is

$$\mathbf{P} \propto (\mathbf{M} \cdot \nabla)\mathbf{M} - \mathbf{M}(\nabla \cdot \mathbf{M}) \tag{1.2}$$

where **M** is the local magnetization at a lattice site. It is clear from equation 1.2 that only a non-homogeneous magnetic state is capable of producing a non-zero **P**. In particular, in a spiral cycloidal state (see figure 1.3) such as $\mathbf{M} = M_1\cos(\mathbf{Q} \cdot \mathbf{x} + \phi_1)\hat{x} + M_2\cos(\mathbf{Q} \cdot \mathbf{y} + \phi_2)\hat{y}$, the polarization is

$$\mathbf{P} \propto \sin(\phi_1 - \phi_2)[\mathbf{Q} \times (M_1\hat{x} \times M_2\hat{y})] \tag{1.3}$$

here **Q** is the propagation vector of the spiral. From the form of equation 1.3 we see a striking similarity to equation 1.1, in both cases **P** is proportional to the cross product between spins in different lattice sites. This can be interpreted in the sense that the model

5
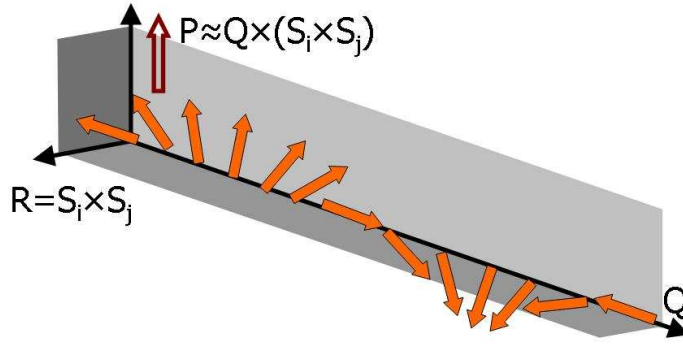
Figure 1.3: Cycloidal Spiral Magnetic order and polarization direction.

of Katsura *et al.* [5] provides for a microscopic mechanism of the phenomenological symmetry analysis of Mostovoy [9]. Therefore, the origin of the coupling between the magnetic and ferroelectric orders in these theories is the spin orbit interaction. These models have been extended and generalized for different cases of the spin orbit interaction [10, 11]. The basic principle of non-collinear magnetic structures and, in particular, of cycloidal spins has been used to discover new multiferroic compounds [12].

One might question whether the approaches outlined above are the more general way of understanding the coupling between magnetism and ferroelectricity. In particular, is spin orbit coupling necessary to achieve magnetically induced ferroelectricity? The answer is obviously no. In order to see this, consider the case of 2 magnetic ions and the symmetric Heisenberg exchange interaction between them $E = JS_1 \cdot S_2$. If we assume that the exchange constant depends on the polarization (or, equivalently, on the

6

distance between ions) $\mathbf{P}$ then we can make an expansion of J in powers of $\mathbf{P}$

$$J(\mathbf{P}) = J(0) + \frac{\partial J}{\partial \mathbf{P}}(0) \cdot \mathbf{P} + \mathbf{P}_i \frac{\partial^2 J}{\partial \mathbf{P}_i \partial \mathbf{P}_j}(0) \mathbf{P}_j + \ldots \tag{1.4}$$

in this case the polarization points in the direction between the lattice sites, and has the following form [13]

$$\mathbf{P} \propto \hat{e_{12}} J'(0) \vec{S_1} \cdot \vec{S_2} \tag{1.5}$$

This type of coupling has been used to explain the origin of ferroelectricity in $R\mathrm{Mn_2O_5}$ [13], orthorhombic $\mathrm{HoMnO_3}$ [14] and $\mathrm{Ca_3CoMnO_6}$ [15]. Since this type of coupling does not depend on the spin orbit interaction, it is expected that the polarization value for these multiferroics be larger than in the spin orbit induced ones.

These two microscopic mechanisms of magnetically-induced ferroelectricity give rise to two different forms of phenomenological magnetoelectric coupling: electric polarization induced by a spiral cycloid equation 1.3 is described by the third-order coupling term $P(L_1 \partial L_2 - L_2 \partial L_1)$, where P is electric polarization and $L_{1,2}$ are magnetic order parameters describing the sinusoidal and cosinusoidal components of the spiral [9, 16], while the coupling working in collinear spin states has the form $P(L_1^2 - L_2^2)$, where L_1 and L_2 are components of a two-dimensional irreducible representation describing magnetic states with opposite electric polarizations [14, 17, 18, 19].

1.3 Magnetic Orders and Ferroelectricity

Fundamental interest in multiferroicity also derives from the strong interplay between magnetic frustration, ferroelectric order, and fundamental symmetry issues in phase transformations that characterize these materials [1, 9, 12, 19, 20, 21, 22]. It is important to note that equations 1.3 and 1.5 are derived from a local 'molecular' picture, it is still unclear whether a macroscopic polarization can be induced after adding up these contributions within the unit cell of specific materials. It is therefore crucial to consider the characteristics of materials that would allow a finite polarization. In the next subsections the two families of multiferroics which are the focus of this dissertation will be introduced in the context of these two different origins of ferroelectricity in magnetic materials.

1.3.1 Multiferroics RMnO$_3$

The compound TbMnO$_3$ was discovered to be ferroelectric below $T \sim 28$K in 2003 [1] as has spurred a flurry of activity in the field of multiferroics (see figure 1.2). It was later shown that the ferroelectric transition occurred at the same time as the transition from a spin density wave state to a cycloidal spiral state [23], this finding allows the identification of the mechanism in equation 1.1 as a possible origin of polarization in this material.

1.3.1.1 Symmetry analysis of $R\mathrm{MnO_3}$

In this subsection a symmetry based analysis of the magnetic structure and the magnetoelectric interaction is presented, this method clarifies the relation between this family and other multiferroic materials. The positions of the $\mathrm{Mn^{3+}}$ in the paramagnetic unit cell in the space group *Pbnm* are shown in table 1.1 (in this case only the Mn ion is assumed to be magnetic, the rare earth ion magnetism is ignored because its role on the multiferroic behavior is minimal).

Table 1.1: Coordinates of Mn ions and magnetic order parameters in $R\mathrm{MnO_3}$

$\mathrm{Mn^{3+}}$	Order Parameters for $\mathbf{k} = 0$
$(1) = \left(0, \frac{1}{2}, 0\right)$	$F = S_1 + S_2 + S_3 + S_4$
$(2) = \left(\frac{1}{2}, 0, 0\right)$	$C = S_1 + S_2 - S_3 - S_4$
$(3) = \left(0, \frac{1}{2}, \frac{1}{2}\right)$	$G = S_1 - S_2 + S_3 - S_4$
$(4) = \left(\frac{1}{2}, 0, \frac{1}{2}\right)$	$A = S_1 - S_2 - S_3 + S_4$

The magnetic order parameters in table 1.1 are the linear combinations of spins that transform according to all the symmetries of the crystallographic space group *Pbnm*, that is, these magnetic structure correspond to the wave vector $\mathbf{k} = 0$. Because the experimentally obtained magnetic structure has a wave vector $\mathbf{k} = (0, 0.28, 0)$, these order parameters do not fully reflect the symmetry of the ground state because this incommensurate wave vector breaks the translational symmetry of the lattice. In what follows the method of representational analysis [19, 24, 25] is used to describe the order parameters of the magnetic structure in $R\mathrm{MnO_3}$.

In order to find the correct order parameters, the crystal must be invariant under the symmetry operations that leave the wave vector unchanged, the irreducible representations that correspond to the group of operations that leave $\mathbf{k}$ invariant are shown in table 1.2.

Table 1.2: Irreducible representation of the group of $\mathbf{k} = (0,q,0)$ in *Pbnm*. Here $\Lambda = e^{\imath \pi q}$.

	1	2_y	m_{xy}	m_{yz}
Γ_1	1	Λ	1	Λ
Γ_2	1	Λ	-1	$-\Lambda$
Γ_3	1	$-\Lambda$	1	$-\Lambda$
Γ_4	1	$-\Lambda$	-1	Λ

Now the basis functions can be constructed with respect to the $k = 0$ order parameters if we write the magnetic structure in the following way

$$S_\alpha(\mathbf{k}, \tau) = \frac{1}{N} \sum_{\mathbf{R},\Gamma} S_\alpha^\Gamma(\mathbf{R} + \tau) e^{\imath \mathbf{k} \cdot (\mathbf{R} + \tau)} \tag{1.6}$$

where N is the number of unit cells in the system, S_α^Γ is the thermally averaged spin value in the α direction within the irreducible representation Γ, τ is the position of the τth spin in the unit cell, and $\mathbf{R}$ is a lattice vector.

The amplitudes of the basis functions in table 1.3 can be further constrained by symmetry but this is not attempted here. Instead the second order invariant with respect to spin variables is built out of the basis functions, this is to be used within a Landau theory [26] to explore the basic magnetoelectric mechanism.

10

Table 1.3: Basis functions of the space group of $\mathbf{k} = (0, q, 0)$ in *Pbnm*

	Γ_1	Γ_2	Γ_3	Γ_4
S_x^Γ	C_x	$-G_x$	$-A_x$	F_x
S_y^Γ	$-A_y$	F_y	C_y	$-G_y$
S_z^Γ	$-G_z$	C_z	F_z	$-A_z$

Kenzelmann, *et al.* [23] found that TbMnO$_3$ first becomes magnetically order in an incommensurate spin density wave (SDW) state with $\mathbf{k} = (0, 0.28, 0)$ that belongs to the Γ_3 irreducible representation. At 28K, there is a transition to the spiral cycloidal state composed out of the Γ_3 and Γ_2 irreducible representations in table 1.3. The coefficients were $S_x^{\Gamma_2} = S_x^{\Gamma_3} = S_y^{\Gamma_2} = S_z^{\Gamma_3} = 0$, $S_z^{\Gamma_2} = 3\mu_B$, and $S_y^{\Gamma_3} = 4.7\mu_B$. This structure corresponds to a cycloidal spiral in the $y - z$ plane that propagates along the y axis as shown in figure 1.4.

Because two different irreducible representations exist in the ground state, an invariant containing both symmetries will transform as the product of both $\Gamma_2 \otimes \Gamma_3$. From table 1.2 it can be checked that this product is odd under 2_y and m_{xy}. This symmetry property correspond to the transformation of a polar vector P_z. Therefore, the invariant in the free energy expansion that contains these terms, identifying the polar vector with the actual polarization, is $a_z \sigma_2(q)\sigma_3(-q)P_z + \text{c.c.}$, where c.c. is the complex conjugate, σ_Γ is the amplitude of the basis function (table 1.3) for the respective irreducible representation Γ, and a_z is the coupling constant. After taking the complex conjugate and
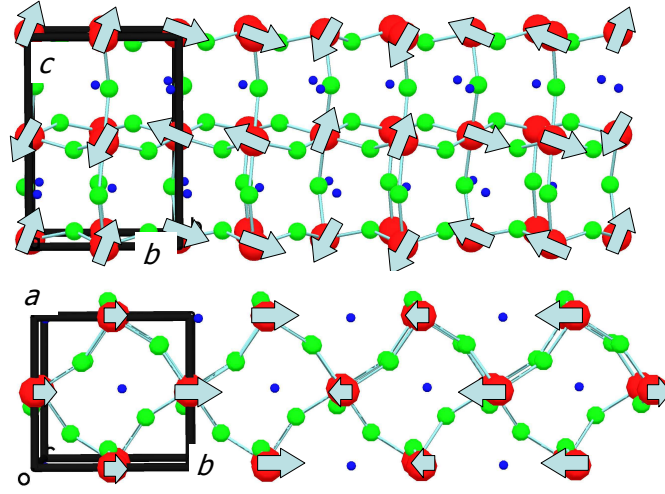
Figure 1.4: Spiral structure in TbMnO$_3$.

taking all the phase factors from equation 1.6 the invariant has the form:

$$\Phi_{ME} = a_z P_z |\sigma_2(q)||\sigma_3(-q)| \sin(\phi_2 - \phi_3) \tag{1.7}$$

where ϕ_Γ is the total phase of the irreducible representation Γ, which includes an overall phase for each one. We can add this term in equation 1.7 in a Landau expansion of the free energy to study the ferroelectric phase transition $\Phi = \frac{P_z^2}{2\chi_E} + \Phi_{ME}$. After minimization of Φ and solving for P_z it is obtained:

$$P_z = -\chi_E a_z |\sigma_3||\sigma_2| \sin(\phi_2 - \phi_3) \tag{1.8}$$

which gives identical results to equation 1.3. Also note that in the high temperature SDW state a quadratic invariant such as equation 1.7 cannot exist because the square of

12

the Γ_3 representation does not transform as a polar vector. Finally, it should be noted that the term equation 1.7 is sometimes referred to as a third order invariant because it contains two magnetic order parameters and one polar vector.

1.3.2 Multiferroics $R\mathrm{Mn_2O_5}$

This family of multiferroics is slightly more complicated in its magnetic structure and phase transitions. The interest in this family surged after Hur, *et al.*[20] reported that a magnetic field could change the polarization direction by $180°$, i.e. the polarization vector can be flipped by magnetic field. These materials order antiferromagnetically above 40 K with an incommensurate SDW structure and $\mathbf{k} = (q_1, 0, q_2)$. Around 38 K there is a transition to a commensurate and ferroelectric state with $\mathbf{k} = (1/2, 0, 1/4)$ and $\mathbf{P} = (0, P_b, 0)$. Finally around 25 K there is an additional transition to an incommensurate state which is weakly ferroelectric. This transitions have been extensively studied from a Landau theory perspective by A.B. Harris and his coauthors [19, 27, 28], therefore in what follows only an outline of the symmetry analysis is given for the commensurate and ferroelectric state.

1.3.2.1 Symmetry analysis of $R\mathrm{Mn_2O_5}$

In this subsection a phenomenological description of spin states and the magneto-electric coupling mechanism that derives from the Heisenberg exchange is discussed, which will clarify the similarities between $R\mathrm{Mn_2O_5}$ and other multiferroic materials.

13

The positions of Mn^{3+} and Mn^{4+} in the paramagnetic unit cell are shown in table 1.4 and the eight vector order parameters can be found in table 1.5 (the notations of Bertaut *et al.*[29] are used).

Table 1.4: The coordinates of Mn ions, where $x \approx 0.41$, $y \approx 0.35$ and $z \approx 0.26$ (for $BiMn_2O_5$).

Mn^{3+}	Mn^{4+}
$r_1 = (x, y, 1/2)$	$r_5 = (1/2, 0, z)$
$r_2 = (-x, -y, 1/2)$	$r_6 = (1/2, 0, -z)$
$r_3 = (1/2 - x, 1/2 + y, 1/2)$	$r_7 = (0, 1/2, z)$
$r_4 = (1/2 + x, 1/2 - y, 1/2)$	$r_8 = (0, 1/2, -z)$

Table 1.5: Magnetic order parameters.

Mn^{3+}	Mn^{4+}
$F = S_1 + S_2 + S_3 + S_4$	$F' = S_5 + S_6 + S_7 + S_8$
$C = S_1 + S_2 - S_3 - S_4$	$C' = S_5 + S_6 - S_7 - S_8$
$G = S_1 - S_2 + S_3 - S_4$	$G' = S_5 - S_6 + S_7 - S_8$
$A = S_1 - S_2 - S_3 + S_4$	$A' = S_5 - S_6 - S_7 + S_8$

For discussion of phenomenological description of the magnetoelectric coupling, the relatively simple case of $BiMn_2O_5$ is best suited, which shows the commensurate spin ordering with $Q = (1/2, 0, 1/2)$. In this case the components of the order param-

Table 1.6: Irreducible representations of the space group *Pbam* for $Q = (1/2, 0, 1/2)$.

	2_x	2_y	2_z	m_x	m_y	m_z	I
Γ_1	$\begin{pmatrix} 0 & 1 \\ -1 & 0 \end{pmatrix}$	$\begin{pmatrix} 1 & 0 \\ 0 & -1 \end{pmatrix}$	$\begin{pmatrix} 0 & -1 \\ -1 & 0 \end{pmatrix}$	$\begin{pmatrix} 1 & 0 \\ 0 & -1 \end{pmatrix}$	$\begin{pmatrix} 0 & 1 \\ -1 & 0 \end{pmatrix}$	$\begin{pmatrix} 1 & 0 \\ 0 & 1 \end{pmatrix}$	$\begin{pmatrix} 0 & -1 \\ -1 & 0 \end{pmatrix}$
Γ_2	$\begin{pmatrix} 0 & -1 \\ 1 & 0 \end{pmatrix}$	$\begin{pmatrix} 1 & 0 \\ 0 & -1 \end{pmatrix}$	$\begin{pmatrix} 0 & 1 \\ 1 & 0 \end{pmatrix}$	$\begin{pmatrix} -1 & 0 \\ 0 & 1 \end{pmatrix}$	$\begin{pmatrix} 0 & 1 \\ -1 & 0 \end{pmatrix}$	$\begin{pmatrix} -1 & 0 \\ 0 & -1 \end{pmatrix}$	$\begin{pmatrix} 0 & -1 \\ -1 & 0 \end{pmatrix}$

eters belong to one of the two two-dimensional representations, Γ_1 or Γ_2, of the *Pbam* group [29, 30]. BiMn$_2$O$_5$ only shows the 'collinear' state with the *a*-components of the Mn^{3+} and Mn^{4+} spins described, respectively, by the order parameters $F_x = -3.1\mu_B$ and $G'_x = 2.4\mu_B$ with small *b* components $C_y = -0.8\mu_B$ and $A'_y = 0.6\mu_B$ [30] corresponding to a small rotation between spins in neighboring antiferromagnetic chains. A cartoon of this structure is shown in figure 1.5 together with one of the Γ_1 representations that induce ferroelectricity.

Table 1.7: Basis vectors of the space group *Pbam* for $Q = (1/2, 0, 1/2)$.

Γ_1	$\begin{pmatrix} F_x \\ C_x \end{pmatrix}$	$\begin{pmatrix} C_y \\ F_y \end{pmatrix}$	$\begin{pmatrix} G_x \\ -A_x \end{pmatrix}$	$\begin{pmatrix} -A_y \\ G_y \end{pmatrix}$			$\begin{pmatrix} C'_z \\ F'_z \end{pmatrix}$	$\begin{pmatrix} G'_x \\ -A'_x \end{pmatrix}$	$\begin{pmatrix} -A'_y \\ G'_y \end{pmatrix}$
Γ_2		$\begin{pmatrix} F_z \\ C_z \end{pmatrix}$	$\begin{pmatrix} G_z \\ -A_z \end{pmatrix}$	$\begin{pmatrix} C'_x \\ F'_x \end{pmatrix}$	$\begin{pmatrix} F'_y \\ C'_y \end{pmatrix}$				$\begin{pmatrix} G'_z \\ -A'_z \end{pmatrix}$
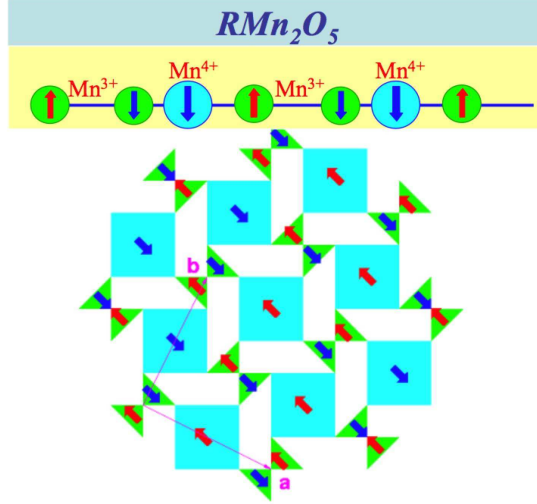
Figure 1.5: Spin structure in the commensurate phase of $R\text{Mn}_2\text{O}_5$.

Since F_x is the part two-dimensional representation $\begin{pmatrix} F_x \\ C_x \end{pmatrix} \in \Gamma_1$, the state described by the order parameter C_x is another ground state of the system. These two states are related by inversion, which transforms F_x into $-C_x$ and vice versa. It is easy to check that the magnetoelectric coupling of the form $-\lambda_x P_y \left(F_x^2 - C_x^2 \right)$ is invariant upon all symmetry transformations of the paramagnetic phase, so that the order parameters F_x and C_x describe two ferroelectric states with opposite directions of electric polarization. It also easy to check that the couplings $-\lambda_y P_y \left(F_y^2 - C_y^2 \right)$ and $-\lambda_z P_z \left(F_z^2 - C_z^2 \right)$ are also allowed by symmetry, which is a strong indication that the mechanism inducing electric polarization in the magnetically ordered state is invariant upon the global spin rotation and the coupling can be written in the form $\lambda P_y \left(F^2 - C^2 \right)$ [18].

Due to the exchange coupling between the Mn^{3+} and Mn^{4+} ions, the order param-

eters G'_x and F_x are strongly coupled. Since $\begin{pmatrix} G'_x \\ -A'_x \end{pmatrix}$ also belongs to Γ_1 representation, the coupling between the two spin subsystems is phenomenologically described by $-g\left(F_x G'_x - C_x A'_x\right)$ [18]. Thus, more generally, the magnetoelectric coupling should be written in the form

$$\Phi_{\mathrm{me}} = -\lambda P_y \left(\eta_1^2 - \eta_2^2\right) \tag{1.9}$$

where $\begin{pmatrix} \eta_1 \\ \eta_2 \end{pmatrix}$ belongs to Γ_1 representation. Because this coupling term was built from order parameters of a single irreducible representation, the coupling 1.9 derives from the Heisenberg exchange interaction as proposed in 1.5. This form of the third-order magnetoelectric coupling was discussed previously by A.B. Harris [19] and in the context of the orthorhombic manganites with the E-type magnetic ordering [14] and is typical for improper ferroelectrics [17].

1.4 Dynamic Magnetoelectric Coupling

Symmetry considerations are essential for unraveling the relevant interactions in these complex systems [22, 19]. While the direction of the spontaneous electric polarization $\mathbf{P}$ is controlled by symmetry it does not uniquely identify the coupling mechanism [22, 19]. On the other hand, the direction, or selection rules, for the dynamics may be different for different exchange mechanisms, and therefore may help identify the dominant exchange processes involved in multiferroicity.

17

The role of the 3rd-order DM as well as 4th-order isotropic exchange ($\Phi_{ME} \sim P^2 S_1^2 S_2^2$) coupling terms in dynamic coupling has been discussed [31, 32]. It is understood that different coupling terms couple phonons to different magnon branches [31]. However, the DM exchange, due to its relativistic origin, is intrinsically weak so that symmetric exchange may be expected to be more favorable for strong coupling.

The known microscopic mechanisms of magnetically-induced ferroelectricity include lattice distortion and redistribution of electron density in response to spin ordering. Such processes occur locally in all magnetic materials. However, only when a spin ordering breaks inversion symmetry do these local electric dipoles add into a macroscopic electric polarization. Therefore the study of the dynamical response, which provides additional symmetry information through the optical selection rules and gives insight about the low lying magnetic and lattice excitations, is the focus of this section. In particular the electrodynamic consequences for the coupling term equation 1.7 are theoretically explored.

1.4.1   Dynamics of Spiral Magnets

The theory of dynamical spin configurations was first summarized by Nagamiya [33] in 1967. He also studied the spin wave spectrum of these types of system. Here this model is applied to the symmetry of RMnO$_3$.

The Hamiltonian that is capable of describing the spiral structure as the ground state

is the following

$$\mathcal{H} = -J\sum_i S_i \cdot \left(S_{i+\frac{b+a}{2}} + S_{i+\frac{b-a}{2}}\right) + \sum_{i\lambda}\left[J_\lambda S_i \cdot S_{i+\lambda} + K_\lambda \left(S_i^\lambda\right)^2\right] \tag{1.10}$$

where $\lambda = a, b, c$. The first term corresponds to the nearest neighbor ferromagnetic interaction in the $a - b$ layers, the second term is the next nearest neighbor interaction along the three axes, and the last term is the single ion anisotropy, which in this case favors the $b - c$ easy plane. J_c is antiferromagnetic, and $J_a > \frac{J}{2}$ frustrates the ferromagnetic ordering in the $a - b$ plane favoring a cycloidal spiral state with wave vector $\mathbf{Q} = (0, Q, 0)$ with $\cos(\frac{Q}{2}) = \frac{J}{2J_b}$. For $K_a > 0$ and $K_b = K_c = 0$ a circular spiral in the $b - c$ plane is the ground state.

The spin spiral configuration in the $b - c$ plane, as in TbMnO$_3$, is given by

$$S_i = \pm S\left(\hat{c}\cos(\mathbf{Q}\cdot\mathbf{r_i}) - \hat{b}\sin(\mathbf{Q}\cdot\mathbf{r_i})\right), \tag{1.11}$$

where the upper/lower sign corresponds to different $a - b$ planes of the structure. In order to facilitate the algebra later on, a transformation of coordinates to the rotating spin frame

$$\hat{z} = \pm\left(\hat{c}\cos(\mathbf{Q}\cdot\mathbf{r_i}) - \hat{b}\sin(\mathbf{Q}\cdot\mathbf{r_i})\right)$$

$$\hat{x} = \mp\left(\hat{c}\sin(\mathbf{Q}\cdot\mathbf{r_i}) + \hat{b}\cos(\mathbf{Q}\cdot\mathbf{r_i})\right) \tag{1.12}$$

$$\hat{y} = \hat{a}$$

in which the average spin vector is parallel to the $\hat{z}$ axis. In this frame the spiral structure is invariant under the simultaneous shift of the spins along $\mathbf{Q}$ and rotation around the a

19

axis. Applying a Holstein-Primakoff [34] transformation to the spin variables

$$S_i^z = S - a_i^\dagger a_i$$

$$S_i^- \approx \sqrt{2S} a_i^\dagger \qquad (1.13)$$

$$S_i^+ \approx \sqrt{2S} a_i$$

for one of the $a-b$ planes, for the other the operator a is replaced by b. The spectrum can be found by diagonalizing the quadratic boson Hamiltonian $\mathscr{H}$ (equation 1.10), and it consists of two branches

$$\omega_{\mathbf{k}}^\pm = S\sqrt{U_{\mathbf{k}}^2 - (V_{\mathbf{k}} \pm W_{\mathbf{k}})^2} \qquad (1.14)$$

where

$$U_{\mathbf{k}} = -4J\left(\cos^2\frac{Q}{4}\cos\frac{k_a}{2}\cos\frac{k_b}{2} - \cos\frac{Q}{2}\right) + 2J_b\left(\cos^2\frac{Q}{2}\cos k_b - \cos Q\right)$$
$$+ 2J_a(1 - \cos k_a) + 2J_c + K \qquad (1.15)$$
$$V_{\mathbf{k}} = -4J\sin^2\frac{Q}{4}\cos\frac{k_a}{2}\cos\frac{k_b}{2} + 2J_b\sin^2\frac{Q}{2}\cos k_b + K$$
$$W_{\mathbf{k}} = 2J_c\cos\frac{k_c}{2}$$

The magnon modes from branch $\omega_{\mathbf{k}}^-$ correspond to spin oscillations normal to the spiral plane, and from the branch $\omega_{\mathbf{k}}^+$ correspond to oscillations within the plane. A typical dispersion of the spin waves is shown in figure 1.6. At $\mathbf{k} = 0$ $\omega_{\mathbf{k}}^+ = 0$ and this mode is called the phason (or Goldstone boson) of the spiral, and it corresponds to the uniform in-phase oscillations of neighboring spins in the $b-c$ plane.

The spin waves at the point Q in the dispersion are significant with respect to the dynamic magnetoelectric effect, as will be seen below. The spins oscillate at $\pm Q$, from

20
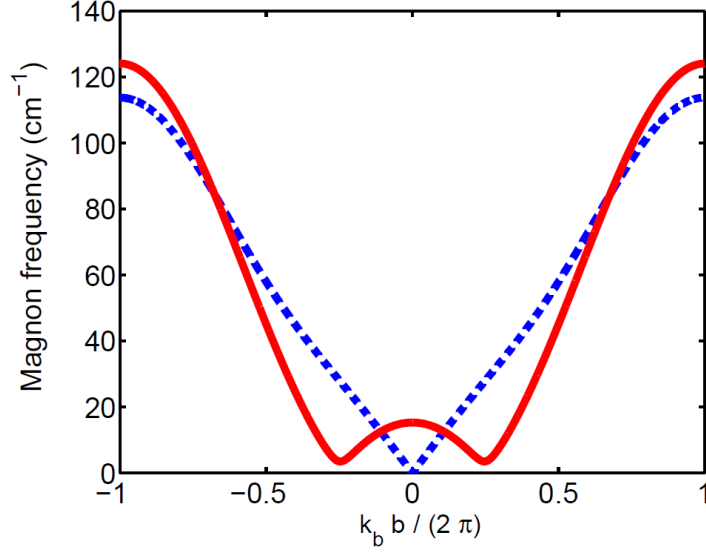
Figure 1.6: Typical spin wave spectrum of a circular spiral. Blue dashed line corresponds to $\omega_{\mathbf{k}}^{+}$ and red solid line to $\omega_{\mathbf{k}}^{-}$.

the $\omega_{\mathbf{k}}^{-}$ branch, with relative phases $Qb/2$ along wave vector direction. Because of the finite easy plane anisotropy K this oscillation is elliptical and there will be a small uniform oscillating spin component in the plane perpendicular to the wave vector. This small uniform component makes this mode active to an imposed oscillating magnetic field $h_\omega \perp Q$. A static magnetic field applied parallel to Q splits this mode into two magnetically linearly polarized modes, and in the case of TbMnO$_3$ the selection rules are $h_\omega \| a, c$. These two modes correspond to linear combinations of the magnon states at $\pm Q$ and are called *antiferromagnetic resonance* (AFMR). Note that if $K_b \neq 0$ or $K_c \neq 0$ these modes are always non-degenerate, even in zero static magnetic field.
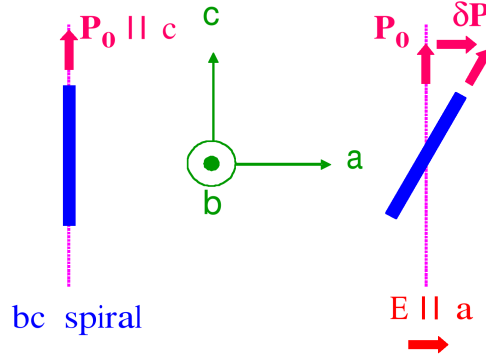
Figure 1.7: Schematic representation of the dynamical magnetoelectric coupling induced by the excitation of the magnon from the "-" branch with $\mathbf{k} = Q$

1.4.2 Magnetoelectric dynamics in spiral magnets

The frequency of the magnons from the "-" branch at $\pm Q$ is $\omega_Q^- \approx 4\sqrt{2J_c K}$. One of the linear combinations $(S_Q - S_{-Q})$ can be visualized as the rotation of the spiral plane around the direction of the wave vector. This is because the static phase difference between spins cancels the phase difference introduced by the spin wave exactly. According to equation 1.3, the direction of polarization is perpendicular to both Q and the spiral plane, and if the spiral plane *rotates* around Q induced by the spin wave, the direction of $\mathbf{P}$ must follow this rotation creating an oscillating $\delta\mathbf{P}$ in the direction perpendicular to the spiral plane.

As indicated in figure 1.7, using again the symmetry of TbMnO$_3$, this oscillation is in fact active for $e_\omega \| a$, making it an *electromagnon*, an electric-dipole active magnon, as

22

opposed to the usual AFMR described above. The selection rule of this electromagnon is tied to the spiral plane, meaning that if this plane changes then the selection rule must follow it. This feature offers the advantage of direct experimental testing if two multiferroics with different spiral planes can be found.

1.5   Ferroelectric Phase Transition

As it has been pointed out in the previous sections, ferroelectricity in multiferroics only appears as a consequence of the breaking of inversion symmetry by special magnetic structures. It is natural then to question how this origin of ferroelectricity differs from the standard ferroelectrics. In this section a phenomenological treatment of ferroelectricity is outlined that serves as context in the understanding of the lattice dynamics of multiferroic materials.

A ferroelectric material is identified with the existence of a macroscopic spontaneous electric polarization that is switchable by an externally applied electric field. In this sense it is common to think that the polarization is just the macroscopic dipole moment, obtained from the charge density, divided by the system volume. However this definition runs into severe trouble when a microscopic model based on this idea is formally developed. The solution to this problem is given by what is now known as the *Modern Theory of Polarization* [35, 36, 37]. This theory says that the polarization as defined above is ill-defined, that only polarization differences between 2 different polarization states are real, i.e. measurable (for example between a paraelectric and

ferroelectric phases, or between 2 distinct ferroelectric phases).

In this modern picture the measurable macroscopic polarization is given by the integrated current generated when the crystal *adiabatically* changes from one state to the other. Because of this, the only requirements to calculate the value of the polarization are the ground state wave functions of the crystal in the two states. This property of the theory has allowed the *ab initio* calculation of the ferroelectric properties of many oxides (see for example K. Rabe and P. Ghosez in [38] for a short review). It is outside the scope of this introduction to delve any further into the details of this modern theory of polarization, however it is necessary to point out the importance of the crystal symmetry in this discussion. As suggested in the above outline, the change in symmetry of the crystal is the key ingredient in describing the change in current whose integral is the spontaneous polarization. Therefore, a survey of the structural phase transition associated with the change in state is the next step in our introduction to the basic physics of ferroelectrics.

From the structural point of view, ferroelectric polarization can only exist in crystals whose symmetry contains a polar axis, that is, a crystal whose space group is polar. Therefore the standard study of ferroelectric transitions considers as a reference state a dielectric crystal that is non-polar, and as a final state the polar ferroelectric state. In this case the structural change implies a macroscopically uniform deformation of the lattice. This is usually described as the instability of the lattice to a phonon which tries to restore the symmetry of the reference state, wherein at the transition temperature the

frequency of this phonon vanishes, it is called a soft-phonon. Because the symmetry lost at the ferroelectric transition is discrete, the frequency of this phonon is only zero at the critical temperature, and increases as the temperature changes away from the transition. Also, this requires that the phonon be polar, i.e. electric dipole or infrared active. This type of description was developed by Cochran [39, 40] and led to the understanding of the ferroelectric phase transitions as being soft-mode driven.

There is a fundamental relation between the static and dynamic dielectric response in matter [41], represented in the Kramers-Kronig [42, 43] relation (see Chapter 2)

$$\varepsilon'(0) - \varepsilon'(\infty) = \frac{2}{\pi} \int_0^\infty \frac{\varepsilon''(\omega')}{\omega'} d\omega' \tag{1.16}$$

which relates the static dielectric function to the frequency dependence of the absorptive part of the dielectric function. Here $\varepsilon'(\infty)$ is the value of the dielectric function at frequencies much higher than the relevant energy scales of the problem. This relation says that any absorption process that contributes to ε'', i.e. electric dipole active, gives a finite contribution to the static dielectric function. This connection immediately implies that in a ferroelectric phase transition the static ε' diverges because the frequency of the infrared soft-phonon goes to zero. This is usually expressed in the Lyddane-Sachs-Teller relation

$$\frac{\varepsilon'(0)}{\varepsilon'(\infty)} = \frac{\omega_{LO}^2}{\omega_{TO}^2} \tag{1.17}$$

where ω_{LO} (ω_{TO}) corresponds to the zero (pole) of $\varepsilon(\omega)$, and also is the longitudinal (transverse) optical phonon frequency.

25

The above discussion has focused on the so called *displacive* ferroelectric transition, in which it is assumed that polarization appears uniformly in the whole crystal as the temperature is lowered below the critical temperature (T_C) because the lattice distortion only occurs below T_C and is zero above it. In this case the symmetry-restoring soft-mode is in fact a uniform polar phonon (**k**=0, Brillouin zone center). However, there is another type of ferroelectric transition, in this other case it is assumed that the lattice is distorted locally but without any coherence over the whole crystal, and long-range order of this local distortions only occurs below T_C. This transition is of the *order-disorder* type. The symmetry-restoring mode is now a relaxation mode centered at zero frequency that exists in addition to the symmetry allowed phonons. In real materials the transition is always somewhere in between these two extremes.

Because of the Kramers-Kronig relation 1.16 the frequency dependence of $\varepsilon(\omega)$ is a very important tool in studying the physics of ferroelectric phase transitions. Given that polar phonons are infrared active, they contribute significantly to $\varepsilon'(0)$, specially if their frequency is low. It is now clear why the lattice dynamics of multiferroics are important, first one needs to identify the soft-phonon or relaxation process that plays the role of the symmetry restoring mode at the transition, secondly, because the magnetoelectric coupling is in fact responsible for the appearance of ferroelectricity, the effect on the lattice dynamics of this coupling deserves investigation.

1.6 Summary

In this chapter a short introduction to the topic of multiferroics was given. The basic mechanisms of magnetoelectric coupling were outlined in a molecule-like picture. Then the magnetoelectric coupling was explored phenomenologically with a symmetry analysis of the magnetic order parameters in two prominent families of multiferroic materials, that allowed the construction of the magnetoelectric interaction term, and then the derivation of the form of the polarization is possible. One of these interactions was used as an example of the dynamic magnetoelectric effects that are possible in multiferroics, this allowed the study of the interaction of the fundamental excitations in magnetic and ferroelectric materials: spin-waves and polar phonons, respectively. This interaction produces a hybrid new elementary excitation, which is called electromagnon, a magnon that interacts with the electromagnetic field of light via an electric dipole coupling. Finally, the lattice dynamics of ferroelectric transitions were outlined, in particular the concept of soft-phonon was emphasized as the most important dynamic effect in ferroelectrics.

The rest of the dissertation is organized as follows. Chapter 2 deals with the experimental methods used in the study of the electrodynamic response of multiferroic materials. Chapter 3 contains results of the polar lattice dynamics in $R\mathrm{Mn_2O_5}$, dealing specifically with evidence of inversion symmetry loss at the ferroelectric phase transition. Chapter 4 focuses on the investigation of electromagnons in $R\mathrm{Mn_2O_5}$, as well as with a theoretical picture that captures the main experimental results. Chapter 5 deals

with electromagnons in $Eu_{0.75}Y_{0.25}MnO_3$ and $TbMnO_3$, results of the temperature and magnetic field dependence are combined with another theoretical model that explains the physics. Finally Chapter 6 gives a summary of the results in addition to avenues for further experimental studies in these families of multiferroics.

Chapter 2

Experimental Methods

The main experimental technique described in this chapter is Fourier Transform In-
frared spectroscopy (FTIR). This technique allows the extraction of the electrodynamic
response of materials as measured in their transmission and reflection spectra. By com-
bining these spectra it is possible to obtain the response function of the material to elec-
tromagnetic waves encoded in the complex index of refraction $n(\omega) = \sqrt{\varepsilon(\omega)\mu(\omega)}$. In
the end the relevant response functions are the dielectric and magnetic susceptibilities
ε and μ, which describe the behavior of the material to electric and magnetic fields,
respectively.

The following sections describe briefly the principles of FTIR and their implemen-
tation in real experiments. Additionally, other apparatus used in the study of the tem-
perature and magnetic field dependencies of the electrodynamic response of materials
are described. Finally, the analysis methods used for the extraction of ε and μ from the
measured spectra are presented.

2.1   Principles of FTIR

The essential problem of any spectroscopic technique is the measurement of the
intensity of light as a function of frequency. FTIR has the advantage of measuring the

intensity distribution in a broad frequency range simultaneously using a single detector. The basic layout of an FTIR instrument is sketched in figure 2.1. The interferometer consists of a half-silvered beamsplitter (BMS), one fixed and one moving mirror, a source and a detector. The transmitted and reflected waves from the BMS travel to the mirrors, the moving mirror travels a distance d from the ZPD point (zero path difference), the corresponding path length is then $x = 2d$. The reflected beams recombine at the BMS and then are focused to the detector. The detector signal varies with the optical path length x and is maximal at ZPD and corresponds to constructive interference. As x changes, the relative length between the 2 beams varies and this is recorded as a time-varying signal in the detector. This time dependent detector signal is the Fourier transform of the source power spectrum and is called an *interferogram*.

The electric field amplitude at the detector as a function of frequency ν and x can be expressed as

$$E_{det}(x,\nu) = E_1(\nu) + E_2(\nu)e^{\iota \Delta \theta(x,\nu)} = rtE_0(\nu)(1 + e^{\iota 2\pi \nu x}) \tag{2.1}$$

where r and t are the reflection and transmission coefficients, respectively, of the BMS, which ideally equal $\frac{1}{2}$. Therefore, the intensity measured at the detector is

$$I(x,\nu) = \frac{c}{4\pi}|E_{det}(x,\nu)|^2 = 2|rt|^2 S(\nu)[1 + \cos(2\pi \nu x)], \tag{2.2}$$

here $S(\nu) = \frac{c}{4\pi}|E_0(\nu)|^2$ is the power spectrum of the source. By superposition, the total signal at the detector for a broadband source results from an integration over the
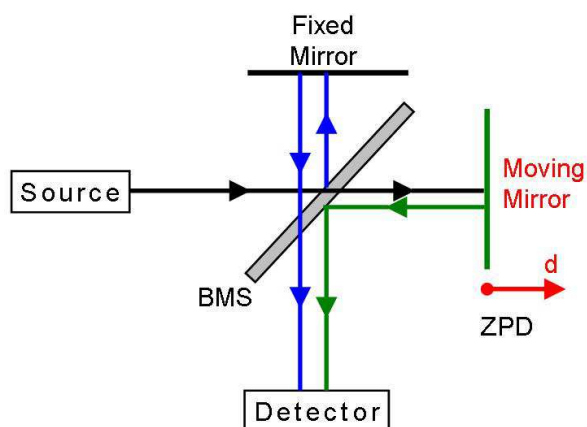
Figure 2.1: Schematic of the Twyman-Green version of the Michelson interferometer as usually implemented in an FTIR instrument.

frequency range of the source

$$I(x) = 2|rt|^2 \left[\int_0^\infty S(\nu)\mathrm{d}\nu + \int_0^\infty S(\nu)\cos(2\pi\nu x)\mathrm{d}\nu \right] = \frac{1}{2}I(0) + I_{int}(x) \qquad (2.3)$$

where $I_{int}(x)$ is the interferogram and it consists of the cosine-Fourier transform of the incident light as a function of the mirror position x. In other words, the translation of the moving mirror transforms the power spectrum of the source into a positional (or temporal via $t = x/v$ where v is the mirror speed) spectrum. The original power spectrum $S(\nu)$ can be recovered using the inverse cosine Fourier transform of $I_{int}(x)$, and modern computers can perform this operation in real time using the fast Fourier transform algorithm.

FTIR spectrometers have very important advantages over other types of spectrom-

eters. In order to compare these the most important features of a generic spectrometer are: (1) throughput or how much light passes through, (2) chromatic resolving power (resolution) or how close two spectral features can be before they become indistinguishable in the interferogram, and (3) cost or how fast the interferogram can be obtained with a fixed signal to noise (S/N) ratio. FTIR offers the advantage of multiplexing, because it simultaneously detects all frequencies, and therefore its cost is small. In a grating spectrometer it takes a time $T = m\tau$ to measure m intervals in a frequency range if for each frequency measured it takes a time τ to make the measurement. For a FTIR spectrometer the same time T can be used to repeat m measurements of the entire frequency range, this reduces the S/N by a factor of $\sqrt{m}$. In terms of throughput the FTIR spectrometer is also superior to traditional grating spectrometers because the solid angle of the light beam is very large for the FTIR whereas it is rather small for a grating spectrometer. The resolution of an ideal FTIR is $\delta \sim 1/2d$, therefore, very high resolution will require very long displacements of the moving mirror and this complicates the engineering of the real instrument and it also undermines the speed at which the interferograms can be obtained.

Other issues regarding the asymmetry of the interferograms, apodization and aliasing have to be carefully consider when utilizing a real FTIR instrument. The correct power spectrum $S(v)$ can be obtained from the inverse cosine Fourier transform only if the interferogram is symmetric. For an asymmetric interferogram a phase correction has to be applied to the measured interferogram to yield a symmetric one. Because

real spectrometers can only scan over a finite distance, the measured interferogram is truncated. This truncation introduces spurious effects like side lobes near sharp spectral features. This effects can be minimized when apodizing functions are applied to the interferogram at the expense of spectral resolution. Aliasing refers to the discrete sampling of the signal that is performed during the mirror displacement, this implies that when the Fourier transform is performed, the spectrum is repeated multiple times, or aliased. Thus any real intensity in the power spectrum above the maximum frequency of the desired frequency range, is *folded back* into the transformed spectrum and introduces errors in the signal. Electronic, numerical and optical filtering of these signals can be used to minimize aliasing.

2.2   Apparatus

The FTIR spectrometer used in this research is the DA3.02 FTIR spectrometer by ABB-Bomem (Québec, Canada). The main layout is as shown in figure 2.1. The sample compartment of this spectrometer is divided into a transmission and a reflection part as shown in figure 2.2. This device offers a range of spectral resolutions from 64-0.02 cm^{-1}, and works in the frequency range of 5-50000 cm^{-1} using a variety of sources, beamsplitters and detectors. The DA3 spectrometer system manual provides further detail of its operation [44].

The DA3 offers three main broadband blackbody radiation sources. A mercury vapor discharge (Hg) lamp for the far IR ($\nu < 250$ cm^{-1}), a globar for the mid-IR
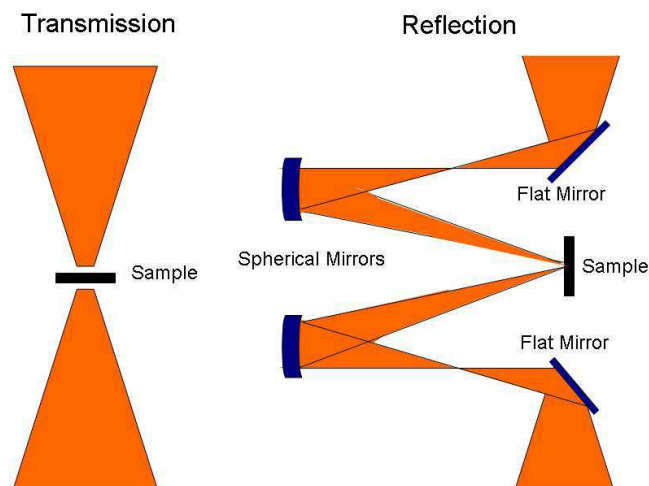
Figure 2.2: Schematic of the Transmission (left) and Reflection (right) geometries in the FTIR instrument.

(100-8000 cm^{-1}) and a quartz tungsten halogen lamp for the visible region of the spectrum (4000-25000 cm^{-1}). Several beamsplitters are available that match the different frequency regions of the sources, in particular for the far IR a Si beamsplitter (0-1000 cm^{-1}) was used throughout the course of this research. Finally, as detectors resistive-bolometers were used for the far-IR: a standard liquid-He cooled bolometer (4K bolometer) was used in the range 100-700 cm^{-1}, a pumped liquid-He bolometer (2K bolometer) was used for the range 5-250 cm^{-1}, and in addition a He-3 cooled bolometer (He-3 bolometer) working at 350 mK was used in the range 3-60 cm^{-1}.

Sample temperature control in zero magnetic field is achieved with the use of an optical cryostat (optistat) manufactured by Janis Research Corporation. Figure 2.3 shows
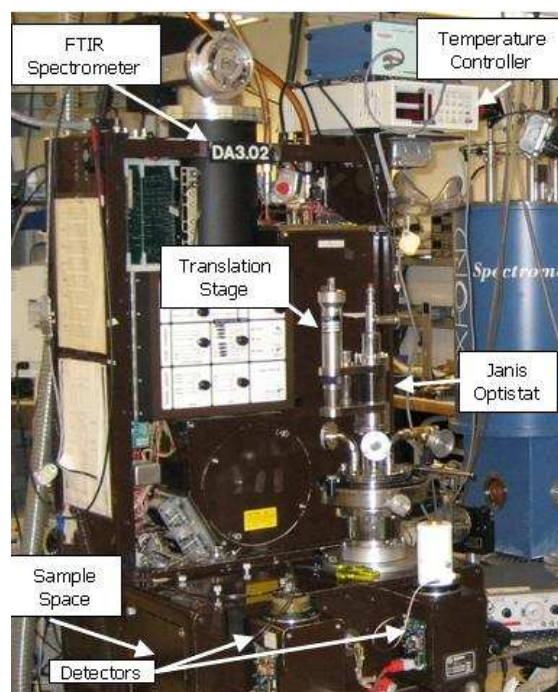
Figure 2.3: Bomem DA3.02 Spectrometer and Janis optistat in reflection mode.
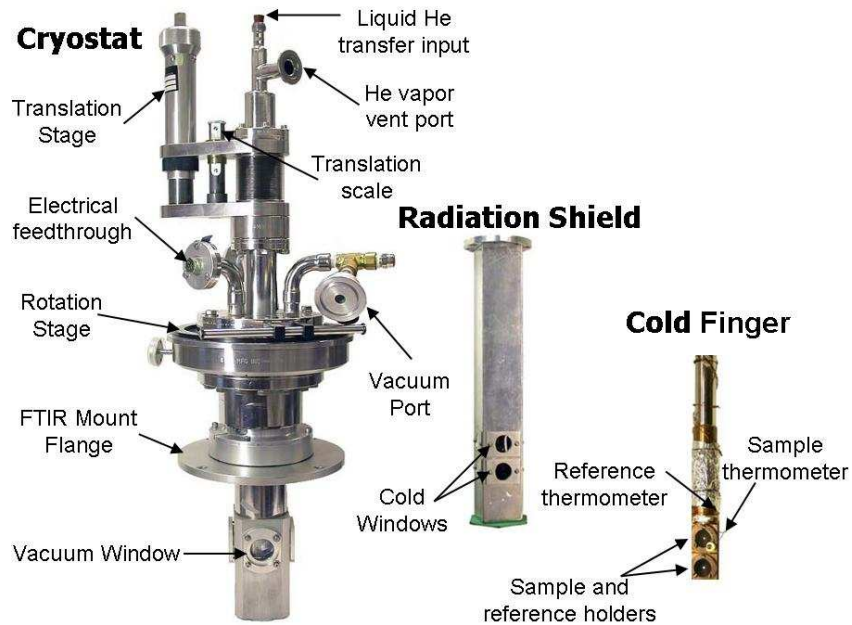
Figure 2.4: Janis optistat.

the optistat in the reflection mode of the DA3 instrument. Details of the Janis optistat

construction are shown in figure 2.4. Cooling is achieved by continuous flow of liquid

He through a transfer line directly into the cryostat. The liquid He cools down the in-

terior all the way down to the sample mounted on a cold finger. The cooling is made

more effective by using the radiation shield, this part is in contact with the flowing He

and is cooled as well. By using cold windows as filters, a large amount of ambient room

temperature radiation can be prevented from reaching the sample. In this configuration

temperatures of 5 K can be reached when studying the far IR response of samples.

For the investigation of the magnetic field dependence of the electrodynamics of

multiferroics, a connection with an existing Oxford Magnet was developed. The Oxford
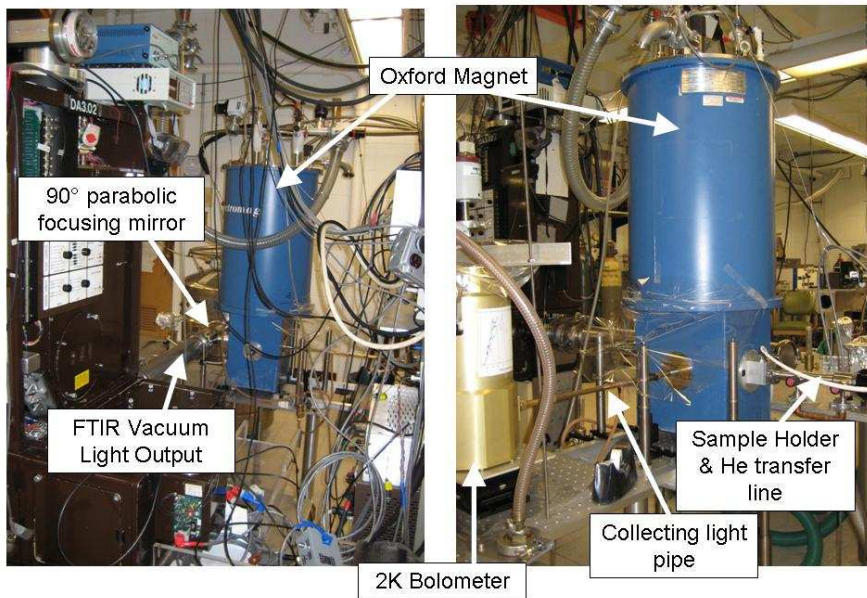
Figure 2.5: FTIR to magnet connection.

Optical Cryostat, manufactured by Oxford Instruments Inc., allows the application of an static magnetic field up to 8 Tesla in the direction of propagation of light. Its split-coil geometry facilitates its use as a true optical cryostat where standard focusing and light collecting optics can be used. Figure 2.5 shows the FTIR connection with the magnet during one of the experimental runs. Light is extracted out of FTIR via a collimated parallel output beam, which is then focused onto the sample with an off-axis parabolic mirror. The focused beam then enters the magnet and reaches the sample in the middle of the housing where the magnetic field is maximum and uniform. The transmitted beam is then collected with a copper light pipe of half-inch diameter. This light pipe functions as a waveguide with a cut-off wavelength of approximately one half of the diameter.
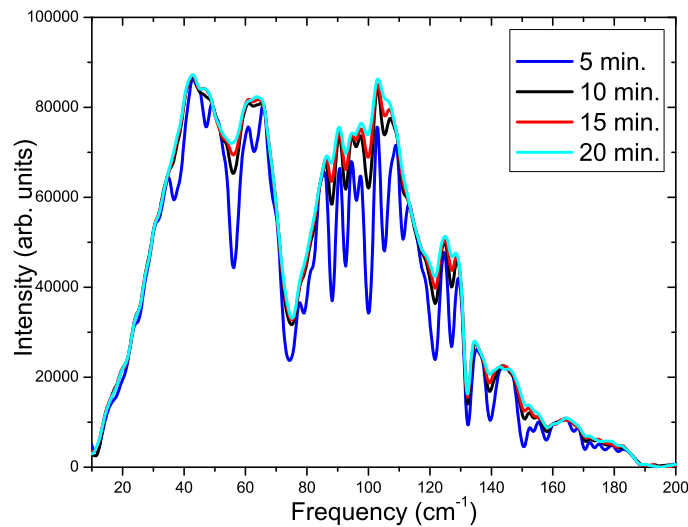
Figure 2.6: Transmission signal after the start of Nitrogen gas flow.

The connection between the DA3 and the Oxford magnet is not fully in vacuum. This means that water vapor absorption in the far IR will complicate the analysis of the obtained spectra. In order to minimize this, all the volumes not in vacuum, are purged with cold Nitrogen gas obtained from the boil-off of the liquid Nitrogen in the magnet itself. This effectively eliminates any signal of water vapor absorption in the resulting spectra. Figure 2.6 shows the time evolution of the transmission signal in this configuration after the flow of Nitrogen gas started. After approximately 30 minutes, there are no distinguishable traces of water vapor absorptions and then measurements on the samples are performed.

Further details of the experimental apparatus can be found in the PhD thesis of the previous students of the group, Jeffrey Simpson [45] and Gregory Jenkins [46].

38

2.3 Optical Constants

2.3.1 Basic Definitions

As mentioned in the first paragraphs of this chapter, the electrodynamic response of materials is encoded in the optical constants such as the complex index of refraction $n(\omega) = \sqrt{\varepsilon(\omega)\mu(\omega)}$. It is usually assumed that the magnetic effects in solids are small [41], however consideration should be given to them in multiferroic materials because they are partly magnetic. Nevertheless, the magnitude of the magnetic effects, even in resonant conditions, is much smaller than the corresponding electric effect and therefore it is assumed that $\Re[\mu] = \mu_1 \sim 1$ and $\Im[\mu] = 0$ in the following description (where $\Re$ and $\Im$ take the real and imaginary parts of a complex function).

The response of matter to an electric field is given by the complex dielectric permittivity ε because it relates the electric field $\mathbf{E}$ with the electric displacement $\mathbf{D} = \varepsilon\mathbf{E}$.

$$
\begin{aligned}
\varepsilon &= \varepsilon_1 + \varepsilon_2 &= n^2 \\
&= (n_1 + \iota\kappa)^2 &= n_1^2 - \kappa^2 + \iota 2n_1\kappa
\end{aligned}
\tag{2.4}
$$

where κ is the imaginary part of the index of refraction and is usually called the extinction coefficient. The complex electrical conductivity $\sigma = \sigma_1 + \iota\sigma_2$ is related to ε in the following way because it relates the electric field with the motion of charges $\mathbf{J} = \sigma\mathbf{E}$

$$
\varepsilon = 1 + \iota\frac{4\pi}{\omega}\sigma
\tag{2.5}
$$

Based on this equation, the large majority of optical measurements are described using

ε_1 and σ_1 given that they describe the absorptive (σ_1) and screening (ε_1) part of the electrodynamic response in materials.

2.3.2 Kramers-Kronig Relations

As mentioned in Chapter 1 there exists a fundamental relation between the static response functions and their frequency dependence (see equation 1.16). This is a consequence of more fundamental characteristics of response functions, which are causality and linearity. Causality means that a response of a system cannot occur before the stimulus is applied, and linearity refers to the fact that the stimulus is weak enough that the response itself does not depend on its intensity. In this case both ε and μ are called linear response functions.

Let us assume that a stimulus field $\mathbf{H}$ is applied to a system, and its response is measured in the field $\mathbf{M}$. The linear response function relating them is χ

$$\mathbf{M} = \chi\mathbf{H} \tag{2.6}$$

where $\chi = \chi_1 + \iota\chi_2$. Using causality and the properties of analytical complex functions the dispersion relations can be derived, and are:

$$\chi_1(\omega) = \frac{1}{\pi}\mathscr{P}\int_{-\infty}^{\infty}\frac{\chi_2(\tilde{\omega})}{\tilde{\omega}-\omega}d\tilde{\omega} \tag{2.7}$$

$$\chi_2(\omega) = -\frac{1}{\pi}\mathscr{P}\int_{-\infty}^{\infty}\frac{\chi_1(\tilde{\omega})}{\tilde{\omega}-\omega}d\tilde{\omega} \tag{2.8}$$

where $\mathscr{P}$ is the Cauchy principal value integral. In the realm of complex analysis χ_1 and χ_2 are said to be Hilbert transformed pairs of each other [47].

Equations 2.7 and 2.8 can be applied to $\varepsilon(\omega)$. Taking advantage of the symmetry property $\varepsilon(-\omega) = \varepsilon^\star(\omega)$ these can be simplified further, and these are the Kramers-Kronig relations:

$$\varepsilon_1(\omega) - 1 = \frac{2}{\pi} \mathscr{P} \int_0^\infty \frac{\tilde{\omega}\varepsilon_2(\tilde{\omega})}{\tilde{\omega}^2 - \omega^2} d\tilde{\omega} \tag{2.9}$$

$$\varepsilon_2(\omega) = -\frac{2}{\pi\omega} \mathscr{P} \int_0^\infty \frac{[\varepsilon_1(\tilde{\omega}) - 1]\tilde{\omega}^2}{\tilde{\omega}^2 - \omega^2} d\tilde{\omega} \tag{2.10}$$

A natural consequence of the Kramers-Kronig relations are the so called sum-rules. Equation 1.16 can therefore be obtained from equation 2.9 by taking the limit $\omega \to 0$. If we cast these relations in terms of the electrical conductivity σ the sum-rule has the form

$$\varepsilon_1(0) - 1 = 8 \int_0^\infty \frac{\sigma_1(\omega)}{\omega^2} d\omega \tag{2.11}$$

which signifies that very low frequency absorptive excitations will greatly enhance the zero frequency value of the dielectric function. This clearly indicates that the static measurements of ε_1 are incomplete until a detailed spectroscopic study is performed on the absorption spectrum of a material.

2.3.3 Experimental Procedure

There are several experimental techniques that can be used to obtain the optical constants n, ε and μ. The two most used ones are the reflection from and transmis-

sion through the sample of electromagnetic waves. The Fresnel formulas for the bulk transmission and reflection coefficients are widely used in the community

$$\mathscr{R}(\omega) = \left| \frac{1-n(\omega)}{1+n(\omega)} \right|^2 = \frac{(1-n_1(\omega))^2 + \kappa(\omega)^2}{(1+n_1(\omega))^2 + \kappa(\omega)^2} \qquad (2.12)$$

$$\mathscr{T}(\omega) = \frac{4n_1(\omega)}{(n_1(\omega)+1)^2 + \kappa(\omega)^2} \qquad (2.13)$$

in this case $R+T=1$ because this case is only considering reflection and transmission through a boundary between air and a material of index of refraction $n(\omega) = n_1(\omega) + \iota\kappa(\omega)$. A more relevant case is when light is transmitted through a slab of material of thickness d,

$$\mathscr{T}(\omega) = \frac{\mathscr{T}_{01}\mathscr{T}_{12}\exp[-\alpha d]}{1 - 2\mathscr{R}_{01}\cos[2(\theta_1+\phi_1)]\exp[-\alpha d] + \mathscr{R}_{01}^2\exp[-2\alpha d]} \qquad (2.14)$$

$$\alpha(\omega) = \frac{2\kappa(\omega)\omega}{c} \qquad (2.15)$$

$$\theta_1(\omega) = \arctan\left[\frac{\Im(r_{10})}{\Re(r_{10})}\right] \qquad (2.16)$$

$$\phi_1(\omega) = \frac{n_1(\omega)\omega d}{c} \qquad (2.17)$$

where $\mathscr{T}_{01}$, $\mathscr{T}_{12}$ are the transmission coefficients of the boundaries air–slab and slab-air, respectively, $\mathscr{R}_{01} = |r_{01}|^2$ is the reflection coefficient between the slab and air.

With formulas 2.12 and 2.14 then we can start analyzing experimental data by using as fit parameters the index of refraction n_1 and the absorption coefficient α, thus this allows the extraction of $\varepsilon(\omega)$ from the measurements.

2.3.3.1 Electric Dipole and Magnetic Dipole Excitations

The discussion of the optical constants above was focused on the frequency dependence of ε, meaning that only electric dipole transitions have been considered. However, materials containing magnetic atoms and/or magnetically ordered, will give rise to magnetic dipole transitions that will contribute to the optical constants in the form of the magnetic permeability $\mu = \mu_1 + \iota\mu_2$. Because the basic equations 2.12 and 2.14 are written as functions of $n(\omega)$ as a complex quantity, the actual information obtained is a combination of electric and magnetic transitions and it seems not possible to disentangle all the desired knowledge from measurements of $\mathcal{R}$ and $\mathcal{T}$. However, there is a feature of the reflection coefficient that allows the distinction between magnetic and electric dipole excitations, at least in simple models for the frequency dependence of ε and μ.

Figure 2.7 shows the Reflectivity and Transmission spectra of a slab of isotropic material characterized by a Lorentzian form of ε and μ with a single oscillator at frequencies marked by black arrows in the figure,

$$\varepsilon(\omega) = \varepsilon_\infty + \sum_j \frac{S_j}{\omega_j^2 - \omega^2 - \iota\omega\gamma_j} \tag{2.18}$$

$$\mu(\omega) = 1 + \sum_j \frac{S_j}{\omega_j^2 - \omega^2 - \iota\omega\gamma_j} \tag{2.19}$$

It is clear from the figure that only by measuring the Reflectivity spectrum one can distinguish magnetic dipole from electric dipole excitations, this is because for electric dipole excitations the reflectivity first increases as the frequency increases from zero,
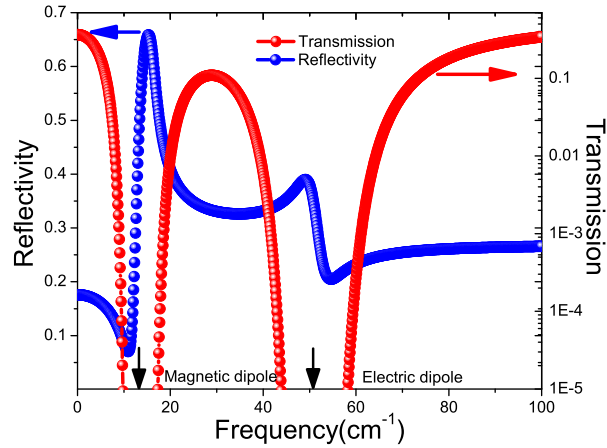
Figure 2.7: Reflectivity and Transmission spectra of an isotropic material with one of each electric and magnetic dipole transitions.

and for magnetic dipole the reflectivity decreases first.

Additionally, magnetic and electric dipole excitations can be distinguished in the Transmission spectra of anisotropic materials. For simplicity let's assume that the crystal symmetry is orthorhombic. In this case the principal axes of the tensors ε and μ correspond to the orthogonal axis of the crystal structure. Figure 2.8 shows the different experimental configurations needed to observe magnetic and electric dipole absorptions. The top panel shows two orientations of the crystal, $x - z$ and $y - z$ planes, and the corresponding direction of the polarized light electric (e_ω) and magnetic (h_ω) fields. Because only $h_\omega \| z$ is absorbed, the excitation is magnetic dipole. The bottom panel shows the case of an electric dipole absorption where only $e_\omega \| x$ is absorbed for the two orientations of the crystal, $x - z$ and $x - y$ planes.

44
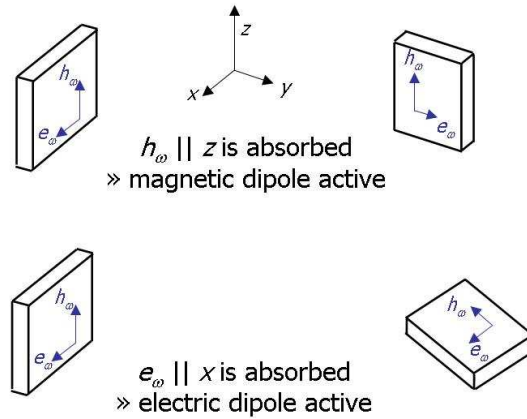
Figure 2.8: Absorption conditions for magnetic dipole and electric dipole excitations.

2.4   Summary

This chapter has outlined the basic experimental and analysis techniques to be used in the rest of the dissertation. The experimental set up used for the spectroscopic studies was described, including the addition of the magnetic field capabilities. Furthermore, the optical properties of materials were outlined together with the basic notions of how to experimentally obtain them. Armed with these tools, the next chapters describe the results of the investigations of the electrodynamics of multiferroic materials.

Chapter 3

Lattice Dynamics in the Multiferroic Family $R\mathrm{Mn_2O_5}$

3.1   Overview

In order to address the questions posed in Chapter 1 regarding the dynamic coupling

between ferroelectric and magnetic orders, a study of the lattice and magnetic excitations

is required. Here results are presented about the lattice dynamics of the multiferroic

family $R\mathrm{Mn_2O_5}$ where R is a rare earth element, Y or Bi.

Figure 3.1 shows the magnetic structure in $R\mathrm{Mn_2O_5}$, this is composed of oxygen

octahedra coordinating $\mathrm{Mn^{4+}}$ which connect at the edges to form ribbons that extend

along the c axis. $\mathrm{Mn^{3+}}$ is located at the base of a oxygen square pyramid, these pyramids

link at one edge of the square and at the other connect the octahedra. The rare earth ion

is located in a site without inversion which creates a special crystal field environment

that splits the $3f$ orbitals, this will become important given that transitions between this

split levels are optically allowed and can appear in the infrared.

3.2   Multiferroics $R\mathrm{Mn_2O_5}$

The antiferromagnet $R\mathrm{Mn_2O_5}$ (orthorhombic space group *Pbam* # 55, Z = 4) is a

multiferroic family of compounds with a complex magnetic order [48, 49, 50, 51, 52]
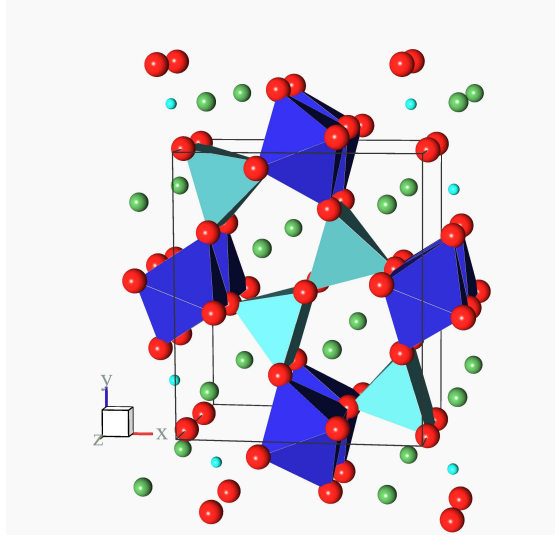
Figure 3.1: Structure of multiferroic TbMn$_2$O$_5$.

that shows a strong magnetoelectric coupling effect. For example in TbMn$_2$O$_5$ [20] an applied magnetic field along the *a* axis changes the sign of the electrical polarization along the *b* axis. The complex magnetism is accompanied by a series of phase transitions between different magnetic states characterized by distinct commensurate and incommensurate phases. The first hint to the magnetoelectric coupling is given by the behavior of the dielectric constant ε. In particular ε in TbMn$_2$O$_5$ has anomalies along the *b* axis associated with the distinct phase transitions at low temperatures as shown in figure 3.2: at the Néel temperature $T_N \approx 42$ K no anomalies are present in ε. There is a paraelectric to ferroelectric phase transition at T$_C \approx 38$ K evident by a peak in the dielectric constant. The magnetic order then locks in to a commensurate structure (CM) with wave vector (1/2,0,1/4). At T $\approx$ 24 K the magnetic order transforms into an incommensurate structure (ICM) with a step-like feature in ε; this anomaly is also
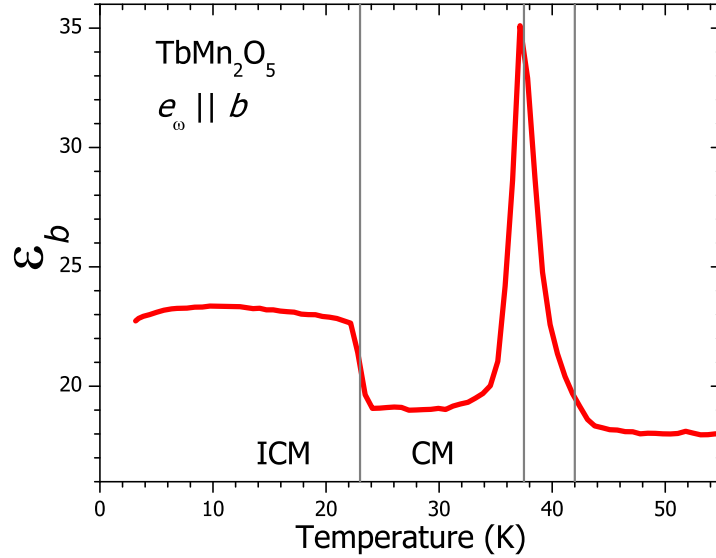
Figure 3.2: Temperature dependence of the dielectric constant along the b axis ε_b in TbMn$_2$O$_5$.

accompanied by hysteresis [20]. Note that the dielectric constants along the a and c axis show no significant effects at these phase transitions.

The existence of a macroscopic dipole moment is evidence of the lack of inversion symmetry in the FE phase, and motivates the study of the dynamics of the lattice to look for further information about the structural changes. In EuMn$_2$O$_5$ it was found [53] that displacements of the Mn^{3+} ion along the a axis occur at the ferroelectric transition. They suggested that this behavior leads to a change in symmetry from the space group Pbam to the non-centrosymmetric group Pb2$_1$m (# 26). In a analogous work on the compound YMn$_2$O$_5$ [54], Kagomiya, et al proposed similar displacements at the ferroelectric transition. These displacements are very small (≈ 0.007 Å), which hints to an exotic origin

of ferroelectricity when compared to the typical ferroelectrics as described in Chapter 1, where a polar lattice distortion creates the macroscopic polarization. Other structural investigations [48, 55, 49] have not reported any signature of atomic displacements at the ferroelectric phase transition in this family of compounds. The lattice dynamics have been investigated by Raman spectroscopy, Mihailova, et al [56] reported a study in $HoMn_2O_5$ and $TbMn_2O_5$ and García-Flores, et al [57] in $BiMn_2O_5$, $EuMn_2O_5$ and $DyMn_2O_5$ as a function of temperature and found no evidence of anomalous behavior of the Raman active phonons at the ferroelectric transition temperature, indicating that the lattice may not play such an important role in the appearance of ferroelectricity on these multiferroics.

This chapter presents a study of the temperature dependent infrared (IR) phonon spectra of the multiferroic $TbMn_2O_5$. The most interesting result is the appearance of an IR inactive phonon activated at the ferroelectric transition with light polarization parallel to the static ferroelectric polarization $\mathbf{P_0}$ ($e\|\mathbf{P_0}\|b$). This indicates that one IR forbidden mode (Raman or silent) in the paraelectric phase acquires an electric-dipole moment due to the static displacement associated with the ferroelectricity. This phonon is identified with a Raman Mn-O stretching mode, which accounts for its sensitivity to the static polarization [9, 49].
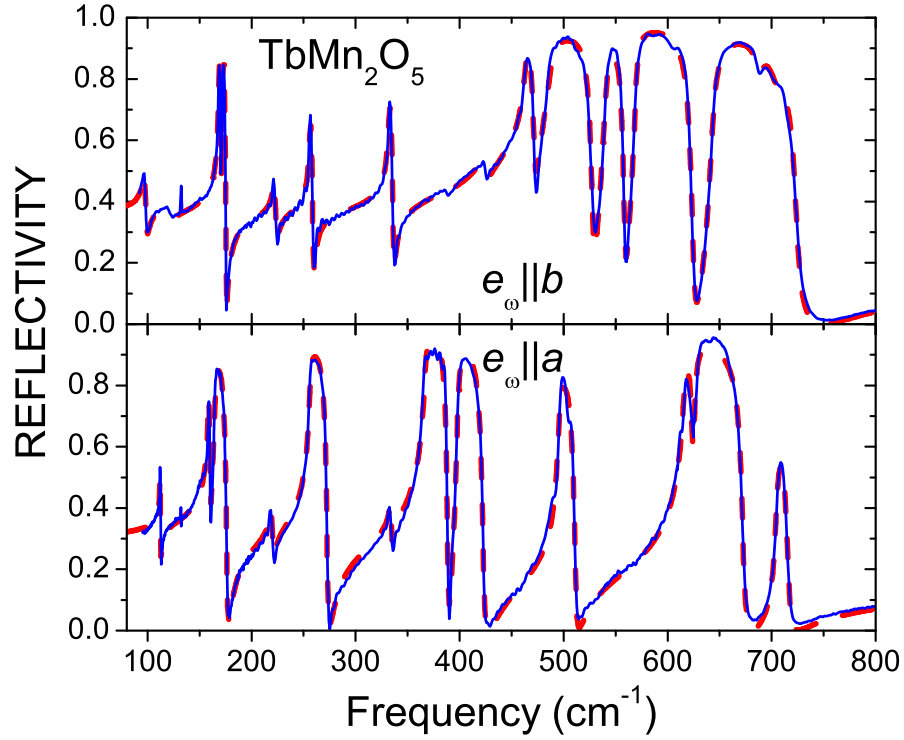
Figure 3.3: Experimental (solid line) and fit (dashed line) at T = 7 K phonon spectra in TbMn$_2$O$_5$.

3.3   Experimental Results

The group theory analysis (see Appendix A) based on structural data by Alonso, et al [58] of the paraelectric phase predicts the following IR active vibrational modes at the Γ point: $\Gamma_{IR} = 8B_{1u}(E||z) + 14B_{2u}(E||y) + 14B_{3u}(E||x)$ identical to a previous report [56]. This analysis was complemented with a shell model calculation of the phonon frequencies.

Figure 3.3 shows the spectra at T = 7 K. Twelve of the 14 IR active phonons in the *a* polarization were reliably observed, whereas all 14 phonons polarized along *b* are present in the spectrum. The reflectivity spectra was fitted in a least squares procedure using the sum of Lorentzian form of the model dielectric function ε, given by:

$$\varepsilon(\omega) = \varepsilon_\infty + \sum_{i=1}^{N} \frac{S_i}{\omega_{0i}^2 - \omega^2 - \iota\gamma_i\omega} \qquad (3.1)$$

where ε_∞ is the dielectric constant at high frequency and the phonon parameters ω_0, S and γ are the phonon frequency, the spectral weight and the linewidth respectively, we also define $S_i = \Delta\varepsilon_i\omega_{0i}^2$ where $\Delta\varepsilon$ is the contribution of the phonon to the static dielectric function; these parameters are extracted as functions of temperature and are displayed in table 3.1. The result of the fitting is also shown in figure 3.3 and it can be seen that it is almost indistinguishable from the data indicating the weakness of higher order phonon processes.

The optical conductivity was obtained from $\varepsilon(\omega)$ from eqn. 3.1 and using the Kramers-Kronig transform of the reflectivity spectrum. Figure 3.4 shows the optical conductivity around 700 cm^{-1} for several temperatures with $e||\mathbf{P_0}||b$. A feature not present at 45 K appears in the low T phases. The temperature dependence of the spectral weight and frequency of this feature are plotted in figure 3.5 where the spectral weight starts to appear at 38 K. *S* for this phonon was obtained by directly integrating the optical conductivity between 695 and 710 cm^{-1}. The spectral weight of this phonon increases and its frequency shifts, both continuously, as the temperature is lowered. Around 24 K both abruptly change and show hysteresis around this point evident by the difference

Table 3.1: Oscillator parameters at T_1 = 7 K and T_2 = 45 K in TbMn$_2$O$_5$. *a, b* are the crystal axes. $\varepsilon_\infty^{a,b} = 5.31, 6.82$.

$\omega_o(cm^{-1})$				$\Delta\varepsilon$				$\gamma(cm^{-1})$			
a		*b*		*a*		*b*		*a*		*b*	
T_1	T_2	T_1	T_2	T_1	T_2	T_1	T_2	T_1	T_2	T_1	T_2
111.9	111.7	97.2	96.4	0.59	0.66	0.42	0.38	1.9	2	3.3	3.7
157.5	157.3	168.9	168.6	0.81	1.05	0.46	0.43	0.9	0.3	1	1.1
164.2	163.8	171.9	171.5	1.68	2.02	0.30	0.35	3.3	2.6	1.4	1.5
218.5	217.4	222.2	221.9	0.30	0.69	0.11	0.11	4.7	8.9	2.4	2.9
254.8	253.2	256.8	256.6	1.88	2.56	0.17	0.18	3.1	1.5	2.1	2
333.1	332.4	333.4	332.7	0.09	0.15	0.17	0.17	2.7	2.6	2.7	2.7
364.9	362.8	386	385.5	2.02	2.75	0.02	0.01	3.9	1	3.5	4
397.6	396.5	422.3	422.3	0.38	0.46	0.28	0.28	4.6	3.2	4	3.5
494.8	493.9	453.2	459.3	0.45	0.59	3.43	3.56	5.3	3.7	18.4	6.7
613.5	611.3	481.8	483	0.71	1.11	2.86	2.6	9	5.4	4.4	3.3
627.5	625.9	538.2	537.6	0.23	0.14	0.25	0.51	8.4	4.2	7.3	7.1
704.2	701.4	567.3	568.4	0.05	0.04	0.52	0.57	3.3	4.5	5.1	7.9
—	—	636.6	637.2	—	—	0.27	0.23	—	—	10.7	9.3
—	—	688.2	686.9	—	—	0.003	0.003	—	—	9.5	6
—	—	703[a]	—	—	—	0.0001	—	—	—	7	—
—	—	120.4[b]	119.5	—	—	0.12	0.10	—	—	5.7	6.4

[a]Previously IR inactive

[b]Crystal field excitation fitted as electric dipole active
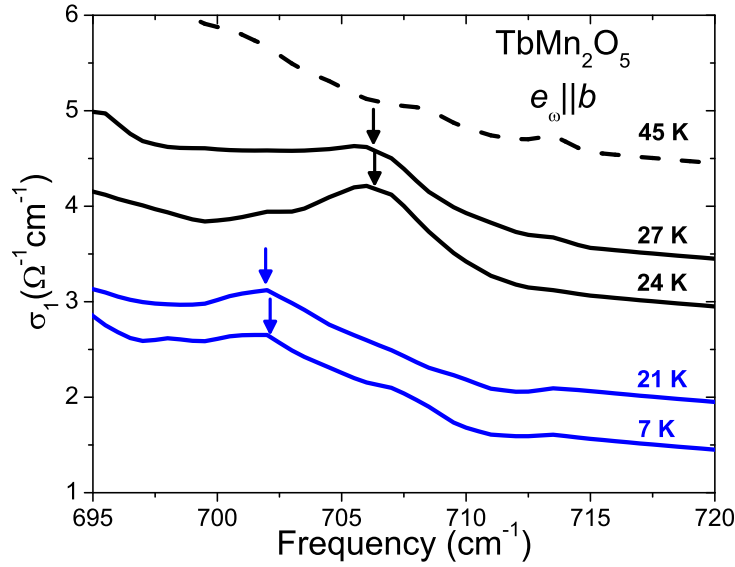
Figure 3.4: Optical conductivity of the newly activated phonon (shifted plots). Arrows indicate the position of the resonance frequency.

in the cooling and warming curves. The behavior of this feature is correlated with the second order FE transition at 38 K and the first order CM → ICM transition at 24 K in this compound. The static polarization $\mathbf{P_0}$ plotted in figure 3.5 was obtained by measuring the temperature dependence of the pyroelectric current on a similar sample to the one used in the optical measurements.

On very general grounds the appearance and behavior of this phonon can be related to these underlying phase transitions. Since the lattice distortions δu associated with these phase transitions are very small we can expand the spectral weight and frequency shifts in powers of δu. The quadratic term is the first non-zero term in this expansion that can describe the spectral weight change or frequency shift. Similarly, the order pa-

rameters associated with the new phases are proportional to δu so that $\mathbf{P_0} \propto \delta u$. As a result we expect that the spectral weight behavior and frequency shift should be S, $\Delta\omega \propto (\delta u)^2 \propto \mathbf{P_0}^2$. This is the observed behavior as can be seen in figure 3.5 where it is plotted $\mathbf{P_0}^2$ with the phonon data. At low temperatures (T < 10 K) where the Tb moment orders, the phonon data deviates from $\mathbf{P_0}^2$ suggesting that it is the Mn and oxygen ion displacements that dominate the dynamics of this high frequency phonon. The possible scenarios for the appearance of a new phonon are: (1) zone folding of the phonon dispersion (since the magnetic order corresponds to a lock in ICM $\rightarrow$ CM transition with $\mathbf{k} = (1/2, 0, 1/4)$), and (2) activation of IR-inactive phonons at this transition due to the loss of inversion symmetry. The shell model calculation shows that the dispersion of the high frequency phonon is negative so that no zone-folded mode can give the high frequency of this phonon. Therefore, this phonon is a previously IR inactive phonon that acquires electric dipole moment at the FE transition.

In a ferroelectric phase transition, where inversion symmetry is lost, symmetry considerations dictate that phonons that were not IR active in the paraelectric phase can become IR active in the FE phase. This is the case in $TbMn_2O_5$, where the low T phase has mixed IR and Raman phonons. In this low T phase the phonons of the high T symmetry group split as shown in table 3.2 [1]. This splitting was obtained by considering what sym-

---

[1]The exact space group for the FE phase in $TbMn_2O_5$ is not known precisely. The assumption has been made of space group # 26 following Polyakov, et al [53] and Kagomiya, et al [54], because this allows to write the direct transformation of each phonon for both space groups. Nevertheless, even if the real crystallographic structure is different, such as the modulated structure in $DyMn_2O_5$[59], the experimental
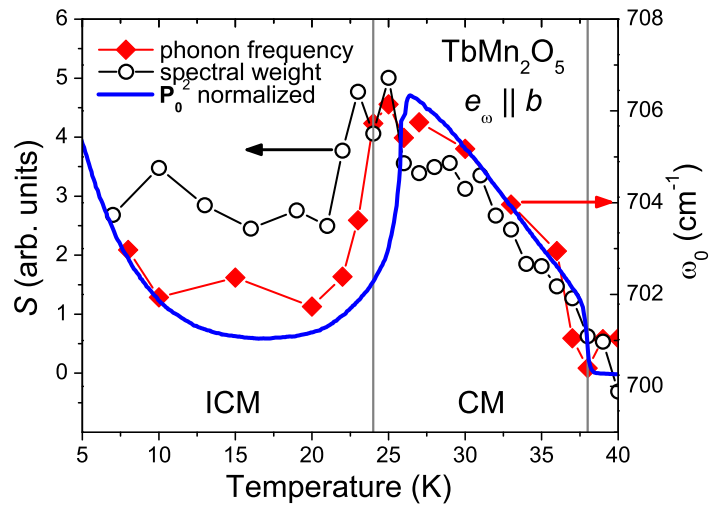
Figure 3.5: Comparison of the behavior of the spectral weight and frequency of the new phonon to the static polarization $\mathbf{P_0}$. Polarization and frequency show warming curves and S shows the cooling curve.

metry operation is maintained in both phases and then assign spectral activity according to the experimental observations. The assumption was made as well that the low T space group is as proposed by Polyakov, et al [53] and Kagomiya, et al [54]. Consistency with the laboratory frame (x → a, y → b, z → c) is applied as well. From the reports by Mihailova, et al. [56] and García-Flores, et al. [57] it is learned that a A_g mode at frequency ≈ 700 cm^{-1} exists in all the RMn$_2$O$_5$ materials whose Raman phonons have been reported. Note as well that these reports do not resolve any IR phonons becoming Raman active at the FE phase transition. Therefore this high frequency A_g Raman phonon is the mode we observe that acquires IR activity in the FE phase. Further experimental confirmation has been obtained [60] in the Raman spectrum of TbMn$_2$O$_5$ that clearly identifies the high frequency Mn-O Raman phonon with this newly activated IR phonon reported here.

Only a few other phonons show correlations with the low temperature phase transitions. The phonons polarized along the a axis do not show any significant anomalies in this temperature range. This is consistent with the featureless behavior of the dielectric function along this axis. On the other hand, the behavior of some of the phonons with dipole moment along b is non-trivial. The low frequency phonon with frequency ≈ 96 cm^{-1}, identified primarily with movement of the Tb ions, has a temperature dependence that correlates with the low temperature CM → ICM magnetic transition. In figure 3.6 the frequency of this phonon is plotted versus temperature and an increase in the fre-

observation and analysis would not change.

Table 3.2: Irreducible representation splitting at the FE phase transition. S. A. = Spectral Activity (R = Raman active, IR = Infrared Active).

# 55 S. A.	$Pbam$ irreps	$Pb2_1m$ irreps	$Pb2_1m$ S. A.[a]
R	A_g	A_1	IR (y) & R
R	B_{1g}	B_2	IR (x) & R
R	B_{2g}	A_2	R
R	B_{3g}	B_1	IR (z) & R
Silent	A_u	A_2	R
IR(z)	B_{1u}	B_1	IR (z) & R
IR(y)	B_{2u}	A_1	IR (y) & R
IR(x)	B_{3u}	B_2	IR (x) & R

[a]Note that in this column x, y, z correspond to the high temperature system of coordinates *a, b, c* and differ from what is found in the character table.

quency around 24 K is observed. This effect is thought to be a manifestation of the coupling of this phonon to a magnon as is discussed by Katsura, et al [32].
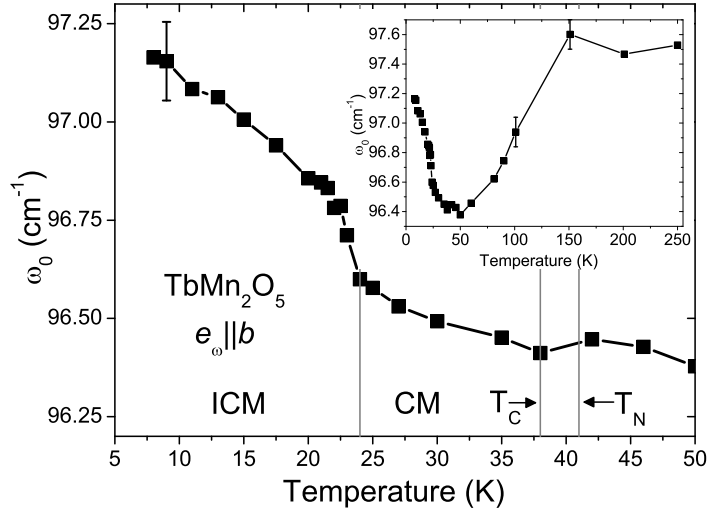
Figure 3.6: Temperature dependence of the b axis Tb phonon frequency. Inset shows the full temperature dependence. Typical dispersion of several measurements is indicated as error bars.

Surprisingly several phonons show interesting temperature dependence for T above T_N. The inset in figure 3.6 shows the full temperature dependence of the frequency of the b axis phonon. The anomalous softening in the temperature range of 150 K to 50 K demonstrates additional effects in the dynamics of the lattice. In figure 3.7 the behavior of the spectral weight of two oxygen phonons polarized in the a and b axes, with frequencies of 704 and 689 cm^{-1} respectively, seems complementary: the a phonon gains spectral weight while the b phonon looses it as the temperature is lowered. This

effect is present in the full temperature range from 300 K to 7 K, while for the rest of the phonons the spectral weight is only changed significantly around the various transition temperatures. The fact that these modes gain or lose so much spectral weight (10 and 6-fold respectively) in a large temperature interval also demonstrates some higher energy scale in this system. These effects (the anomalous softening and the dramatic changes in spectral weight) are not understood at present. However, one interesting possibility is that they are of magnetic character. Recent high temperature susceptibility measurements [57] in $BiMn_2O_5$ have shown evidence for spin frustrated behavior from deviations from Curie law with a Weiss temperature of $\approx$ 250 K. Dielectric anomalies in $BiMn_2O_5$ around this temperature have been reported [61] as well.

Finally the inset of figure 3.7 shows the temperature dependence of the intensity of a feature observed at 120 cm^{-1}. This is identified as a crystal field level of the Tb^{3+} ion [62]. This transition has electric dipole character as is seen from the form of the reflectivity curve (see fig. 3.3) as well as the fact that the spectral weight (see table 3.1) is comparable to the IR active phonons (magnetic dipole transitions are usually much weaker than electric dipole transitions). This conclusion is supported as well by the shell model calculation that shows the 3 lowest phonon excitations being the Tb-dominated phonon (at $\approx$ 100 cm^{-1}) and then a doublet (at $\approx$ 170 cm^{-1}). Furthermore, the observed temperature dependence of the intensity is common for the f-level crystal field transitions in the rare earth ions [63].
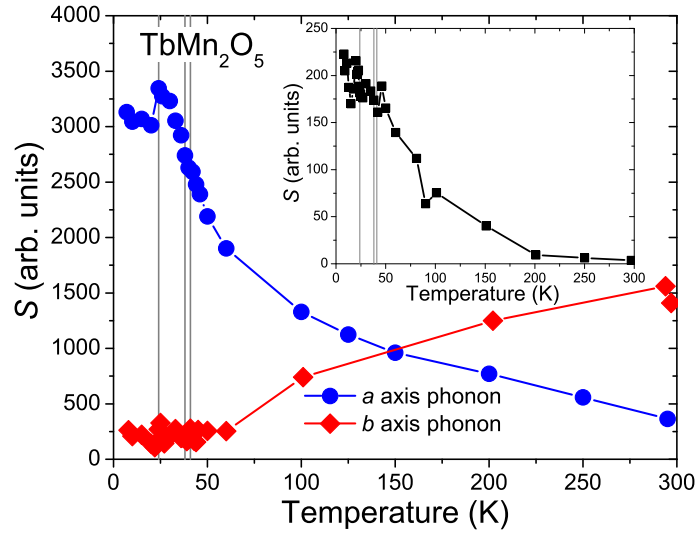
Figure 3.7: Temperature dependence of the spectral weight of 2 oxygen dominated phonons. Inset shows the temperature dependence of the spectral weight of one of the Tb^{3+} crystal field transitions.

3.4 Conclusions

The IR phonon spectra in $TbMn_2O_5$ have been measured along the *a* and *b* axes and most of the symmetry allowed modes were observed. The majority of the phonons do not show significant correlations to the FE and AFM phase transitions of the system. However several phonons exhibit interesting correlations to the ferroelectricity of this material. A signature of the loss of inversion symmetry in the FE phase by the appearance of a IR phonon below T_c that was only Raman active in the paraelectric phase was found. The strength of this mode is proportional to the square of the FE order parameter

and gives a sensitive measure of the symmetry lowering lattice distortions in the ferro-electric phase. In addition, the lowest frequency phonon (along b) displays hardening in the CM $\rightarrow$ ICM transition possibly due to the coupling with the spin system [32]; 2 modes (along a and b) have dramatic changes in their spectral weight over a wide temperature range possibly because of frustration effects in the spin system. It has also been identified in the spectra an electric dipole active crystal field transition of the Tb^{3+} ion in the phonon frequency range.

In addition, it is clear from these data that there is no soft phonon at the ferroelectric transition, even though the symmetry change of the lattice was found. This suggests that the anomalies in ε (see figure 3.2) at the different magnetic transitions are not caused by the infrared phonons, but additional electric dipole excitations must exist at lower frequencies. This is the topic of the next chapter.

Chapter 4

Electromagnons in the Multiferroic Family RMn$_2$O$_5$

The results of the investigation of the low energy electrodynamics below the IR phonons in the family of multiferroics RMn$_2$O$_5$ are presented. In this chapter the focus is on the discovery and properties of electromagnons.

4.1   Introduction

The magnetoelectric interactions that induce electric polarization in magnets can also couple oscillations of magnetization to polar lattice vibrations. The oscillations of polarization at magnon frequency and vice versa give rise to dynamic magnetoelectric effects, such as electromagnon excitations. In usual magnets, an oscillating electric field of photons can excite a three-particle continuum consisting of two magnons and one phonon [64]. This process results from the fourth-order spin-lattice coupling. The third-order couplings in multiferroics, discussed above, make possible photo-excitation of two-magnon continuum without a phonon ('charged magnons' [65]). Replacing one of the magnons by the static modulation of spin density appearing in the ordered spin state, a process that converts a photon into a single magnon results, which is the electromagnon. This process is usually mediated by a polar phonon linearly coupled to both magnons and light, which for low-frequency phonons can lead to a resonant enhance-

ment of the photo-excitation of electromagnons.

As there are two possible contributions to the polarization — from ionic displacements and from electronic density redistribution — one can think of two corresponding electric contributions to electromagnon — from phonons and from electronic excitations. This means a transfer of the electric dipole spectral weight from phonons ($\hbar\omega \sim 10 - 100$ meV) and/or electronic excitations ($\hbar\omega \sim 2$ eV) down to magnons ($\hbar\omega \sim 1 - 5$ meV). Such a transfer, in turn, leads to a step-like anomaly in the temperature dependence of the dielectric constant. Current research on electromagnons is focused mainly on magnon-phonon coupling while the magnon-electron aspect is much less explored as it is generally expected to be weak because of the large difference between the electronic and magnetic excitation frequencies

The outstanding fundamental questions for electromagnon are the microscopic origin of these novel excitations (Heisenberg or Dzyaloshinskii-Moriya type exchange) in the different classes of compounds (RMnO$_3$ and RMn$_2$O$_5$), the explanation of the observed selection rules, and whether electromagnons may occur in a wider range of materials. The practical issues are enhancing the magneto-capacitance effect and its temperature range and possibly applying these new excitations to metamaterials and/or achieving negative index of refraction in the magnon range of frequencies.

4.2   Experimental Results

In this Chapter, the observations of electromagnons in the RMn_2O_5 (R = Y, Tb, Eu) multiferroics are reported and compared with previously reported electromagnons [66] as well as with 'usual' magnons in multiferroic $LuMnO_3$. The measurements on YMn_2O_5 eliminate any confusion, coming from the spin excitations in the rare earth ions. The polarization of the electromagnons can be additional evidence in favor of the symmetric exchange as the leading magnetoelectric coupling mechanism.

Single crystals of YMn_2O_5 and $TbMn_2O_5$ were grown as described before [67]. The samples were characterized by X-rays and dielectric measurements in kHz range. Transmission measurements were performed using a Fourier-transform spectrometer in the frequency range from 4 to 200 cm^{-1}. The temperature dependence from 5 to 300 K was measured using liquid helium in a continuous flow cryostat (sample in vacuum) with optical access windows. A ^{3}He-cooled bolometer was used for low frequency measurements. To increase the accuracy of transmission measurements, thicker samples were used for weak features and thin samples for strongest modes: 0.46 and 0.09 mm for YMn_2O_5, and 0.725 and 0.16 mm for $TbMn_2O_5$.

The three phases in $TbMn_2O_5$ (YMn_2O_5) are addressed: LT1, incommensurate magnetic and ferroelectric, below 24(20) K; LT2, commensurate magnetic and ferroelectric, at $24(20) < T < 38(41)$ K; and the paramagnetic-paraelectric phase at $T > 41(45)$ K. The low frequency transmission spectra of $TbMn_2O_5$ in three phases are shown in Fig. 1. The lowest phonon was found to be centered at 97 cm^{-1} and is seen as zero transmis-
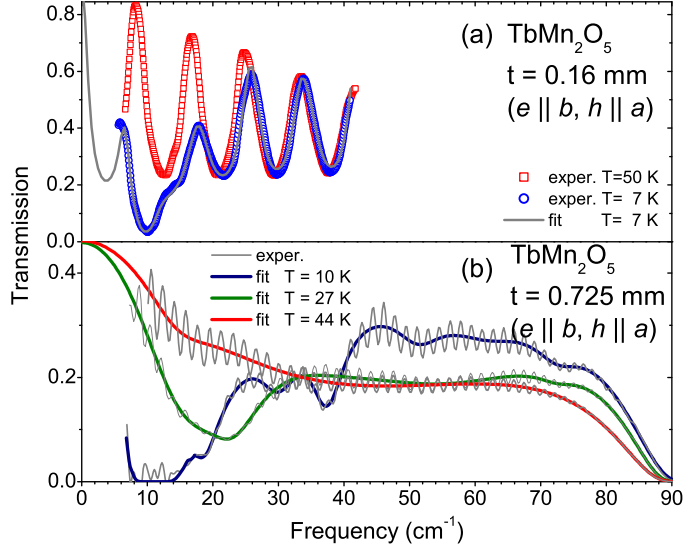
Figure 4.1: Transmission spectra of TbMn$_2$O$_5$: (a) thin sample, (b) thicker sample, oscillations are averaged out in model curves. Oscillations of experimental data are due to the etalon effect. e and h are electric and magnetic fields of light.

sion in figure 4.1b consistent with the phonon frequency in Table 3.1. All other features below this frequency are of magnetic origin (but with electric dipole activity). Figure 4.1a shows results for the strongest absorption (low transmission) near 10 cm^{-1} in the LT1 phase in comparison to the paramagnetic phase. Figure 4.1b emphasizes weak absorption features.

Identifying these excitations as electromagnons requires addressing several questions. To avoid confusion with possible transitions between f-levels of rare earth ions, YMn$_2$O$_5$ was selected as Y has empty f-shells. A second issue is electric or magnetic

dipole activity. Figure 4.2 presents transmission spectra of YMn_2O_5 for the three phases defined above. From fig 4.2a it follows that the absorption bands are either $e||b$ or $h||a$ active. In the spectra in figure 4.2b, measured for $h||a$ on a different cut of a crystal, there is no comparable absorptions. Spectra, taken in $(e||a, h||b)$ configuration, are similar to those in figure 4.2b — without absorptions. It follows that strong absorptions occur only in $e||b||$P orientation and are, therefore, electric dipole active. There is a possibility of observation of the magnetic activity in this frequency range however, the electric dipole part is of stronger interest. Based on the shell model calculations of the phonon frequencies, the lowest phonon frequency is near 100 cm^{-1}. Therefore, these new modes cannot be new phonons activated in the low T phases.

To extract the parameters of the oscillators, the transmission spectra is fitted with a Lorentzian model of the dielectric constant $\varepsilon(\omega)$ for electric dipole or magnetic permeability $\mu(\omega)$ for magnetic dipole transitions:

$$\varepsilon(\omega) = \varepsilon_\infty + \sum_j \frac{S_j}{\omega_j^2 - \omega^2 - \iota\omega\gamma_j} \tag{4.1}$$

$$\mu(\omega) = 1 + \sum_j \frac{S_j}{\omega_j^2 - \omega^2 - \iota\omega\gamma_j} \tag{4.2}$$

where ε_∞ is the high frequency dielectric constant, j enumerates the oscillators, S_j is the spectral weight, ω_j is the resonance frequency, and γ_j is the damping rate. The extinction coefficient is proportional to $\sqrt{\varepsilon(\omega)\mu(\omega)}$. Thus, electric and magnetic dipole absorptions can be compared using same set of the oscillator parameters. These param-

66
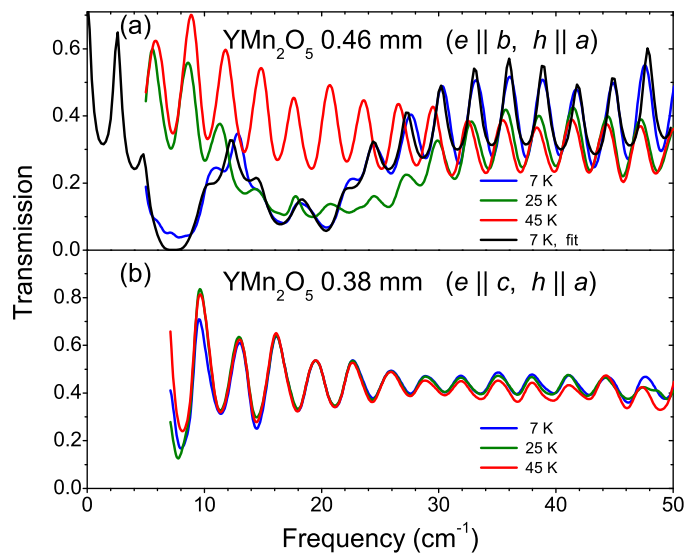
Figure 4.2: Transmission spectra of multiferroic YMn_2O_5: Absorption is observed only when $e||b$ and is, thus, electric dipole active. Nonzero transmission near 7 cm^{-1} at 7 K in panel (a) and difference between curves in (b) is due to a low frequency noise.
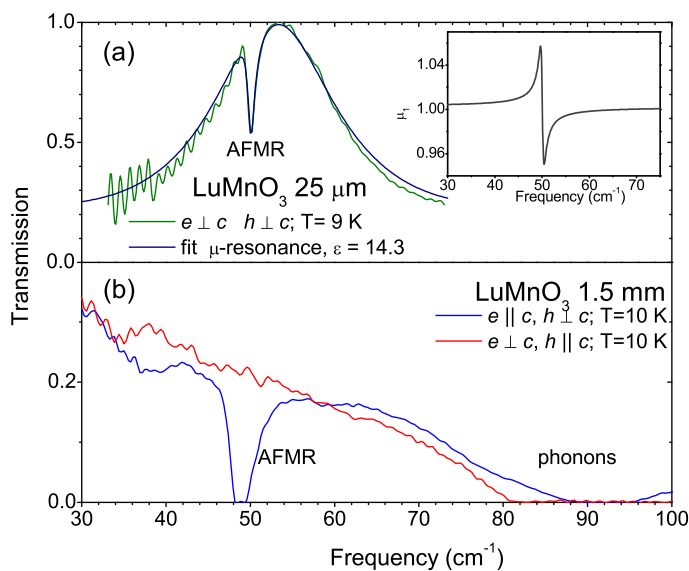
Figure 4.3: Transmission spectra of hexagonal multiferroic LuMnO$_3$: Absorption is observed only when $h \perp c$ and is magnetic dipole active. (a) Transmission for a thin sample, (b) for thick single crystal.

eters are collected in the Table 4.1. Here, spectra of Y- and TbMn$_2$O$_5$ were fitted with formula 4.1 at fixed $\mu = 1$; and for LuMnO$_3$ equation 4.2 was used at fixed $\varepsilon = 14.3$ as shown in figure 4.3.

It is interesting to compare the observed electromagnons to the uncoupled magnons in multiferroic hexagonal LuMnO$_3$. This compound is ferroelectric below $\sim$1000 K and antiferromagnetic below 76 K with geometric frustration. Using different cuts of the LuMnO$_3$ crystal, one resonant absorption is observed only in the $h(\omega) \perp c$ configuration. It means that this mode is magnetic dipole active (parameters are in Table 4.1).

68

Table 4.1: Comparison of spectral parameters of electromagnons/magnons in various multiferroics.

Compound	ω_0 (cm^{-1})	S (cm^{-2})	γ (cm^{-1})
YMn$_2$O$_5$	7.2	170	1.9
TbMn$_2$O$_5$	9.6	330	3.6
TbMnO$_3$ [66] [a]	23	≈1000	>25
LuMnO$_3$	50	4	0.75

[a]See Chapter 5

The dielectric constant shows a gradual 'step-down' anomaly below 76 K, caused by phonon hardening [68]. Therefore, despite sharing with RMn$_2$O$_5$ the features of multiferroicity, frustrated magnetism, and non-collinear spin order, hexagonal LuMnO$_3$ does not have detectable electromagnon excitations. Hexagonal HoMnO$_3$ has several absorption bands below 100 cm^{-1} which confirms the possible effects of rare earth ions.

Figure 4.4 shows the optical conductivity of YMn$_2$O$_5$ and TbMn$_2$O$_5$ along the ferroelectric b-axis in three different phases as determined from the fits to the transmission spectra. In the ground state, LT1, both compounds show strong electromagnons at low frequencies and a several weaker peaks at higher frequencies. In the RMn$_2$O$_5$ structure 16 magnon branches are expected [13], and only the strongest electromagnons are seen in Figure 4.4. In the LT2 phase only a broad mode, centered at 20 cm^{-1}, is present. This mode in Y has S=225 cm^{-2} and contributes 0.6 to the static ε. At 45 K, just above the
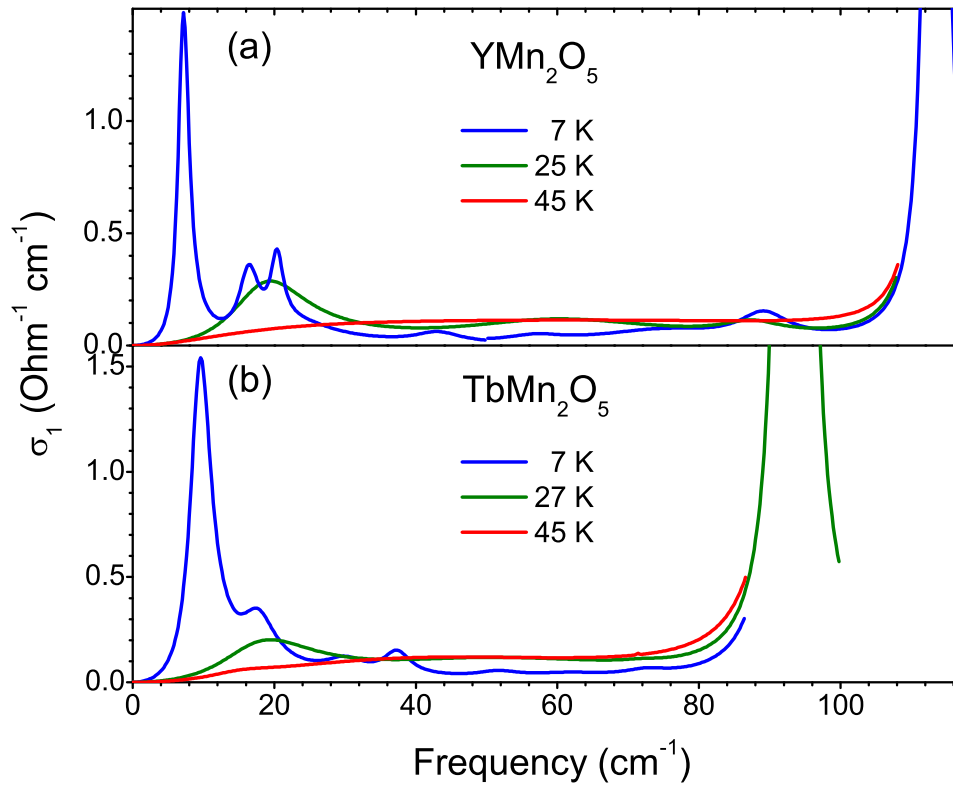
Figure 4.4: Optical conductivity of YMn$_2$O$_5$ and TbMn$_2$O$_5$ for $e||b$ in three phases. Strong peaks at 113 and 97 cm^{-1} are the lowest phonons. Other peaks are electro-magnons.

Neel temperature, no well defined modes are observed. However, there is a broad background absorption which extends at least up to the lowest TO phonon frequency. This absorption is present at all three temperatures and it is really gone only at room temperature. This broad absorption can be understood as frustrated spin fluctuations with electric dipole activity. The similar behavior of both compounds points to a leading role of Mn spin system in the physics of all of these electromagnon excitations.

Transmission of a $EuMn_2O_5$ polycrystal was measured as well. Its absorption spectrum is similar to those shown in Figure 4.4: a strong peak at $14\ cm^{-1}$ in the LT1 phase and a broad peak at $20\ cm^{-1}$ in the LT2 phase. Therefore $EuMn_2O_5$ is another RMn_2O_5 compound with nonmagnetic rare earth ion that supports electromagnon excitations.

The data of Table 4.1 allow to compare the electromagnons in $RMnO_3$ and RMn_2O_5 compounds. The resonance frequencies of the strongest electromagnons in the RMn_2O_5 compounds are lower than those in $TbMnO_3$ suggesting a possible stronger mode 'repulsion'. However this is inconsistent with their weaker oscillator strength. Therefore, the different frequencies may be due to the distinct magnetic anisotropies, which influence the bare magnon frequencies. Electromagnon spectrum of the RMn_2O_5 compounds is better resolved into distinct modes than the $RMnO_3$ spectrum. However, the total spectral weight of $510\ cm^{-2}$ of all $TbMn_2O_5$ modes, seen below the lowest phonon in LT1 phase, is closer to $\approx 1000\ cm^{-2}$ of the $TbMnO_3$ electromagnon. It would be interesting to compare infrared data to inelastic neutron scattering results to match electric and magnetic dipole activity in this frequency range for these two types of multiferroics.

The polarization of electromagnons gives additional information about leading spin-lattice coupling mechanism. Katsura et al. [32] showed that for DM type coupling and cycloidal spin chain the electromagnon is electrically active along the axis perpendicular both to the Q-vector of spin structure and static polarization **P**. These imply that the DM exchange is not the leading magnetoelectric coupling in the RMn$_2$O$_5$ compounds where the electromagnon is active for e||P. On the other hand, the latter polarization can be obtained from Heisenberg exchange and magnetostriction, as shown below [13]. Therefore, the results presented here give additional evidence in favor of symmetric exchange being dominant in RMn$_2$O$_5$ compounds suggested earlier [18, 49].

It is important to know where the electromagnons obtain their electric activity. Simple model calculations emphasize the role of the lowest phonon [32]. This prediction was qualitatively confirmed for GdMnO$_3$ by Pimenov et al. [69] but the change in the phonon spectral weight (60 %) was too large. On examining the phonon spectra of TbMn$_2$O$_5$ in Chapter 3 [67], clear correlations could not be found with activation of electromagnons. The lowest phonon with $S \approx 5000$ cm^{-2} is observed to strengthen slightly in the LT1 phase in contradiction to expectation from mode mixing. However, its frequency hardens in the LT phases (see figure 3.6 and [67]) in accord with the electromagnon models. Determining which phonons couple to the magnon and with what strength remains an important experimental challenge.

Figure 4.5 shows the temperature dependence of the static dielectric constant from kHz range measurements (top curve) compared with the dependence obtained from the
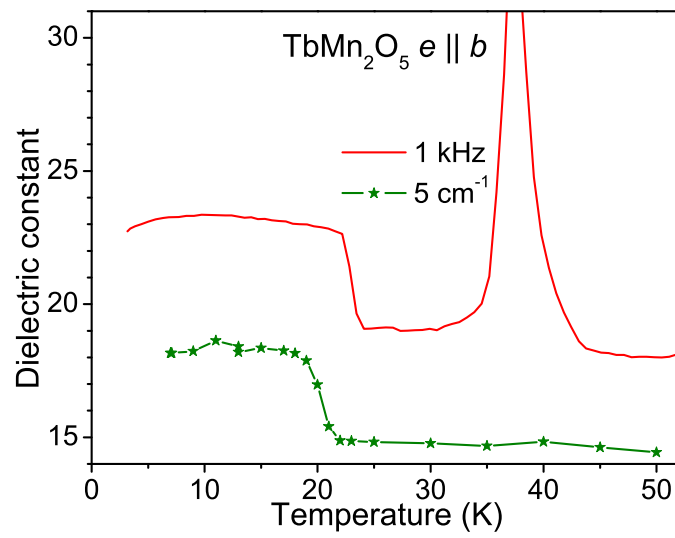
Figure 4.5: Dielectric constant of TbMn$_2$O$_5$ from fits of infrared spectra (lower curve) in comparison with kHz measurements.

fits of the far infrared spectra of $TbMn_2O_5$. Only the Tb compound data are shown because of the larger sample size and higher frequency of the strongest electromagnon. These data show that the whole step-like anomaly in $\varepsilon(T)$ results from electromagnons. It follows that we observe practically all electromagnons. The largest contribution to ε in the LT1 phase comes from the strong low frequency electromagnon. The difference in absolute values of ε comes possibly from the zero-frequency relaxational mode that is yet to be observed. The sharp peak at 38 K (top curve), at the onset of **P**, is also produced by this mode, and it is not observed in the far infrared (lower curve). The magnetic nature of electromagnons allows suppression/enhancement and/or Zeeman splitting of original magnon branches by externally applied magnetic fields [66, 70] which leads to the magneto-dielectric effects [71].

Finally, a definitive confirmation of these excitations as electromagnons can come via their observation in magnetic neutron scattering. A set of measurements has been performed by Prof. Seung-Hun Lee [72] on a single crystal of YMn_2O_5 and the results are shown in figure 4.6. Comparing this spectrum with figure 4.4(a), we can see that the magnetic scattering features match almost perfectly to the absorption peaks observed in the far infrared, confirming that these are in fact magnons.

In conclusion, the observation of electromagnons was reported in the RMn_2O_5 compounds including the non rare earth YMn_2O_5. The spectra of YMn_2O_5 and $TbMn_2O_5$ are very similar which proves the Mn origin of electromagnons in these compounds. The overall spectral weight of RMn_2O_5 electromagnons is approximately 1/2 that in
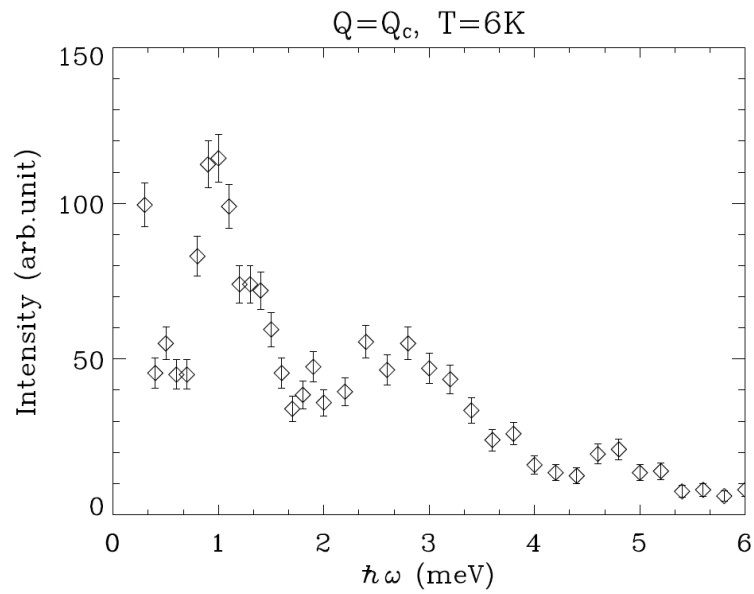
Figure 4.6: Inelastic neutron scattering intensity as a function of energy transfer at the wave vector of the magnetic structure $Q_c = \left(\frac{1}{2}, 0, \frac{1}{4}\right)$). Figure courtesy of Prof. Seung-Hun Lee.

RMnO$_3$ compounds [66]. The electromagnons polarization selection rules in RMn$_2$O$_5$ provides evidence in favor of symmetric exchange coupling mechanism in this system. The match between the optical and neutron scattering experiments confirms again the hybrid nature of these excitations.

4.3   Exchange Striction Model

The presence of two different types of magnetic ions and geometric frustration of spin interactions give rise to rather complex magnetic structures RMn$_2$O$_5$ compounds. Nonetheless, a number of salient properties of these materials, such as the magnetically-induced electric polarization, photo-excitation of magnons as well as the spin re-orientation transition, can be understood within a simplified microscopic model, which is discussed in this section. The starting point is the assumption that multiferroic and optical properties of these materials are governed by the symmetric Heisenberg exchange, although magnetic anisotropy is included to explain the spin re-orientation transition that has a strong effect on the low-frequency absorption spectrum. This model predicts the ordered spin states, the mechanism of magnetoelectric coupling and enables the calculation of the optical absorption spectrum at magnon frequencies for different magnetic states.

First, consider a single magnetic ab-layer including Mn^{3+} and Mn^{4+} ions. The model describes interactions between the spins and their coupling to a polar phonon

mode:

$$\mathscr{H} = \frac{1}{2}\sum_{i,j} J_{ij}(\mathbf{P})\left(S_i \cdot S_j\right) - \frac{1}{2}\sum_{i\alpha} K_{i\alpha}\left(S_i \cdot \hat{k}_{i\alpha}\right)^2 -$$
$$- \sum_i \mu_i \left(S_i \cdot H\right) + V\left(\frac{P^2}{2\chi_1^{(0)}} - PE - \frac{\chi_2 E^2}{2}\right). \tag{4.3}$$

Here the first term is the symmetric Heisenberg spin exchange, while the second term is the single-ion anisotropy. The antisymmetric Dzyaloshinskii-Moriya exchange as well as other types of anisotropic exchange interactions are not included, as in the scenario discussed below they play no role. For simplicity it is assumed that in the ordered state all spins lie in the *ab* plane [49] and neglect the small out-of-plane components found in recent neutron diffraction experiments on single crystals [73, 74]. Thus, the easy and intermediate magnetic axes on each Mn site ($\alpha = 1, 2$) lie in the *ab* plane, while the hard axis $\hat{k}_{i3} \parallel \hat{c}$. The third term in (4.3) is the interaction of spins with an applied magnetic field and the last term describes the dielectric response of the system, where $\chi_1^{(0)}$ is the 'bare' dielectric susceptibility related to the polar lattice mode (not including the magnetic contribution calculated below) and χ_2 is the remaining part of the dielectric susceptibility of non-magnetic origin. Finally, V is the system volume.

The coupling between the spins and the polar phonon mode results from the dependence of the exchange coupling on the electric polarization, which in $R\mathrm{Mn_2O_5}$ is parallel to the *b* axis:

$$J_{ij}(P_b) = J_{ij}(0) + J'_{ij}(0)P_b + \frac{1}{2}J''_{ij}(0)P_b^2 + \dots \tag{4.4}$$

The last two terms give rise to the cubic and the quartic magneto-electric couplings.

4.3.1 Magnetic ordering and spin re-orientation transition

Here, the model of Chapon *et al.* [49] is used with 5 exchange constants between pairs of nearest-neighbour Mn ions: J_1 and J_2 couple Mn^{4+} ions along the c direction, J_3 and J_5 couple the spins of neighboring Mn^{3+} and Mn^{4+} ions and J_4 is the coupling between two neighboring Mn^{3+} ions (see figure 4.7).
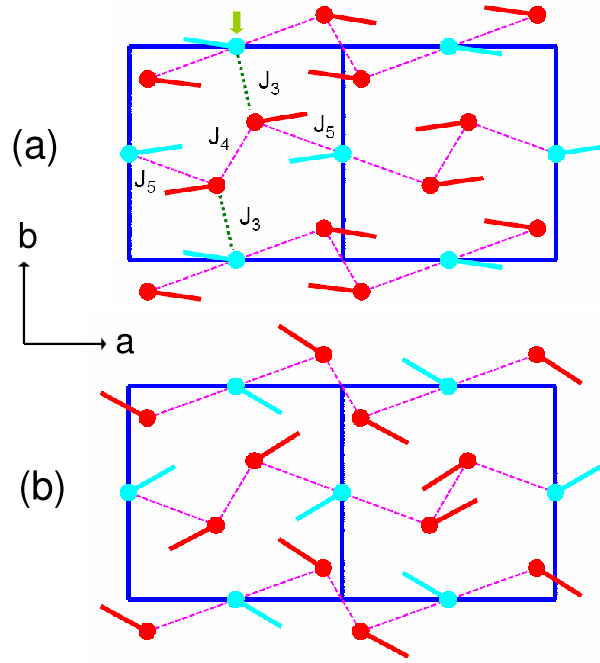
Figure 4.7: Minimal energy spin configurations for $J_4 = J_5 = 40$ K and the anisotropy parameter $K_a(Mn^{3+}) = 0.6$ K for all Mn^{3+} ions (red) and $K_a(Mn^{4+}) = 0.1$ K for all Mn^{4+} ions (blue). The value of the interchain coupling J_3 is -2 K for the structure in panel (a) and -4 K for the one panel (b).

Figure 4.7 shows the minimal energy spin configurations obtained by the numerical minimization of the spin energy (4.3) on the subspace of the commensurate magnetic

states with the wave vector $Q = (1/2, 0, 0)$ for two different sets of exchange constants. The exchange constants J_4 and J_5 were chosen to be positive and large compared to other exchange constants, which gives rise to antiferromagnetic zig-zag chains along the a axis with nearly collinear spins (marked by dashed lines) observed in neutron experiments [49, 74].

The angle between spins in neighboring chains sensitively depends on the ratio between the interchain coupling J_3 and the magnetic anisotropy parameters K_i. The easy magnetic axis is parallel to the a axis. The interplay between magnetic anisotropy and interchain interaction determines the angle between spins in neighboring antiferromagnetic chains.

First note that if spins in each antiferromagnetic chain would be perfectly collinear, then the interchain interactions would cancel as a result of geometric frustration. Conversely, the interchain coupling J_3 results in spin rotations, which destroy the collinearity of spins in each chain. Consider, for example, the spin of the Mn^{4+} ion, marked in figure 4.7(a) by an arrow. Because of a nonzero angle between spins in the neighboring a-chains, the interaction of the marked spin with the spin of the Mn^{3+} ion from the neighboring chain will give rise to a rotation of the marked spin. These small spin rotations lift the frustration and lead to some energy gain due to interchain interactions. Thus, while the magnetic anisotropy favors an almost collinear spin configuration, interchain interactions favor the $90°$ angle between spins of neighboring chains.

This competition gives rise to a very strong sensitivity of the angle between spins

in neighboring chains to the interchain coupling J_3. For weak interchain coupling $J_3 = -2$ K, this angle is relatively small and minimal-energy spin configuration shown in figure 4.7(a) is similar to the one observed in the high-temperature 'collinear' phase of YMn_2O_5 by Chapon *et al.*[49]. A small change in J_3 from -2 K to -4 K transforms the configuration shown in figure 4.7(a) into the one shown in figure 4.7(b), which may explain the spin re-orientation observed in RMn_2O_5 with $R =$ Tb, Ho, Dy and Y, provided that the interchain coupling is temperature-dependent. Although the rotations that make spins in each chain non-collinear are barely visible, they are sufficient to produce the large changes in the spin configuration, since the magnetic anisotropy is relatively weak. In RMn_2O_5, the spin re-orientation transition is accompanied by the loss of commensurability of the spin structure in the a and c directions (which is also a consequence of magnetic frustration). This latter aspect of the transition is, however, less important for the photo-excitation of magnons, discussed below, than the re-orientation of spins.

4.3.2 Magnetically-induced polarization

Minimizing (4.3) with respect to P_b, we obtain expression for the magnetically-induced electric polarization,

$$P_b \approx -\frac{\chi_1^{(0)}}{2V} \sum_{i,j} J'_{ij}(0)\left(S_i S_j\right),\tag{4.5}$$

which only involves scalar products of spins (compare to equation 1.5).

Figures 4.8 and 4.9 show why in the high-temperature ferroelectric phase the polarization vector is oriented along the b axis. Figure 4.8 gives a simplified view of the
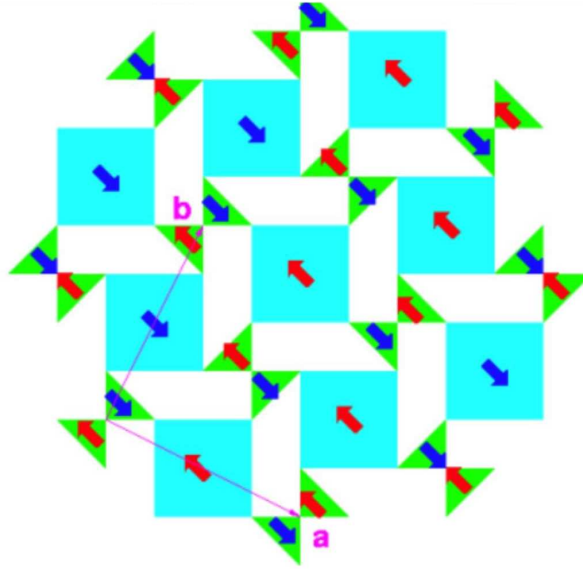
Figure 4.8: A cartoon of the magnetic ordering in the high-temperature collinear phase.

Mn layer in the *ab* plane, in which the spins inside squares depict the spins of Mn^{4+} ions located inside oxygen octahedra, while the spins inside triangles are the spins of Mn^{3+} ions in oxygen pyramids. The nearly collinear magnetic ordering in the high-temperature ferroelectric phase consists of antiferromagnetic chains with spins pointing along the *a* direction.

The mechanism responsible for electric polarization in this magnetic state involves, however, the ↑↑↓ and ↓↓↑ spin chains along the *b* axis, such as shown in figure 4.9. These chains contain the polar Mn^{4+} – Mn^{3+} bonds, connecting parallel spins, and the Mn^{3+} – Mn^{4+} bonds with opposite polarity, connecting antiparallel spins. Importantly, the charge and spin modulations in the chains have the same period, in which case the conventional exchange striction destroys the cancellation of electric dipoles of the polar
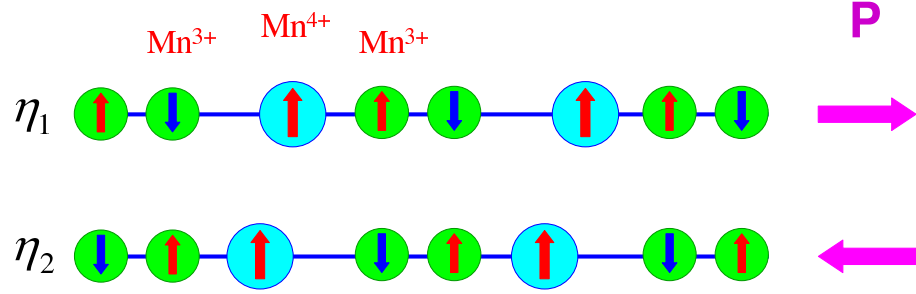
Figure 4.9: Electric polarization induced by magnetostriction along the b-chains. The two order parameters η_1 and η_2 describe degenerate ferroelectric states with opposite directions of electric polarization.

bonds and induces electric polarization along the chains, as illustrated in figure 4.9.

This mechanism also works in the low-temperature (incommensurate) ferroelectric phase, in which the spin and charge orders continue to have the same periodicity in the b-direction. The amplitude of the exchange striction is, however, largest for collinear spins [see (4.5)], which explains the drop of the polarization at the transition to the low-temperature phase. For example, if the value of the magnetoelectric coupling $\propto J_3' - J_4' - J_5'$, is chosen such that the electric polarization induced by the 'high-temperature' configuration shown in figure 4.7(a) is 1000 μC m^{-2}, then for the 'low-temperature' configuration shown in figure 4.7(b) it equals 500 μC m^{-2}.

4.3.3 Static and dynamic dielectric susceptibility

The contribution of the coupled spin-lattice degrees of freedom to static dielectric susceptibility is given by

$$\chi_1^{-1} \approx \left(\chi_1^{(0)}\right)^{-1} - \frac{1}{V}\sum_{i,j} I_i A_{ij}^{-1} I_j + \frac{1}{2V}\sum_{i,j} J_{ij}''(0)\left(S_i S_j\right), \tag{4.6}$$

where

$$A_{ij} = J_{ij}\left(S_i S_j\right) + \delta_{ij}\left[\sum_{\alpha=1,2} K_{i\alpha}\left(2\left(S_i \hat{k}_{i\alpha}\right)^2 - S_i^2\right) - \sum_k J_{ik}\left(S_i S_k\right)\right] \tag{4.7}$$

and

$$I_i = \sum_j J_{ij}'\left[S_i \times S_j\right]_c, \tag{4.8}$$

The second term in (4.6) is the spin contribution to the dielectric constant due to virtual excitations of magnons by electric field (this will become more apparent in the discussion of the dynamic susceptibility).

The last term in (4.6) describes the shift of the phonon frequency due to a change of the spring constants in magnetically ordered states. This effect is known in condensed matter spectroscopy as spin-phonon coupling [75, 76]. Phenomenologically, this effect is described by the fourth-order magnetoelectric coupling of the type $P^2 L^2$, where L is a magnetic order parameter. In most cases, magnon and phonon branches coupled through this term experience 'repulsion' and phonon hardens. However, in the magnetically frustrated compounds, this contribution to the dielectric constant can have either sign and can result in either hardening or softening of phonons in the magnetic phase (see, e. g., [77] on $CdCr_2S_4$ spinel).

Equations of motion describing the coupled spin-lattice dynamics have the form,

$$\ddot{P}_b = -\frac{\chi_0 \omega_0^2}{V} \frac{\partial \mathscr{H}}{\partial P_b},$$

(4.9)

$$\dot{S}_i = \left[\frac{\partial H}{\partial S_i} \times S_i \right],$$

where $\chi_0 = \chi_1^{(0)} + \chi_2$ and ω_0 is the bare frequency of the polar phonon. Omitting the fourth order coupling term and solving linearized equations of motion, the dynamic dielectric susceptibility is:

$$\chi^{-1}(\omega) \approx \chi_0^{-1}\left(1 - \frac{\omega^2}{\omega_0^2}\right) - \frac{1}{V}\sum_{i,j} I_i \left[(BA - \omega^2)^{-1} B \right]_{ij} I_j,$$

(4.10)

where

$$B_{ij} = J_{ij} + \frac{\delta_{ij}}{S_i^2} \sum_{\alpha=1,2} \left(K_{i\alpha} \left(S_i \hat{k}_{i\alpha} \right)^2 - K_{i3} S_i^2 \right) - \frac{\delta_{ij}}{S_i^2} \sum_k J_{ik} (S_i S_k).$$

(4.11)

The second term in (4.10) describes the transfer of a part of electric dipole spectral weight from phonon to magnon frequencies, which turns magnons coupled to phonons into electromagnons. If such an electromagnon has lower frequency than the phonon, the static dielectric constant $\varepsilon(0) = 1 + 4\pi\chi(0)$ increases as a result of the coupling showing a step-like anomaly. Furthermore, frequencies of the mixed spin-lattice excitations (poles of the dielectric susceptibility (4.10)) are shifted down with respect to the 'bare' magnon frequencies, found from

$$\det \left(BA - \omega^2 \right) = 0.$$

(4.12)

Note that the electromagnon term in (4.10) disappears for collinear spin states, as I_i, defined by (4.8), is zero in this case. This can be understood as follows. Classically,
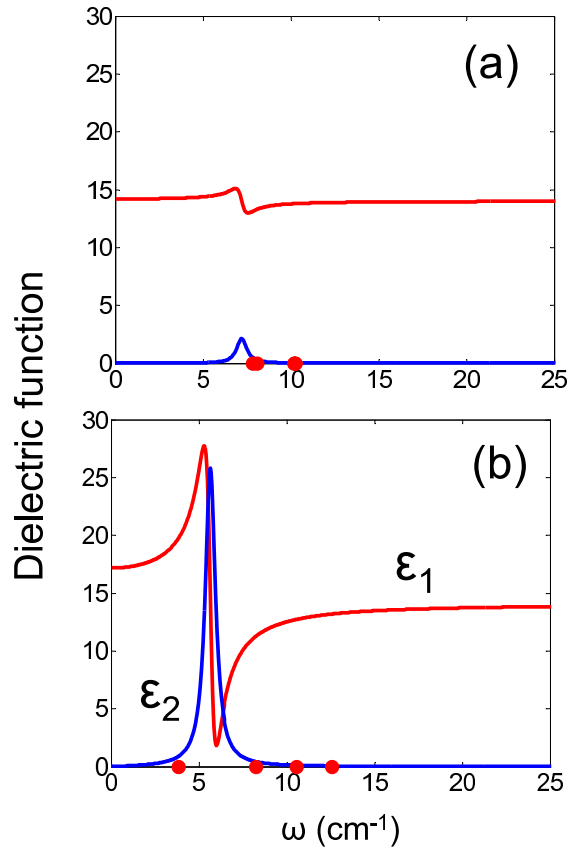
Figure 4.10: The model calculation results: Frequency dependence of the real (ε_1) and imaginary (ε_2) parts of the dielectric function (red and blue lines, respectively) for the 'high-temperature' collinear state (panel a) and the 'low-temperature' non-collinear state (panel b) shown, respectively, in panels (a) and (b) of figure 4.7. Red points are selected magnon frequencies of spins decoupled from the lattice found as the roots of (4.12). A magnon at 11.8 cm^{-1} couples to a polar phonon at 100 cm^{-1} and becomes an electromagnon observable as the peak of the ε_2.

magnons correspond to spin oscillations that are orthogonal to ordered spin vectors. The change of the scalar product of a pair of collinear spins is then proportional to the second power of the amplitude of the oscillations. Since the magnetoelectric coupling in the model originates solely from Heisenberg exchange and only involves scalar products of spins, the linear coupling of electric field to magnons is absent for collinear spins and the lowest-order process is the photo-excitation of a pair of magnons.

In figures 4.10(a) and (b), the real and imaginary parts of the dielectric function (red and blue lines, respectively) are plotted for the 'high-temperature' and 'low-temperature' states shown in, respectively, figures 4.7(a) and (b) (the imaginary part was obtained by the shift $\omega \rightarrow \omega + i\frac{\gamma}{2}$ with $\gamma = 1$ K). As was explained above, the coupling of magnons to the electric component of light and significant electric dipole absorption at magnon frequencies is only present in the non-collinear 'low-temperature' phase, in agreement with experiment. This result may seem somewhat counterintuitive: while the spontaneous electric polarization induced by the Heisenberg exchange striction is maximum for the collinear state, the excitation of magnons by the electric component of light (electromagnons) requires non-collinear spins and is only observed below the spin reorientation transition.

For comparison the transmission spectrum of $BiMn_2O_5$ is plotted in figure 4.11. The temperature dependence shows that only two weak absorption peaks activate below the ferroelectric transition temperature 40 K. Therefore, this clearly shows that in the purely collinear phase of RMn_2O_5 only ferroelectric polarization is allowed but
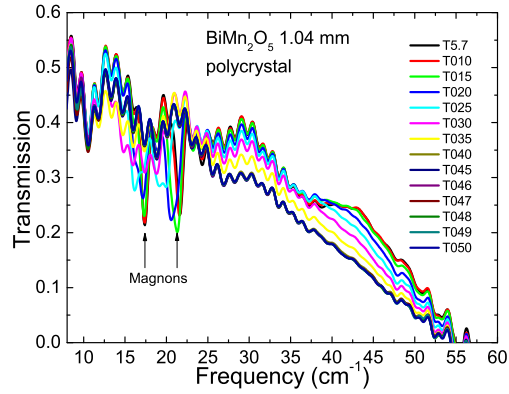
Figure 4.11: Transmission spectra in $BiMn_2O_5$. Only weak magnetic dipole magnons are observed in the spectra below the ferroelectric ordering temperature.

electromagnons are not.

The red points in figure 4.10 mark the bare frequencies of the softest magnons with zero wave vector, found from (4.12). Since the magnetic unit cell in this calculation contains 16 mangetic ions, the total number of such magnons is also 16. However, only one of them is strongly coupled to the electric component of light and significantly contributes to the dielectric constant. This electromagnon corresponds to relative rotation of spins of the neighboring antiferromagnetic chains, which gives rise to oscillations of the induced electric polarization in the b direction. The frequency of this uncoupled magnon for the non-collinear spin configuration shown in figure 4.7(b) is $11.8 \, \mathrm{cm}^{-1}$. As the position of the absorption peak in figure 4.10(b) is clearly lower that this magnon frequency, these parameters correspond to the strong magnetoelectric coupling case. The strong coupling is apparently necessary, if the large difference between dielectric con-

stants of the 'high'- and 'low'-temperature phases $\Delta\varepsilon'(0)$ (= 3.25 in our calculation) is associated solely with the absorption peak emerging in the non-collinear state.

The results of the model calculations presented in figure 4.10(b) show that the symmetry properties of one magnon and the lattice allow an electromagnon in this system. In this model, the first derivatives of the exchange integrals J_{ij} are the coupling constants. Both magnetically induced polarization and electromagnon were calculated using the same set of J' values. Characteristic value of J' used in our calculation was $dJ_3/dy =$ 4 meV/Å which is much less than, for example, 40 meV/Å for $ZnCr_2O_4$ [78].

4.4 Conclusions

This chapter has presented data on multiferroic $TbMn_2O_5$ and YMn_2O_5 single crystals that very clearly confirm the existence of electromagnons in this family. The match between figures 4.4(a) and 4.6 unambiguously affirm these excitations as electromagnons. A model based on a magnetoelectric interaction of pure Heisenberg origin is capable of explaining the appearance of electric polarization and electromagnons and their selection rule.

This model makes two very fundamental predictions, which are that electromagnons can appear even if the static polarization is zero, i.e. in magnetic materials that might not necessarily are multiferroic, and that they can only exist if the magnetic structure is non-collinear. These predictions will be useful for studies of other families of multiferroics.

Chapter 5

Electromagnons in the Multiferroic Family RMnO$_3$

5.1 Overview

In this chapter the electromagnon spectra of Eu$_{0.75}$Y$_{0.25}$MnO$_3$ and TbMnO$_3$ are presented in the context of the theoretical proposal based on the symmetric Heisenberg exchange coupling in spiral magnets RMnO$_3$.

Eu$_{0.75}$Y$_{0.25}$MnO$_3$ has a crystal structure belonging to the orthorhombic space group *Pbnm* which is sometimes called the distorted-perovskite structure shown in figure 5.1. In this structure, the Mn^{3+} ions are surrounded by a distorted octahedron of oxygens. This distortion is the Jahn-Teller distortion [79] because it originates from a degeneracy of the electronic orbitals in the Mn ion. In addition, the octahedra are rotated in a special pattern that reduces the overall symmetry from cubic to orthorhombic, this distortion is usually refereed as the GdFeO$_3$ distortion [80], which makes the Mn-O-Mn angle smaller than $180°$.

As introduced in Chapter 1, Eu$_{0.75}$Y$_{0.25}$MnO$_3$ belongs to the family of multiferroics that are spiral magnets. However, the spiral plane is not the same as in TbMnO$_3$ where the spins lie in the $b-c$ plane. In Eu$_{0.75}$Y$_{0.25}$MnO$_3$ the spiral is in the $a-b$ plane [12][1],

---

[1] The magnetic structure of Eu$_{0.75}$Y$_{0.25}$MnO$_3$ has not been found experimentally by neutron scattering yet, but the behavior of the magnetic susceptibility is used in [12] to argue that spins lie in the $a-b$ plane.
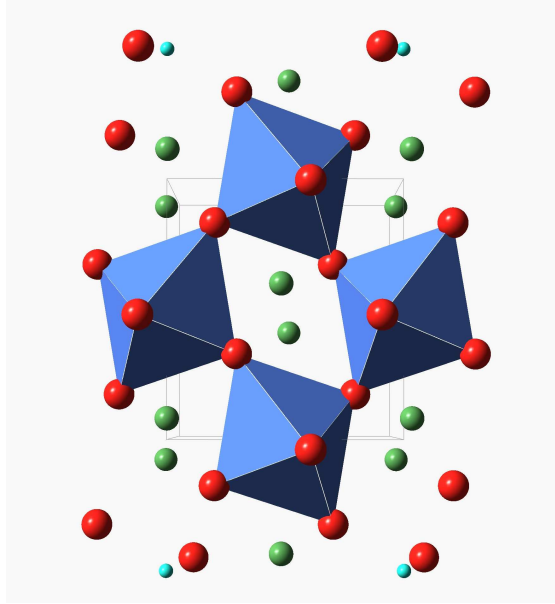
Figure 5.1: Structure of multiferroic RMnO$_3$.

making then the direction of the polarization along the a axis. This configuration is also found in TbMnO$_3$ when a magnetic field is applied in the a or b direction as well [1, 81].

5.2 Experimental Results Eu$_{0.75}$Y$_{0.25}$MnO$_3$

Single crystals of Eu$_{0.75}$Y$_{0.25}$MnO$_3$ were grown as described elsewhere [67]. The samples were characterized by X-ray diffraction and dielectric measurements in kHz range. These samples are ferroelectric below T_{FE}=30 K with static polarization in the $a-c$ plane ($\mathbf{P_a} > \mathbf{P_c}$), and magnetically ordered with transition temperature T_N=47 K, the magnetic structure is still unknown. Optical measurements of reflectance and transmission were made as a function of temperature as described in Chapter 2 [82]. The transmission of a $a-b$ plane crystal was measured at thicknesses of 1.93, 0.45, 0.080

and 0.020 mm. A second crystal was measured in $a - c$ plane geometry at 1.28 mm thickness.

To extract the temperature dependence of the optical conductivity the transmission spectra is fitted with a Lorentzian model of the dielectric constant $\varepsilon(\omega)$ for electric dipole and/or magnetic permeability $\mu(\omega)$ for magnetic dipole transitions as described in Chapter 2 [67, 82]:

$$\varepsilon(\omega) = \varepsilon_\infty + \sum_j \frac{S_j}{\omega_j^2 - \omega^2 - \iota\omega\gamma_j} \tag{5.1}$$

$$\mu(\omega) = 1 + \sum_k \frac{M_k}{\omega_k^2 - \omega^2 - \iota\omega\gamma_k} \tag{5.2}$$

where ε_∞ is the high frequency dielectric constant, j, k enumerates the oscillators, S_j and M_k are spectral weights, $\omega_{j,k}$ is the resonance frequency, and $\gamma_{j,k}$ is the damping rate.

The striking difference between figures 5.2a and 5.2b corresponds to the magnetic dipole and electric dipole absorptions at low temperature for the same thickness. The transmission spectra shows that a strong low frequency absorption in $Eu_{0.75}Y_{0.25}MnO_3$ occurs only in $e||a$ polarization — as was reported for $TbMnO_3$ and $GdMnO_3$ [66]. In $e||c$, the IR active phonons are the only electric dipole features observed (not shown). In the $(e||b, h||a)$ polarization only one weak absorption mode below T_N (fig. 5.2a) is found. Fitting this mode as a $h||a$ magnetic dipole active antiferromagnetic resonance (AFMR) gives the values $\omega = 20$ cm^{-1}, $\gamma = 2.3$ cm^{-1}, and $M = 2.5$ cm^{-2} at 8 K which are typical for the AFMR [82]. In this fit $\varepsilon = 17.5$ was used which was obtained by fitting $e||b$ phonon reflectivity spectra. This AFMR was also observed in the $e||c$, $h||a$ configuration on a $a - c$ plane sample shown in figure 5.3.
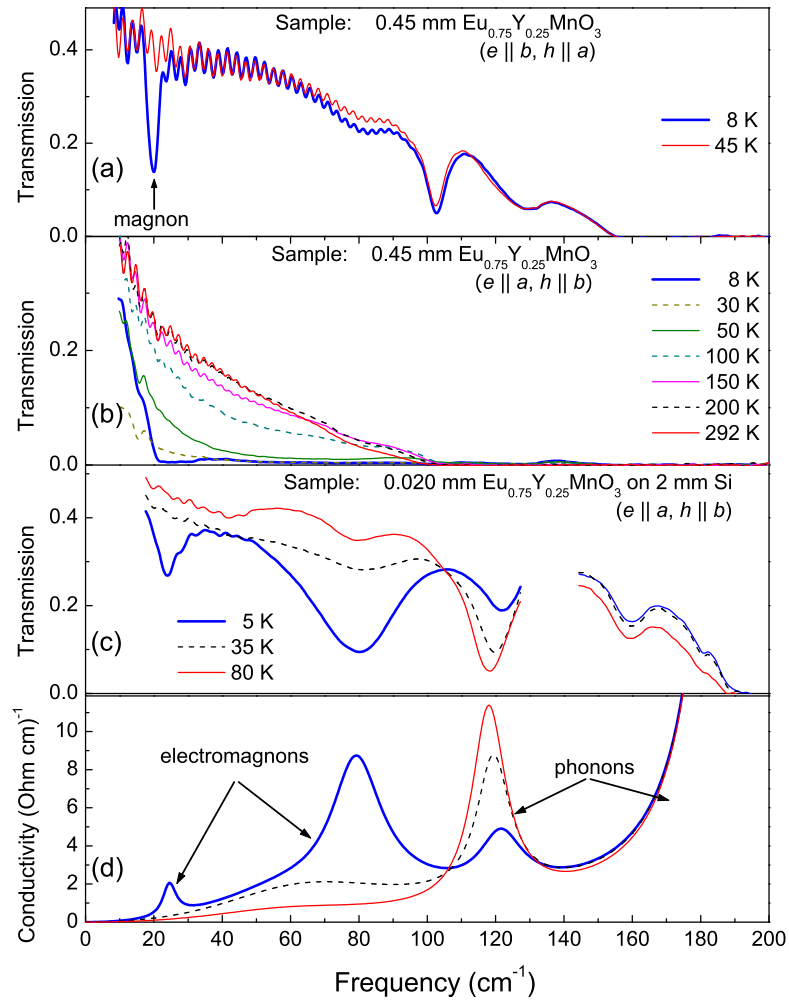
Figure 5.2: (a),(b), and (c) — transmission spectra of $Eu_{0.75}Y_{0.25}MnO_3$ in different polarization configurations; (d)— optical conductivity from fits of spectra in panel (c). e and h are electric and magnetic fields of light.
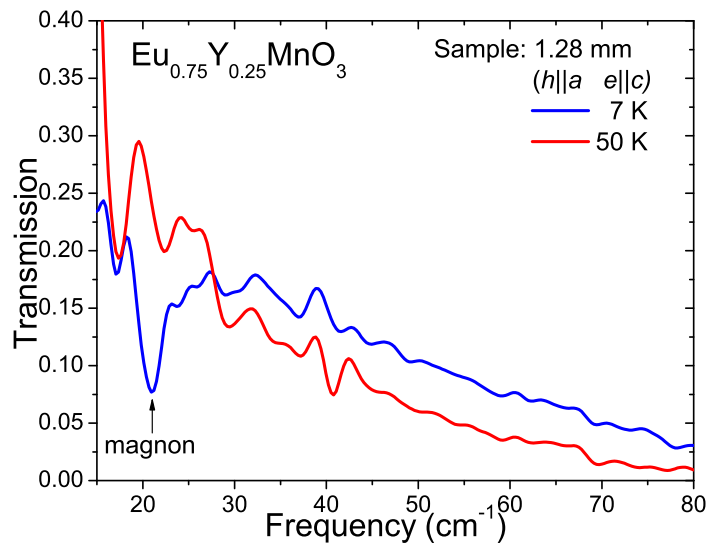
Figure 5.3: Transmission spectrum of $Eu_{0.75}Y_{0.25}MnO_3$ in the $h\|a$, $e\|c$ configuration.

The low temperature trace shows the AFMR absorption also present in figure 5.2(a).

A much thinner sample was used to quantify the $e||a$ spectra as shown in figure 5.2(c). Below T_{FE}, two relatively narrow features appear; a low energy peak at 25 cm^{-1} and a broader absorption at 80 cm^{-1}. The gap in the fig. 5.2(c) data near 140 cm^{-1} is due to absorption in the cold quartz window. An isosbestic point (frequency of constant absorption) is found at 105 cm^{-1} which signifies spectral weight conservation between the low frequency absorption and the phonons. Similar features at 25 and 65 cm^{-1} were observed in a polycrystal of TbMnO$_3$ and the data on single crystal will be shown later.

A broad background absorption is observed as a continuous decrease of the transmission level in fig.5.2(b) in $e||a$ (but not in the $e||b$ or $e||c$ polarizations) and persists to temperatures as high as 150 K. Figure 5.4 shows that this background absorption grows in strength as T decreases (filled upright triangles) and this growth accelerates below $T = T_N$. At $T = 10$ K the background accounts for approximately half of the total low frequency oscillator strength below 140 cm^{-1}.

The optical conductivity obtained by fitting the transmission spectra of fig. 5.2(c) is shown in figure 5.2(d). Three Lorentzians were used to fit the spectra. Their parameters are (ω, γ, S) at 5 K (25, 4, 467), (65, 70, 7708), (79, 17, 7506). The spectral weight of the lowest frequency peak is comparable to the corresponding values for the electromagnons in YMn$_2$O$_5$ and TbMn$_2$O$_5$ (see table 4.1 and [82]). The phonon parameters are (122, 15, 2662) at 5 K and (118, 12, 7456) at 80 K.

The frequencies of the 25 and 80 cm^{-1} peaks show very little temperature dependence and the damping rate decreases, both below T_{FE} (not shown). The temperature
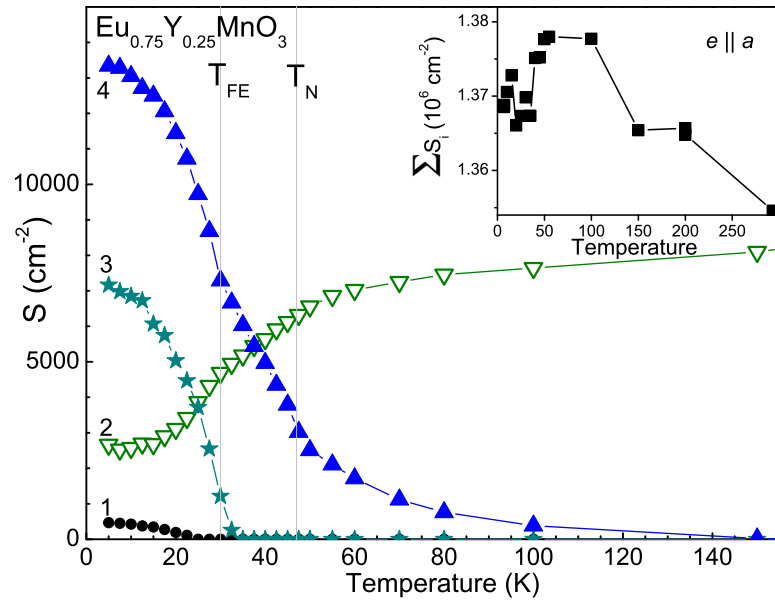
Figure 5.4: Spectral weight of the features below 140 cm^{-1}. Curves show data for: 1) 25 cm^{-1} peak, 2) 120 cm^{-1} phonon, 3) peak at $\sim$80 cm^{-1} and, 4) total spectral weight below 140 cm^{-1} (excluding the phonon). Inset: Total spectral weight of the eight phonons above 140 cm^{-1}.

dependence of the spectral weight of the low frequency modes is shown in Figure 5.4. The phonon spectral weight begins changing significantly around T_N and shows an inflection point at T_{FE}, signaling coupling to the magnetic system. It is seen that the total spectral weight below 140 cm^{-1} is not conserved; there is a net gain of about 6,000 cm^{-2}. To clarify this point, the total spectral weight of the high frequency phonons is shown in the inset. The high frequency phonons are seen to suffer a net loss of 5,000 to 10,000 cm^{-2} below T_N which compensates for the gain of spectral weight below 140 cm^{-1} within experimental error. The change in the phonon strength in 50–295 K range is the usual behavior from thermal contraction. Thus, the new low frequency modes in Eu$_{0.75}$Y$_{0.25}$MnO$_3$ are coupled to, and acquire their optical activity from, all the IR phonon modes.

Further evidence of coupling between the phonons and magnons is visible in the temperature dependence of the phonon frequency in figure 5.5(a). In the temperature range where phonon hardening usually saturates, an onset of additional hardening at T_{FE} and a smaller effect at T_N are observed. Figure 5.5(b) shows the dielectric constant of Eu$_{0.75}$Y$_{0.25}$MnO$_3$. The peak at 30 K in the low frequency curves ($e||a$ and $e||c$) signals the onset of the static FE moment and is related to the dynamical response of ferroelectric domains or due to a relaxation mode. The IR dielectric constant at $\sim$10 cm^{-1} only reproduces a step up in ε_a which is the signature of electric dipole activity of the new modes in $e||a$ polarization. Signatures of these new modes were not found for $e||c$ in either transmission spectra or in the temperature dependence of $\varepsilon_c(0)$.
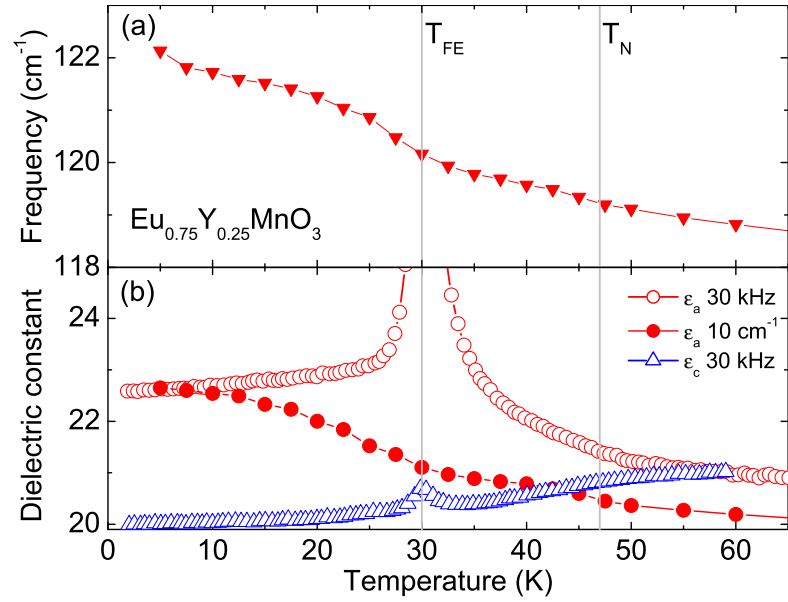
Figure 5.5: (a) Temperature dependence of the phonon frequency that shows hardening at T_{FE}. (b) Dielectric constant of $Eu_{0.75}Y_{0.25}MnO_3$ from fits of infrared spectra in comparison with 30 kHz measurements.

The coupling of the magnons to the lattice leads to mode mixing and therefore spectral weight transfer between the electric dipole active phonons and the magnetic dipole active magnons[32]. The electric dipole activated magnon can be thought of as the Goldstone boson of multiferroicity [32]. In general the lowest order coupling can be written as a trilinear term in the Hamiltonian [19], $H \sim uSS$, where u is the lattice displacement and S is the spin variable. The form of the interaction that can couple the $q = 0$ phonon to one magnon, is $H \sim u_0 S_{-Q} \langle S_{+Q} \rangle$, where $\langle S_{+Q} \rangle$ corresponds to the static magnetic structure.

A quantitative comparison of experiments with theory is limited by the lack of a theoretical treatment for realistic structures including both symmetric and antisymmetric exchange. Katsura, *et al.* [32] have reported a theory of the electromagnon (**em**) for the case of a spin chain with cycloidal order coupled to the lattice by Dzyaloshinskii-Moriya (DM) antisymmetric superexchange. They predict that the **em** should be observed as a $e \perp \mathbf{P} \perp q$ absorption as described in Chapter 1. However the observation is that **em**$||a$ for $Eu_{0.75}Y_{0.25}MnO_3$ as well as for $TbMnO_3$ and $GdMnO_3$, where the static polarization direction and value are different for the three compounds. Therefore the **em** in the $RMnO_3$ multiferroics has a selection rule ($e||a$) which is not borne out by the Katsura model. The model also predicts that the frequency of the **em** should be lower than the AFMR, but, as shown above in figure 5.2, we have observed the opposite. However, the model does predict that the **em** and the AFMR are separate modes as our result also implies.

The 80 cm^{-1} feature is even more problematic within the Katsura picture. In this case the magnon at $q = Q$ is an internal mode in the unit cell and is nearly degenerate with the lowest frequency phonon. However, since mode mixing has generic features, it is interesting to examine the predictions of the Katsura model for this nearly degenerate case. The model can produce the large oscillator strength transfer for a very large DM coupling constant λ but this is accompanied by a large shift, ~ 20 cm^{-1}, in the optical phonon as shown in figure 5.6. The phonon is observed to shift to higher frequencies, consistent with mode repulsion, but only by ~ 2 cm^{-1}, which in the Katsura model means a very small coupling constant (vertical line in fig5.6) and therefore almost no spectral weight transfer from the phonon to the **em**, in stark contradiction with the experiments shown here.

Symmetric exchange coupling should produce similar mode mixing behavior and in principle the coupling strength can be larger than is expected for DM exchange. It has been shown in chapter 4 that symmetric exchange coupling would produce a response of the form **em**||**P** for simple models [13]. While this is the observed selection rule for YMn$_2$O$_5$ and TbMn$_2$O$_5$ where **em**||b||**P**, it is not correct for the RMnO$_3$ systems. Therefore, the experiments imply that the **em** selection rule is associated with the crystal structure and the magnetic structure through the symmetry allowed phonon-magnon coupling. Clearly extending the simple **em** models to include more accurate depictions of the materials is an important task, and it will be presented later.

We note that inelastic neutron scattering can provide important additional informa-
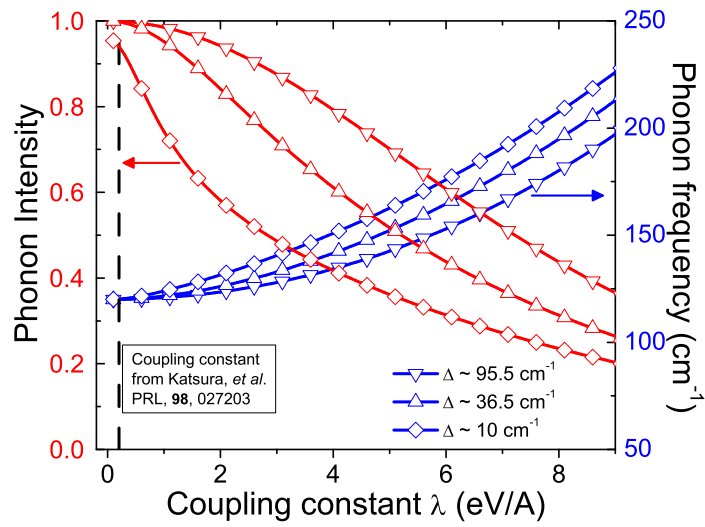
Figure 5.6: Prediction of the KBN model of electromagnons. Plotted are the phonon frequency and intensity as a function of the magnetoelectric coupling constant λ for three different cases of frequency separation Δ between the phonon and the electromagnon.

tion. Data reported by Senff, *et al.* [83] shows good agreement with the low frequency IR data of $TbMnO_3$ [66]. Also S.H. Lee, *et al.* [84] have recently reported good agreement between the sharp **em** features in YMn_2O_5 and the magnons observed in neutron scattering at $q = Q$ favoring the mode mixing scenario for that material as shown in Chapter 4. Mode mixing also implies the onset of magnetic dipole activity of the phonons at T_{FE}. This effect should be investigated experimentally.

The trilinear coupling also allows a two magnon decay of the phonons, by the terms $H \sim u_0 S_q S_{-q}$. The corresponding frequency dependent phonon self energy can produce modifications of the phonon absorption line shape related to the two magnon ($q_1 = -q_2$) density of states. As the two magnon density of states is broad with no narrow spectral features this process is unlikely to produce the observed relatively narrow electromagnon absorption. However, the two magnon process is a good candidate for understanding the broad background absorption observed below as well as above T_N in the $e||a$ polarization. The gradual decrease of this background signal with temperature (Fig. 5.4) above T_N suggests that it originates from magnetic fluctuations. Since there are no long lived magnons for $T > T_N$ this background arises from the coupling of the phonon to the dynamic fluctuations of the magnetic system in the paramagnetic phase. Confirming evidence for this interpretation would be the observation of short range magnetic order in these materials above T_N by inelastic neutron scattering.

At this point it is interesting to ask what is the behavior of these electromagnons under magnetic field. This is because the results above seem to indicate that electro-
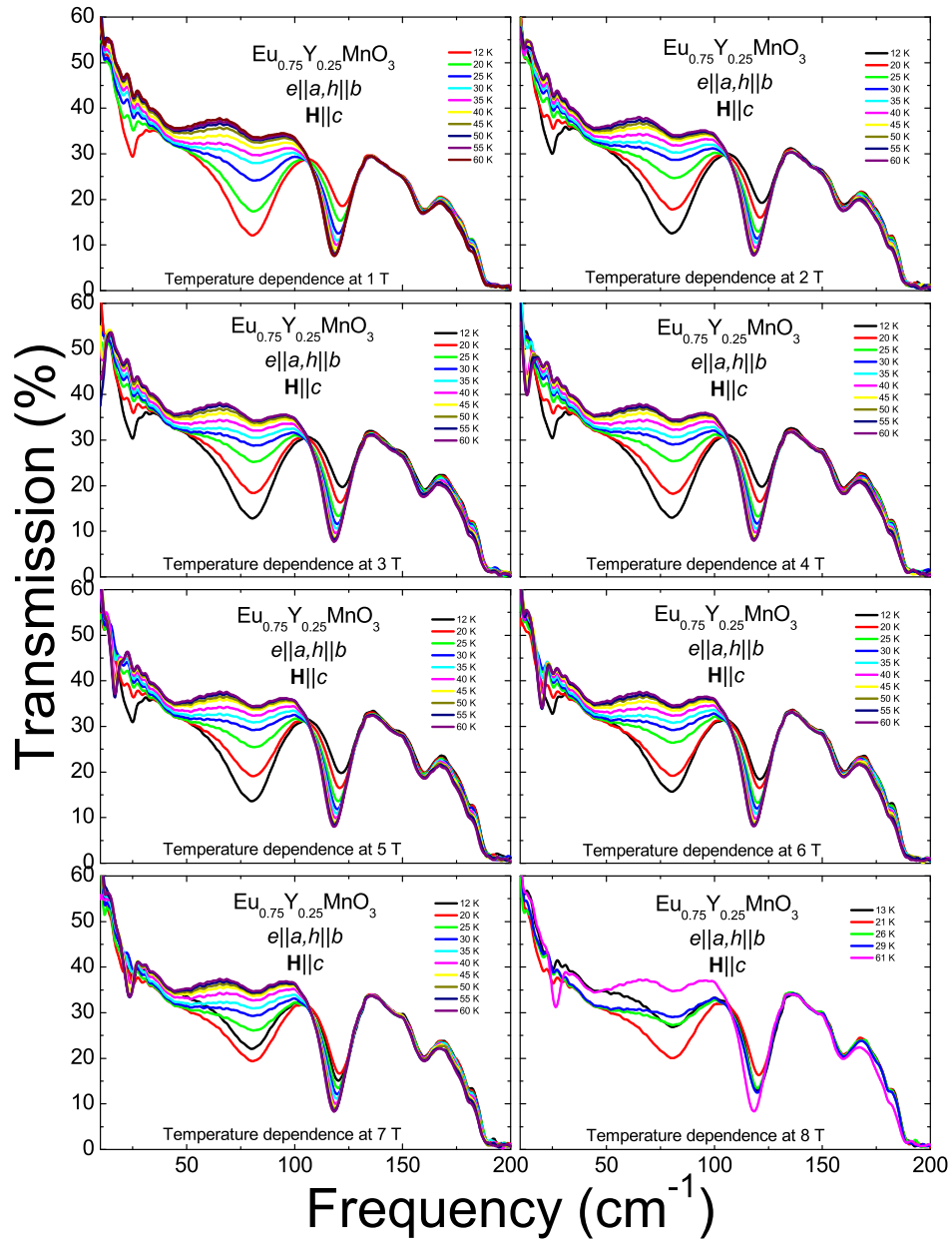
Figure 5.7: Magnetic field and temperature dependence of the transmission spectra in $Eu_{0.75}Y_{0.25}MnO_3$

magnons and polarization are independent, and because the behavior of polarization has been already measured in magnetic field [81], a direct comparison is possible [2]. In order to test this, transmission measurements were done under magnetic field as described in Chapter 2 in the $e||a$, $h||b$ and $\mathbf{H}||c$ configuration. Results of the temperature dependence of the transmission at fixed magnetic fields are shown in figure 5.7. These measurements were done on warming, but the behavior on cooling is highly hysteretical in the region between 6 and 7 T, and below 25 K.

After many cycles of measurements, a phase diagram is built in the $\mathbf{H} - T$ plane shown in figure 5.8. The color coded plot gives the integrated intensity of electromagnon absorption between 3 and 100 cm^{-1}. It is clear from the figure that at low temperatures the magnetic field induces drastic changes until the material losses the electromagnons completely. The points in the plot were obtained from measurements of ε_a and $\mathbf{P}$ as functions of temperature and magnetic field [85]. This behavior of the low frequency electromagnon under magnetic field $\mathbf{H}||c$ was observed in TbMnO$_3$ before [66]. These results, coupled with the static phase diagram of TbMnO$_3$ [81], suggests that even though TbMnO$_3$ and Eu$_{0.75}$Y$_{0.25}$MnO$_3$ have different spiral planes, the electromagnons behave in the same way. In addition, even though electromagnons are independent from polarization, the phase diagram 5.8 suggests that they only exist in the spiral phases, or at least, in the non-collinear ones.

---

[2]The results of experiments in magnetic field has not been published for Eu$_{0.75}$Y$_{0.25}$MnO$_3$, however measurements have been done by Prof. S-W. Cheong's group [85], and he has made these results available to me.
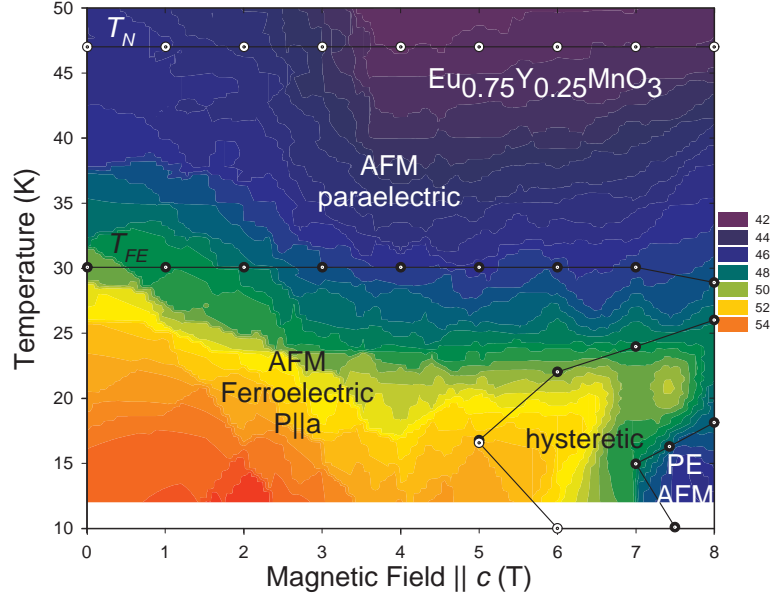
Figure 5.8: Magnetic Field vs. temperature phase diagram in $Eu_{0.75}Y_{0.25}MnO_3$.

Finally, it is also interesting that the transition from the low field phase to the high field one, coincides with a transition from a cycloidal spiral to a canted antiferromagnetic one [86]. This last structure cannot induce ferroelectricity and thus it is paraelectric, as indicated in figure 5.8.

5.3 Origin of Electromagnons in RMnO$_3$

In this section far IR experiments on TbMnO$_3$ are presented together with a model based on the symmetric Heisenberg exchange as the origin of the dynamic magnetoelectric coupling in this family of materials. Two samples of TbMnO$_3$ were used in these measurements: (1) *ab* sample for zero field experiments of size 3×3 mm^2 and 50 μm thick along *a,b* and *c*, respectively (*Pbnm* setting), and an (2) *ac* sample for magnetic

field measurements ($\mathbf{H}||b$) of size $2 \times 2 \times 1$ mm^3 for $e||c$ and then polished to 75 μm for $e||a$. Sample (2) allows access to the phase where ferroelectric polarization $\mathbf{P}$ is changed from the c to the a axis with a field of 5 T at 7 K, and the spiral spin configuration rotates from the bc to ab plane. The transmission spectra were then converted to the absorption coefficient $\alpha(v)$ using $T(v) = (1 - R(v))^2 e^{-\alpha(v)l}$, where l is the sample thickness.

5.3.1   Experimental Results

Figure 5.9(a) shows the spectra in the far infrared taken at zero external magnetic field in TbMnO$_3$. All the features observed have been identified in the spectra of Eu$_{0.75}$Y$_{0.25}$MnO$_3$ as shown in section 5.2 and are described in the caption [87]. Measurements of the far infrared transmission in a magnetic field ($\mathbf{H}||b$) were performed to test the behavior of electromagnons on different spiral states. The spectra taken at 7 K are shown in figure 5.9(b). Above approximately 5 T the system undergoes a spin flop transition from a spiral in the bc plane to an ab plane spiral, yet the electromagnons remain active in the configuration $e||a$ with only a slight shift of their frequencies and an increase of their spectral weight. The color coded phase diagram is shown in figure 5.10 resulting from integrating the absorption coefficient from 15 to 100 cm^{-1}. The symbols mark the boundaries between different phases, in particular T_{flop} is the temperature at which the spiral plane flops from the $b - c$ to the $a - b$ plane.

It is particularly striking that the absorptions activated in the cycloidal phase are only active for light polarization $e||a$ in all systems studied, regardless of the spin plane,
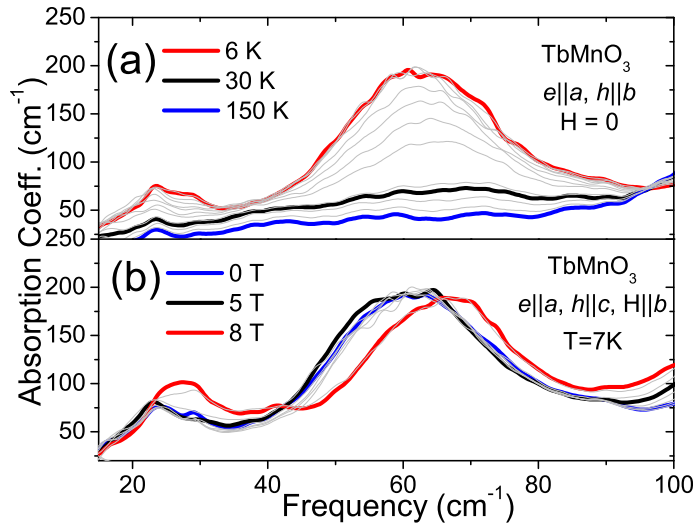
Figure 5.9: (a) Zero field absorption spectra in TbMnO$_3$. Main features of spectra correspond to 2 electromagnon peaks at 25 and 60 cm^{-1} that activate below T_{FE}, and the lowest infrared active phonon just below 120 cm^{-1}. Additionally, the temperature dependence of the spectra shows that there is a broad absorption below the phonon that persists well above T_N. (b) Magnetic field dependence of the low temperature spectrum with **H** $\parallel$ b. The frequencies of the electromagnons shift in the high field phase, and their intensities increase.
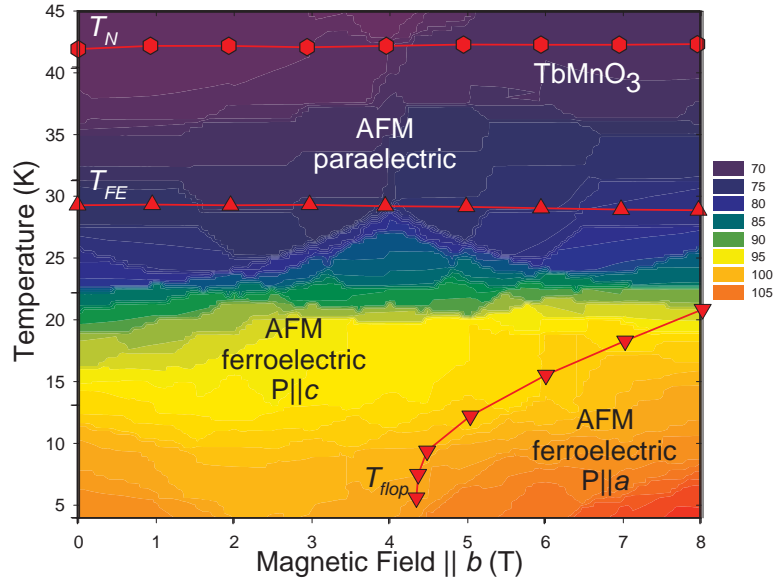
Figure 5.10: Magnetic Field vs. temperature phase diagram in TbMnO$_3$.

or static polarization direction or value. This observation directly contradicts the prediction of KBN [32] on the electrodynamics of spiral multiferroics. Indeed the inadequacy of this mechanism is also suggested by the large Born effective charge required in the KBN model to account for the experimentally observed oscillator strength. The observed selection rule clearly indicates that account must be taken of the specific characteristics of these manganites, such as the crystal structure and anisotropic magnetic interactions, in order to find an accurate description of the electromagnon excitations.

In order to test the possibility of observing electromagnons that follow the KBN prediction, we have performed measurements in the $\mathbf{H}\|b$, $e\|c$, $h\|a$ configuration. The absorption spectra are shown in figure 5.11. The spectrum in the high field phase shows clearly an absorption feature around 21 cm^{-1}. By fitting the transmission spectrum with
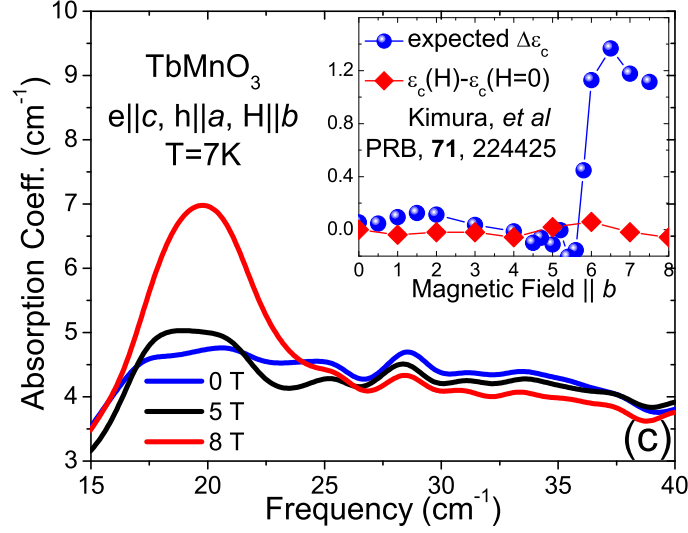
Figure 5.11: Absorption spectrum for the expected polarization of the KBN electromagnon. The new absorption line around 21 cm^{-1} in the high field phase is magnetic dipole active given that the expected contribution to ε (shown in the inset) is larger than found in the static measurements.

a model electric dipole active excitation the putative contribution to the static dielectric function ε is $\Delta\varepsilon \approx 1.2$ as shown in the inset. This change in ε is not observed in the static data [81], showing that this feature is not an electric dipole excitation. Therefore this excitation is a magnetic dipole ($h\|a$) antiferromagnetic resonance (AFMR) as expected from the magnetic order [33]. For comparison, note that in the zero field spectra in the $e\|b$, $h\|c$ configuration an AFMR around 22 cm^{-1} is observed as shown in figure 5.12. This means that the $h\|c$ magnon rotates together with the spin plane thereby changing its selection rule to $h\|a$, completely consistent with the change of polarization direction
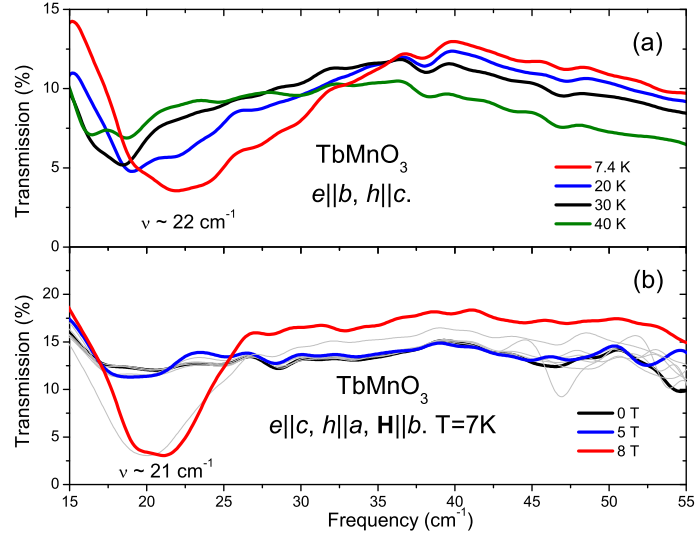
Figure 5.12: Transmission spectra of TbMnO$_3$ in the (a) $h||c,e||b$ at zero field, and (b) $h||a,e||c$ in $\mathbf{H}||b$ configurations.

[1] and recent neutron scattering measurements [88].

5.3.2 Theory

A mechanism specific to rare earth manganites that only involves the symmetric Heisenberg exchange between non-collinear spins [13] and, therefore, is not sensitive to the orientation of the spiral plane is presented. The polarization of electromagnon in this case is always parallel to the a axis, in agreement with experiments.

The essential features of magnetic excitations in the spiral state can be understood

within a model including only superexchange interactions between Mn spins,

$$H_{\text{ex}} = \frac{1}{2} \sum_{i,j} J_{ij} \mathbf{S}_i \cdot \mathbf{S}_j. \tag{5.3}$$

When magnetic anisotropies are neglected, the 4 Mn ions in the unit cell of $R\text{MnO}_3$, located at $\mathbf{R}_1 = (\frac{1}{2}, 0, 0)$, $\mathbf{R}_2 = (0, \frac{1}{2}, 0)$, $\mathbf{R}_3 = (\frac{1}{2}, 0, \frac{1}{2})$, and $\mathbf{R}_4 = (0, \frac{1}{2}, \frac{1}{2})$, become magnetically equivalent (see Fig. 5.13). The competition between the nearest-neighbor ferromagnetic exchange, $J = J_{i,i+(b\pm a)/2} < 0$, and the antiferromagnetic next-nearest-neighbor exchange along the b axis, $J_b = J_{i,i+b} > 0$, favors the circular spin spiral with the wave vector $Q \| b$, where $\cos\frac{Q}{2} = \frac{|J|}{2J_b}$, provided that $J_b > \frac{|J|}{2}$ and $J_a = J_{i,i+a} < \frac{J^2}{4J_b}$. The antiferromagnetic exchange along the c axis, $J_c = J_{i,i+c/2} > 0$, gives rise to the 'double spiral' structure with antiparallel spins in neighboring ab layers:

$$\langle \mathbf{S}_i \rangle = \pm S \left(\hat{\mathbf{c}} \cos \mathbf{Q} \cdot \mathbf{r}_i - \hat{\mathbf{b}} \sin \mathbf{Q} \cdot \mathbf{r}_i \right), \tag{5.4}$$

where the upper/lower sign corresponds the ab layers with integer/half-integer z/c. The bc plane is favored e.g. by the single-ion anisotropy, $\frac{K}{2} \sum_i (S_i^a)^2$ with $K > 0$, which does not spoil the equivalence of Mn sites (effects of other magnetic anisotropies are discussed below).

The magnon spectrum in $R\text{MnO}_3$ has acoustical and optical branches. Their dispersion for a circular spiral is plotted in Fig. 5.14(a) with, respectively, blue dashed and red solid line, as a function of the wave vector $\mathbf{k}$ in the co-rotating spin frame, in which $\langle \mathbf{S} \rangle \| \hat{z}$ on all sites. For acoustical magnons the order parameter $\mathbf{L} = \mathbf{S}_1 + \mathbf{S}_2 - \mathbf{S}_3 - \mathbf{S}_4$ oscillates in the spiral plane, while optical magnons correspond to out-of-plane oscillations

of **L**. The KBN electromagnon is the symmetric superposition of the optical magnons with the wave vectors $+\mathbf{Q}$ and $-\mathbf{Q}$, while the interaction Eq.(5.5) couples electric field through the alternation of the Heisenberg exchange along the b axis to the acoustical magnon with $\mathbf{k_0}$ at the zone boundary. This excitation corresponds to relative rotations of the spins $\mathbf{S}_1$ and $\mathbf{S}_2$ in the spiral plane, which occur in anti-phase with the rotations of the spins $\mathbf{S}_3$ and $\mathbf{S}_4$ and result in alternation of the angle between neighboring spins along the spiral propagation vector. This mechanism works only for noncollinear spins because the first order variation of the exchange energy with respect to spin oscillations is zero for collinear spins, similarly to the model applicable to the $R\mathrm{Mn_2O_5}$ family in Chapter 4.

Due to the $\mathrm{GdFeO_3}$ distortion of $R\mathrm{MnO_3}$ compounds, oxygen ions mediating the superexchange between nearest-neighbor spins in the ab layers are displaced from the straight lines connecting two neighboring Mn ions in ab layers as shown in Fig. 5.13. When an applied electric field shifts all oxygen ions by an equal distance along the a axis, the exchange constants $J_{1,2}$ and $J_{1,2+a}$ will be changed by ΔJ proportional to the applied field, while the exchange constants $J_{1+b,2}$ and $J_{1+b,2+a}$ will be changed by $-\Delta J$. In other words, due to the alternating rotations of the $\mathrm{MnO_6}$ octahedra in $R\mathrm{MnO_3}$, a uniform electric field in the a direction gives rise to an alternation of the nearest-neighbor exchange along the spiral propagation vector $Q\|b$, $J \propto J_0 + \Delta J\cos(\mathbf{k_0} \cdot \mathbf{r})$ where $\mathbf{k_0} = (0, \frac{2\pi}{b}, 0)$. The corresponding coupling of spins to the electric field $e\|a$ compatible

with the *Pbnm* symmetry has the form:

$$H_{me} = - gE_a \sum_j \left[(\mathbf{S}_{1,j} - \mathbf{S}_{1,j+b}) \cdot (\mathbf{S}_{2,j} + \mathbf{S}_{2,j+a}) \right.$$
$$\left. + (\mathbf{S}_{3,j} - \mathbf{S}_{3,j+b}) \cdot (\mathbf{S}_{4,j} + \mathbf{S}_{4,j+a}) \right], \tag{5.5}$$

where the indices $1 - 4$ label different Mn ions in a unit cell while j labels cells.

This mechanism of dynamic magnetoelectric coupling works only for non-collinear spins because the first-order variation of the exchange energy $\propto (\mathbf{S}_i \cdot \mathbf{S}_j)$ with respect to spin oscillations $\delta \mathbf{S}_i(t) = (\mathbf{S}_i(t) - \langle \mathbf{S}_i \rangle) \perp \langle \mathbf{S}_i \rangle$ is zero for collinear spins. Although interactions of spins with $e\|b$ and $e\|c$, similar to Eq.(5.5), are allowed by symmetry, they give rise to alternation of the nearest-neighbor exchange constants in the directions orthogonal to the spiral wave vector $\mathbf{Q}$ and do not lead to single-magnon excitations by electric field, as neighboring spins along the a and c axes are collinear. This explains why the polarization of electromagnon in RMnO$_3$ parallel to the a axis independently of the orientation of the spiral plane.

Note that the coupling Eq.(5.5) induces a static electric polarization $P\|a$ in RMnO$_3$ with the collinear antiferromagnetic ordering of the E-type [14], for which the scalar product of neighboring spins alternates along the b axis. This fact allows the estimation of polarization in the E-phase using the optical absorption data for the spiral phase (the direct measurement of P_E is difficult due to absence of single crystal samples). The total spectral weight of the 60 cm^{-1} peak, $S \approx 7000$ cm^{-2}, corresponds to $P_E \sim 1\mu$C/cm^2, in perfect agreement with *ab initio* calculations [89]. For comparison, the spectral weight of the KBN electromagnon, calculated from the polarization $P \sim 600\mu$C/m^2 in the spi-

112
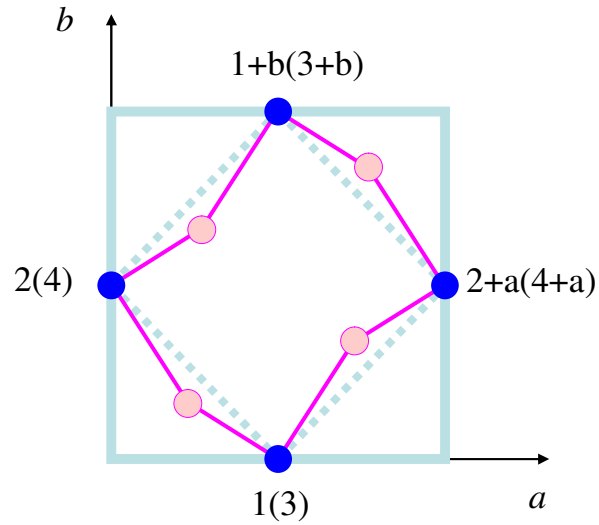
Figure 5.13: One *ab* layer of the *Pbnm* unit cell of RMnO$_3$ consisting of 4 manganese ions (blue circles) and 4 oxygen ions (pink circles). The displacements of the oxygen ions from the midpoints of the straight lines (dashed lines) connecting neighboring Mn ions are $\delta r_{1+b,2+a} = (\delta x;\ \delta y;\ \delta z)$, $\delta r_{1,2} = (-\delta x;\ -\delta y;\ -\delta z)$, $\delta r_{1,2+a} = (-\delta x;\ \delta y;\ \delta z)$, and $\delta r_{1+b,2} = (\delta x;\ -\delta y;\ -\delta z)$. The labels of the manganese ions in the next layer are given in parentheses. The displacements of the oxygen ions in the next layer have opposite δz.

ral phase of TbMnO$_3$, is only ≈ 10 cm^{-2}. The photoexcitation of magnons through the magnetoelectric coupling Eq.(5.5) of exchange origin, which is about 2 orders of magnitude stronger than the relativistic coupling in spiral manganites, is much more effective than the KBN mechanism.

As Eq.(5.5) only involves scalar products of spins, the resulting electromagnon peak is insensitive to the orientation of the spiral plane. Instead, it is tied to the crystal structure of RMnO$_3$ and only depends on the direction of the spiral propagation vector $\mathbf{Q}$, which stays constant in an applied magnetic field. Similar interactions of spins with $e\|b$ and $e\|c$, give rise to alternation of nearest-neighbor exchange constants in the directions orthogonal to the spiral wave vector $\mathbf{Q}$, which do not allow for single-magnon excitations by electric field, as neighboring spins along the b and c axes are collinear.

The coupling Eq.(5.5), as well as another invariant, $E_a[(\mathbf{S}_1 - \mathbf{S}_{1+c}) \cdot \mathbf{S}_3 - (\mathbf{S}_2 - \mathbf{S}_{2+c}) \cdot \mathbf{S}_4]$, also gives rise to the photo-excitation of a pair of magnons with the total wave vector $\mathbf{k}_0$ (the so-called 'charged magnons' [65]). Charged magnons are also excited by $e\|c$ and $e\|b$ through couplings similar to Eq.(5.5). The calculated shape of the bi-magnon continuum is shown in Fig. 5.14(b). Its maximum is located around the electromagnon frequency and its total spectral weight is only $\sim 10\%$ of the spectral weight of the single-magnon peak. This, together with the fact that bi-magnons can also be excited by $e\|c$ and $e\|b$ through couplings similar to Eq.(5.5), indicates that the experimental peak at 60 cm^{-1} results from the photoexcitation of a single zone-boundary magnon. This magnon can be identified in the recent neutron scattering results of Senff, *et al.*[90].

114
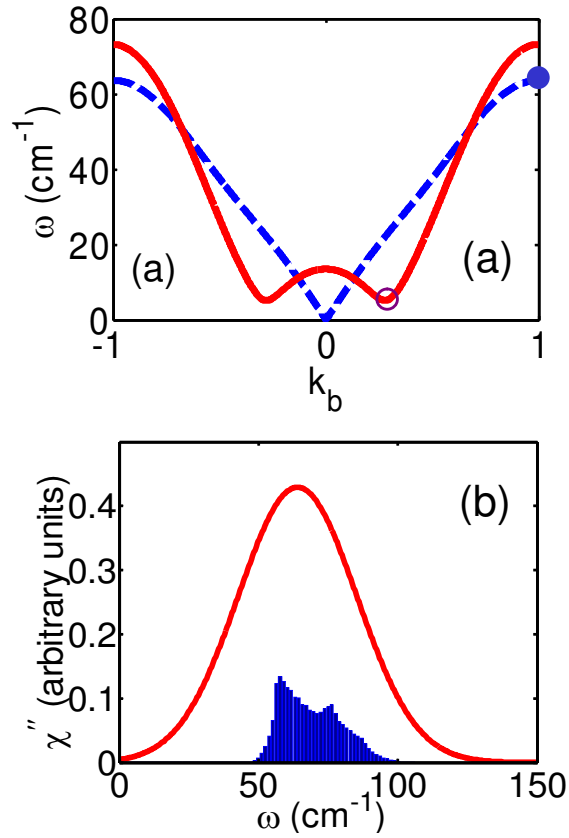
Figure 5.14: (a) The typical magnon spectrum for a circular bc-spiral along $\mathbf{k} = (0, k_b, 0)$, where k_b is measured in units of $\frac{2\pi}{b}$. The empty and filled circles mark the position of, respectively, the KBN electromagnon and the electromagnon excited through the rotationally invariant coupling Eq.(5.5). (b) The histogram shows the corresponding bi-magnon spectrum. For comparison also the (arbitrarily broadened) single-magnon peak is plotted (solid line).

Concerning the nature of the weaker 25 cm^{-1} peak, we note that beyond the simple circular-spiral model the magnon wave vector $\mathbf{k}$ is not conserved and a number of different mechanisms couple high- and low-frequency magnons. For example, the spiral ellipticity that results from the anisotropy in the spiral plane, gives rise to satellite peaks at $\mathbf{k}_0 \pm 2\mathbf{Q}$, $\mathbf{k}_0 \pm 4\mathbf{Q}$.... Furthermore, the alternation of the b-component of the Dzyaloshinskii vectors for pairs of neighboring spins along the b axis,

$$[(\mathbf{S}_1 + \mathbf{S}_{1+b}) \times (\mathbf{S}_2 + \mathbf{S}_{2+a})]_b - [(\mathbf{S}_3 + \mathbf{S}_{3+b}) \times (\mathbf{S}_4 + \mathbf{S}_{4+a})]_b \qquad (5.6)$$

resulting from the GdFeO$_3$ distortion, couples the zone boundary electromagnon with $\mathbf{k} = \mathbf{k}_0$ to the antisymmetric superposition of acoustic magnons with $\mathbf{k} = \pm\mathbf{Q}$. This magnon-magnon coupling (different from the magnetoelectric coupling inducing the static polarization in the spiral state) remains unchanged at the flop of the spiral plane, as it only involves the a and c components of spins. There are, furthermore, anisotropic spin-spin interactions insensitive to the flop transition (e.g. involving products $S_i^a S_j^c$) which couple the electromagnon with $\mathbf{k} = \mathbf{k}_0$ to magnons with $\mathbf{k} = \pm\mathbf{Q}$. Conversely, similar relativistic couplings that do change at the flop transition, do not couple the zone-boundary electromagnon to low-frequency magnons, suggesting that this low frequency electromagnon also originates from Heisenberg interactions. Which of these mechanisms gives the dominant contribution to low-frequency absorption is not clear, but all of them are different from the coupling inducing electric polarization in the spiral state.

5.4 Conclusion

Summarizing the results: 1) the well defined absorption peaks at 25 and 80 cm^{-1} in Eu$_{0.75}$Y$_{0.25}$MnO$_3$ and 25 and 60 cm^{-1} in TbMnO$_3$ arise from mode mixed phonon-magnon excitations — electromagnons with a selection rule $e_\omega \| a$ tied to the crystal structure and independent of the spin plane, and 2) there exists colossal coupling between magnon and phonons that leads to the spectacular loss of spectral weight of the low frequency 120 cm^{-1} polar phonon. In conclusion, we have presented data and a theoretical model that strongly support the Heisenberg exchange interaction as the origin of the magnetoelectric dynamics in the family of multiferroics RMnO$_3$. Additionally, the fact that these excitations are observed both in the neutron measurements and the IR experiments reflects their origin as single-particle excitations of a hybrid electromagnon nature. The surprising outcome of this study is that optical data can be used to explore properties of competing ferroelectric states: from the measured spectral weight of the electromagnon peak in the spectrum of spiral manganites the value of the spontaneous polarization in manganites with the E-type collinear ordering was estimated. These results imply that the dynamic magnetoelectric coupling is in general different from the static one and that electromagnons can be observed in non-multiferroic materials with non-collinear spin orders, which opens a new avenue of investigation of the dynamic properties of frustrated magnets.

Chapter 6

Summary and Outlook

6.1 Summary

The main result of this dissertation is the discovery of a new kind of elementary excitation in multiferroic materials. This new excitation, the electromagnon, is a result of the fundamental coupling between magnons and phonons in magnetic materials. In the families investigated here, $R\mathrm{Mn_2O_5}$ and $R\mathrm{MnO_3}$, electromagnons are present only in phases where the magnetic structure is non-collinear. Based on models that use only the symmetric Heisenberg interaction between spins, the main experimental findings are reproduced, namely, the selection rule and identification with magnons found in neutron scattering experiments.

6.1.1 $R\mathrm{Mn_2O_5}$

A clear signature of inversion symmetry loss was found in the infrared phonon spectrum in the form of the appearance of a new phonon in the ferroelectric phase, that in the paraelectric phase is only Raman active. This suggests that the lattice is involved in this transition, but also that, by the absence of a soft phonon, the transition to the ferroelectric phase is non-conventional. In addition, the contribution from the polar phonons

to the static dielectric constants ε is not enough to account for the anomalies observed in its temperature dependence. This prompted the study of even lower frequency (far infrared) dynamics in this system and resulted in the discovery of electromagnons.

Electromagnons in RMn$_2$O$_5$ are only active for $e_\omega||b$ which is parallel to the static polarization. This selection rule results because electromagnons and static ferroelectric polarization share the same origin. This magnetoelectric coupling originates from the dependence of the exchange interaction on the distance between Mn^{3+} and Mn^{4+} spins. This sensitivity comes about because of the magnetic frustration inherent in this material. With so many competing interactions to be satisfied, spins find that energy can be lowered by relaxing into complex magnetic structures that, by symmetry, allow ferroelectricity and electromagnons.

Very clear confirmation of this is given by the observation of electromagnons in neutron scattering experiments. This type of experiments can, in principle and with enough time, map out the complete dispersion of the magnons. By looking at the wave vector that corresponds to the magnetic structure, the magnons are observed at the same exact energies of the absorption in the far infrared. This means that electromagnons are truly a hybrid mode made out of magnon and phonon character.

6.1.2 RMnO$_3$

Following the results for RMn$_2$O$_5$, the focus shifted to the family of multiferroics RMnO$_3$. This family of multiferroics is structurally simpler and the origin of its fer-

roelectric state seems to be incontrovertible. However the observations ruled out that electromagnons have the same origin as the static polarization because the selection rule of electromagnons is $e_\omega || a$ independent of the spin plane of polarization direction. This selection rule results from the dependence of the exchange integral on the angle formed between two Mn and one O ion (the Mn–O–Mn angle). This angle is effectively modulated along the b axis by the application of an electric field, as in the case of polarized light, directed along the a axis. This modulation results in the effective coupling between the phonon that modulates the angle, and the magnon at the wave vector $Q = (0, \pi/b, 0)$ with anti-phase oscillations within the spin plane.

Because this coupling originates from the crystal structure of this family of multiferroic, it is insensitive to the spin plane. In fact this coupling, when applied to a collinear structure where spins point in the a direction with wave vector $Q = (0, 1/2, 0)$ (the so-called E phase), produces a static ferroelectric polarization. This result allows the estimation of the polarization value in the E-phase multiferroics from the measurement of the spectral weight of electromagnons in the incommensurate spiral multiferroics. This gives a very strong support that this coupling term is active in the whole family of distorted perovskites $R\text{MnO}_3$.

Further confirmation was found in the neutron scattering spectrum of TbMnO_3. This results confirms that the strong electromagnon in the far infrared is indeed the zone boundary magnon observed in the neutron experiments. Again this reaffirm that the electromagnons in $R\text{MnO}_3$ are hybrid excitations of magnon and phonon character.

6.2 Outlook

The results found in this dissertation point very clearly for future studies in multiferroics, and magnetic materials in general. First, electromagnons might be found in other non-collinear multiferroics. This origin might be the same as the polarization's origin as in $R\mathrm{Mn_2O_5}$, or perhaps a different one can be found when analyzing the specifics of the magnetic interactions and crystal structure, as was done in $R\mathrm{MnO_3}$.

Second, electromagnons might be found in magnetic materials that are not necessarily multiferroic but that are non-collinear. This would be very important, because it would generate more interest in the electrodynamics of magnetic materials, and the nature of magnetic frustration and complex magnetic structures could be studied from a very different perspective from the ones used so far.

Thirdly, it is important to note that even though electromagnons are responsible for some of the anomalies in ε found at magnetic transitions, the most noticeable anomaly not explained by electromagnons is the peak that occurs at the ferroelectric transition in ε, as observed in figures 4.5 and 5.5(b). This peak might be due to the relaxation mode discussed in Chapter 1 in the context of order-disorder ferroelectric transitions. This mode is usually associated with motions of ferroelectric domains and its relaxation frequency lies in the microwave (Ghz) part of the spectrum. Therefore, the study of the dielectric response at these frequencies might answer the question of the nature of the excitation responsible for this peak anomaly.

Appendix A

Selection Rules for Phonons

The determination of the selection rules for the observation of the optical phonons at the Brillouin zone center ($\mathbf{k} = 0$) is the topic of this appendix. A method called *nuclear site group analysis* developed in [91] is summarized here and applied to the multiferroics $R\text{Mn}_2\text{O}_5$.

A.1 Symmetry properties of crystals

The symmetry of a crystal of infinite size is described fully by its *space group*. The space group is a set of mathematical operations that, when applied to the crystal, leave all the positions of the atoms either unchanged or translated to a symmetry equivalent place. The space group is composed of translational and rotational operations. The rotational operations also form a group called the *point group*. The point group contains operations that are not purely rotational, in addition to these, it contains screw axis and glide plane operations. The screw axis operation consists of a rotation followed by a translation along the axis by a fractional amount of the full translational symmetry. Glide plane operations consist of a reflection across the plane followed by a translation in the plane, again by a fractional amount. Finally, the concept of the *factor group* is also important, this is the set of operations of the space group without any translations,

including those who are part of screw axis or glide planes. The usefulness of the factor group, is that it allows the symmetry description of an infinite crystal to be reduced to the description of a single unit cell. Within a unit cell, there are sets of points that share the same environment, that is, they have the same site symmetry. The members belonging to the same site symmetry can be transformed into one another by applying the operations of the factor group.

The number of lattice modes which arise from each equivalent set of sites, their symmetries and selection rules can be found with the following procedure. Assume that the ith set of atoms is located in a site of symmetry g_i within a unit cell of a crystal of point group G, g_i is a subgroup of G. In g_i, there will be irreducible representations that transform in the same way as the vector components of a displacement, or polar vector. These irreducible representations of g_i are said to be infrared active. The irreducible representations of G to which the infrared active irreducible representations of g_i map, give the infrared active irreducible representations of G that arise from the ith set of atoms, and correspond to the lattice modes of this set.

When two or three of the vector components transform in the same way under the operations of g_i, these modes contributions to the total number of modes needs to be multiplied by two and three, respectively. A way to check the mapping operation, is that for each site symmetry g_i, the total number of lattice modes (the number of non-degenerate plus two times the number of doubly degenerate plus three times the number of triply degenerate modes) is three times the number of atoms occupying the ith site.

123

Table A.1: Site symmetry decompositions of normal modes for RMn$_2$O$_5$.

Atom	Site Symmetry	Site Representations
R	C_s^{xy}	$2A_g + A_u + 2B_{1g} + B_{1u} + B_{2g} + 2B_{2u} + B_{3g} + 2B_{3u}$
Mn1	C_2^z	$A_g + A_u + B_{1g} + B_{1u} + 2B_{2g} + 2B_{2u} + 2B_{3g} + 2B_{3u}$
Mn2	C_s^{xy}	$2A_g + A_u + 2B_{1g} + B_{1u} + B_{2g} + 2B_{2u} + B_{3g} + 2B_{3u}$
O1	C_2^z	$A_g + A_u + B_{1g} + B_{1u} + 2B_{2g} + 2B_{2u} + 2B_{3g} + 2B_{3u}$
O2	C_s^{xy}	$2A_g + A_u + 2B_{1g} + B_{1u} + B_{2g} + 2B_{2u} + B_{3g} + 2B_{3u}$
O3	C_s^{xy}	$2A_g + A_u + 2B_{1g} + B_{1u} + B_{2g} + 2B_{2u} + B_{3g} + 2B_{3u}$
O4	C_1	$3A_g + 3A_u + 3B_{1g} + 3B_{1u} + 3B_{2g} + 3B_{2u} + 3B_{3g} + 3B_{3u}$
	Raman	$13A_g + 13B_{1g} + 11B_{2g} + 11B_{3g}$
	Infrared	$8B_{1u} + 14B_{2u} + 14B_{3u}$

This immediately means that the total number of modes in the unit cell is $3N$, where N is the number of atoms in the unit cell, where 3 of these modes correspond to uniform displacements of the unit cell called acoustic modes. This makes the total number of optical modes $3(N-1)$. In order to apply this technique the following information is needed: the space and point groups of the crystal, as well as the site symmetry and positions of the atoms in the unit cell. Then one must map out the irreducible representations of each site into the irreducible representations of the point group.

A.2 Examples

The example of the application of this method to find the selection rule of the lattice modes is the multiferroic family $R\mathrm{Mn_2O_5}$. These compounds belong to the *Pbam* space group, with point group symmetry *mmm* and has four chemical formula units in the unit cell ($Z = 4$). The first 2 columns in table A.1 give the site symmetry of each atom in the compound. In order to map the site symmetry representations into the irreducible representations of the unit cell point group, we need character tables for each (character tables can be accessed on-line at [92]). Below, the character tables of the point group *mmm* (D_{2h}) and the point group C_s are reproduced. The left column lists the irreducible representations of the point group, the first row lists the symmetry operations of the group and the middle columns list how each irreducible representation transforms under the operation, these numbers are called the characters. The last column lists the component of the polar vector which transforms as each of the irreducible representations.

125

Table A.2: Character table for Point Group C_s.

C_s	1	σ^{xy}	Selection Rule
A'	1	1	x,y
A"	1	-1	z

Table A.3: Character table for Point Group D_{2h}.

D_{2h}	1	C_2^z	C_2^y	C_2^x	I	σ^{xy}	σ^{xz}	σ^{yz}	Selection Rule
A_g	1	1	1	1	1	1	1	1	
A_u	1	1	1	1	-1	-1	-1	-1	
B_{1g}	1	1	-1	-1	1	1	-1	-1	
B_{1u}	1	1	-1	-1	-1	-1	1	1	z
B_{2g}	1	-1	1	-1	1	-1	1	-1	
B_{2u}	1	-1	1	-1	-1	1	-1	1	y
B_{3g}	1	-1	-1	1	1	-1	-1	1	
B_{3u}	1	-1	-1	1	-1	1	1	-1	x

126

Now, the representations of C_s that transform as components of polar vectors are mapped to the point group by picking the columns of the common operations, in this case 1 and σ^{xy}, and making the correspondence between the representations. Therefore the correspondence is A_g, B_{1g}, B_{2u} and $B_{3u} \Rightarrow$ A', and A_u, B_{1u}, B_{2g} and $B_{3g} \Rightarrow$ A". Because A' is doubly degenerate, its contribution is multiplied by 2, making then the total contribution of normal modes from each atom at site C_s^{xy} equal to $2A_g + A_u + 2B_{1g} + B_{1u} + B_{2g} + 2B_{2u} + B_{3g} + 2B_{3u}$. This procedure is then repeated for each site symmetry which then gives the last column in table A.1.

Finally the total number of lattice modes is decomposed as $13A_g + 9A_u + 13B_{1g} + 9B_{1u} + 11B_{2g} + 15B_{2u} + 11B_{3g} + 15B_{3u}$. Of these, $B_{1u} + B_{2u} + B_{3u}$ correspond to the 3 acoustic modes, $9A_u$ are silent, $13A_g + 13B_{1g} + 11B_{2g} + 11B_{3g}$ are Raman active and $8B_{1u} + 14B_{2u} + 14B_{3u}$ are infrared active with the selection rule given in the character table A.3.

Bibliography

[1] T. Kimura, T. Goto, H. Shintani, K. Ishizaka, T. Arima, and Y. Tokura. Nature **426** (2003), 55.

[2] M. Fiebig. J. Phys. D: Appl. Phys. **38** (2005), R123.

[3] H. Schmid. Ferroelectrics **162** (1994), 665.

[4] ISI Web of Knowledge (2008). URL `http://isi10.isiknowledge.com`.

[5] H. Katsura, N. Nagaosa, and A. V. Balatsky. Phys. Rev. Lett. **95** (2005), 057205.

[6] T. Moriya. Phys. Rev. **120** (1960), 91.

[7] I. Dzyaloshinsky. J. Phys. Chem. Solids **4** (1958), 241.

[8] I. A. Sergienko and E. Dagotto. Phys. Rev. B **73** (2006), 094434.

[9] M. Mostovoy. Phys. Rev. Lett. **96** (2006), 067601.

[10] C. Jia, S. Onoda, N. Nagaosa, and J. H. Han. Phys. Rev. B **76** (2007), 144424.

[11] J. Hu. Phys. Rev. Lett. **100** (2008), 077202.

[12] S.-W. Cheong and M. Mostovoy. Nature Materials **6** (2007), 13.

[13] A. B. Sushkov, M. Mostovoy, R. Valdés Aguilar, S.-W. Cheong, and H. D. Drew. J. Phys.: Condens. Matter **20** (2008), 434310.

[14] I. A. Sergienko, C. Sen, and E. Dagotto. Phys. Rev. Lett. **97** (2006), 227204.

[15] Y. J. Choi, H. T. Yi, S. Lee, Q. Huang, V. Kiryukhin, and S.-W. Cheong. Phys. Rev. Lett. **100** (2008), 047601.

[16] V. G. Baryakhtar, L. V. Lvov, and D. A. Yablonskii. JETP Letters **37** (1983), 673.

[17] A. P. Levanyuk and D. G. Sannikov. Sov. Phys. Usp. **17** (1974), 199.

[18] A. M. Kadomtseva, S. S. Krotov, Y. F. Popov, G. P. Vorobev, and M. M. Lukina. JETP **100** (2005), 305.

[19] A. B. Harris. Phys. Rev. B **76** (2007), 054447.

[20] N. Hur, S. Park, P. Sharma, J. Ahn, S. Guha, and S.-W. Cheong. Nature **429** (2004), 392.

[21] G. Lawes, A. B. Harris, T. Kimura, N. Rogado, R. J. Cava, A. Aharony, O. Entin-Wohlman, T. Yildrim, M. Kenzelmann, C. Broholm, and A. P. Ramirez. Phys. Rev. Lett. **95** (2005), 087205.

[22] P. G. Radaelli and L. C. Chapon. Phys. Rev. B **76** (2007), 054428.

[23] M. Kenzelmann, A. B. Harris, S. Jonas, C. Broholm, J. Schefer, S. B. Kim, C. L. Zhang, S.-W. Cheong, O. P. Vaijk, and J. W. Lynn. Phys. Rev. Lett. **95** (2005), 087206.

[24] E. F. Bertaut. Acta Cryst. A **24** (1968), 217.

[25] P. G. Radaelli and L. C. Chapon. Symmetry constraints on the electrical polarization in novel multiferroic materials. `cond-mat/0609087`.

[26] L. D. Landau and E. M. Lifshitz. *Statistical Physics*, vol. 5 of *Course of Theoretical Physics*. 3rd edn. (Butterworth-Heinemann, 1980).

[27] A. B. Harris, A. Aharony, and O. Entin-Wohlman. Phys. Rev. Lett. **100** (2008), 217202.

[28] A. B. Harris, M. Kenzelmann, A. Aharony, and O. Entin-Wohlman. Phys. Rev. B **78** (2008), 014407.

[29] E. F. Bertaut, G. Buisson, S. Quezel-Ambrunaz, and G. Quezel. Solid State Commun. **5** (1967), 25.

[30] A. Muñoz, J. A. Alonso, M. T. Casais, M. J. Martínez-Lope, J. L. Martínez, and M. T. Fernández-Díaz. Phys. Rev. B **65** (2002), 144423.

[31] G. Smolenskii and I. Chupis. Sov. Phys. Usp. **25** (1982), 475.

[32] H. Katsura, A. V. Balatsky, and N. Nagaosa. Phys. Rev. Lett. **98** (2007). 027203.

[33] T. Nagamiya. *Solid State Physics*, vol. 20, chap. Theory of Helical Spin Configurations, p. 305 (Academic Press, 1967).

[34] T. Holstein and H. Primakoff. Phys. Rev. **58** (1940), 1098.

[35] R. Resta. Ferroelectrics **136** (1992), 51.

[36] R. D. King-Smith and D. Vanderbilt. Phys. Rev. B **47** (1993), 1651.

[37] R. Resta. Rev. Mod. Phys. **66** (1994), 899.

[38] K. Rabe, C. H. Ahn, and J.-M. Triscone (eds.). *Physics of Ferroelectrics. A Modern Perspective*. No. 105 in Topics in Applied Physics (Springer, 2007).

[39] W. Cochran. Phys. Rev. Lett. **3** (1959), 412.

[40] W. Cochran. Adv. Phys. **9** (1960), 387.

[41] M. Dressel and G. Grüner. *Electrodynamics of Solids. Optical Properties of Electrons in Matter* (Cambridge University Press, 2002).

[42] H. A. Kramers. Nature **117** (1925), 775.

[43] R. de L. Kronig. J. Opt. Soc. Am. **12** (1926), 547.

[44] ABB-Bomem, Québec, Canada. *DA3 Spectrometer System Manual* (1991).

[45] J. R. Simpson. Ph.D. thesis, University of Maryland (2004). Available at the following URL http://www.lib.umd.edu/drum/handle/1903/2079.

[46] G. S. Jenkins. Ph.D. thesis, University of Maryland (2003). Available at the following URL http://www.lib.umd.edu/drum/handle/1903/24.

[47] G. B. Arfken and H. J. Weber. *Mathematical Methods for Physicists*. 5th edn. (Academic Press, 2000).

[48] L. C. Chapon, G. R. Blake, M. J. Gutmann, S. Park, N. Hur, P. G. Radaelli, and S.-W. Cheong. Phys. Rev. Lett. **93** (2004), 177402.

[49] L. C. Chapon, P. G. Radaelli, G. R. Blake, S. Park, and S.-W. Cheong. Phys. Rev. Lett. **96** (2006), 097601.

[50] Y. Noda, H. Kimura, Y. Kamada, T. Osawa, Y. Kukuda, Y. Ishikawa, S. Kobayashi, Y. Wakabayashi, H. Sawa, N. Ikeda, and K. Kohn. Physica B **385-386** (2006), 119.

[51] C. Vecchini, L. C. Chapon, P. J. Brown, T. Chatterji, S. Park, S.-W. Cheong, and P. G. Radaelli. Phys. Rev. B **77** (2008), 134434.

[52] J.-H. Kim, S.-H. Lee, S. I. Park, M. Kenzelmann, J. Schefer, J.-H. Chung, C. F. Majkrzak, S. Wakimoto, S. Y. Park, S.-W. Cheong, M. Matsuda, H. Kimura, Y. Noda, and K. Kakurai (2008). `cond-mat/0803.1123`.

[53] V. Polyakov, V. Plakhty, M. Bonnet, P. Burlet, L.-P. Regnault, S. Gavrilov, I. Zobkalo, and O. Smirnov. Physica B **297** (2001), 208.

[54] I. Kagomiya, S. Matsumoto, K. Kohn, Y. Fukuda, T. Shoubu, H. Kimura, Y. Noda, and N. Ikeda. Ferroelectrics **286** (2002), 167.

[55] G. R. Blake, L. C. Chapon, P. G. Radaelli, S. Park, N. Hur, S.-W. Cheong, and J. Rodríguez-Carvajal. Phys. Rev. B **71** (2005), 214402.

[56] B. Mihailova, M. M. Gospodinov, B. Guttler, F. Yen, A. P. Litvinchuk, and M. N. Iliev. Phys. Rev. B **71** (2005), 172301.

[57] A. F. García-Flores, E. Granado, H. Martinho, R. R. Urbano, C. Rettori, E. I. Golovenchits, V. A. Sanina, S. B. Oseroff, S. Park, and S.-W. Cheong. Phys. Rev. B **73** (2006), 104411.

[58] J. Alonso, M. Casais, M. Martínez-Lope, J. Martínez, and M. Fernández-Díaz. J. Phys. Condens. Matter **9** (1997), 8515.

[59] D. Higashiyama, S. Miyasaka, N. Kida, T. Arima, and Y. Tokura. Phys. Rev. B **70** (2004), 174405.

[60] J. R. Simpson *et al.* (2008). To be published.

[61] E. I. Golovenchits, V. A. Sanin, and A. V. Babinskiĭ. JETP **85** (1997), 156.

[62] M. J. P. Gingras, B. C. den Hertog, M. Faucher, J. S. Gardner, S. R. Dunsiger, L. J. Chang, B. D. Gaulin, N. P. Raju, and J. E. Greedan. Phys. Rev. B **62** (2000), 6496.

[63] S. Jandl. private communication (2006).

[64] J. Lorenzana and G. A. Sawatsky. Phys. Rev. Lett. **74** (1995), 1867.

[65] A. Damascelli, D. van der Marel, M. Grüninger, C. Presura, and T. T. M. Palstra. Phys. Rev. Lett. **81** (1998), 918.

[66] A. Pimenov, A. A. Mukhin, V. Y. Ivanov, V. D. Travkin, A. M. Balbashov, and A. Loidl. Nature Physics **2** (2006), 97.

[67] R. Valdés Aguilar, A. B. Sushkov, S. Park, S.-W. Cheong, and H. D. Drew. Phys. Rev. B **74** (2006), 184404.

[68] A. B. Souchkov, J. R. Simspson, M. Quijada, H. Ishibashi, N. Hur, J. S. Ahn, S. W. Cheong, A. J. Millis, and H. D. Drew. Phys. Rev. Lett. **91** (2003), 027203.

[69] A. Pimenov, T. Rudolf, F. Mayr, A. Loidl, A. A. Mukhin, and A. M. Balbashov. Phys. Rev. B **74** (2006), 100403R.

[70] E. Golovenchits and V. Sanina. J. Phys. Condens. Matter **16** (2004), 4325.

[71] N. Hur, S. Park, P. Sharma, S. Guha, and S. Cheong. Phys. Rev. Lett. **93** (2004), 107207.

[72] S.-H. Lee. Private communication, 2006.

[73] Y. Noda, H. Kimura, Y. Kamada, T. Osawa, Y. Fukuda, Y. Ishikawa, S. Kobayashi, Y. Wakabayashi, H. Sawa, N. Ikeda, and K. Kohn. Physica B **385-386** (2006), 119.

[74] C. Vecchini, L. C. Chapon, P. J. Brown, T. Chatterji, S. Park, S.-W. Cheong, and P. G. Radaelli. Phys. Rev. B **77** (2008), 134434.

[75] W. Baltensperger and J. S. Helman. Helv. Phys. Acta **41** (1968), 668.

[76] A. B. Sushkov, O. Tchernyshyov, W. Ratcliff II, S.-W. Cheong, and H. D. Drew. Phys. Rev. Lett. **94** (2005), 137202.

[77] K. Wakamura and T.Arai. J. Appl. Phys. **63** (1988), 5824.

[78] S.-H. Lee, C. Broholm, T. H. Kim, W. Ratcliff II, and S.-W. Cheong. Phys. Rev. Lett. **84** (2000), 3718.

[79] H. Jahn and E. Teller. Proc. R. Soc. A **161** (1937), 220.

[80] A. M. Glazer. Act. Cryst. B **28** (1972), 3384.

[81] T. Kimura, G. Lawes, T. Goto, Y. Tokura, and A. Ramirez. Phys. Rev. B **71** (2005), 224425.

[82] A. B. Sushkov, R. Valdés Aguilar, S. Park, S.-W. Cheong, and H. D. Drew. Phys. Rev. Lett. **98** (2007), 027202.

[83] D. Senff, P. Link, K. Hradil, A. Hiess, L. P. Regnault, Y. Sidis, N. Aliouane, D. N. Argyriou, and M. Braden. Phys. Rev. Lett. **98** (2007), 137206.

[84] S. H. Lee, J. H. Kim, J. H. Chung, Y. Qiu, M. Kenzelman, T. J. Sato, S. Park, and S.-W. Cheong. Http://meetings.aps.org/link/BAPS.2007.MAR.J13.12.

[85] Y. J. Choi, C. L. Zhang, S. Park, and S.-W. Cheong. Unpublished.

[86] D. N. Argyriou, N. Aliouane, J. Strempfer, I. Zegkinoglou, B. Bohnenbuck, K. Habicht, and M. v. Zimmermann. Phys. Rev. B **75** (2007), 020101.

[87] R. Valdés Aguilar, A. B. Sushkov, C. L. Zhang, Y. J. Choi, S.-W. Cheong, and H. D. Drew. Phys. Rev. B **76** (2007), 060404.

[88] D. Senff, P. Link, N. Aliouane, D. N. Argyriou, and M. Braden. Phys. Rev. B **77** (2008), 174419.

[89] S. Picozzi, K. Yamauchi, B. S. and. I. A. Sergienko, and E. Dagotto. Phys. Rev. Lett. **99** (2007), 227201.

[90] D. Senff, N. Aliouane, D. N. Argyriou, A. Hiess, L. P. Regnault, P. Link, K. Hradil, Y. Sidis, and M. Braden. J. Phys.: Condens. Matter **20** (2008), 434212.

[91] D. L. Rousseau, R. P. Bauman, and S. P. S. Porto. J. Raman Spectroscopy **10** (1981), 253.

[92] Bilbao Crystallographic Server. http://www.cryst.ehu.es/.